UNIVERSITY OF CALIFORNIA
RIVERSIDE

Erythrocyte-Derived Optical Constructs for Targeted Fluorescence Imaging and Combined Chemo-phototheranostics

A Dissertation submitted in partial satisfaction
of the requirements for the degree of

Doctor of Philosophy

in

Biochemistry and Molecular Biology

by

Jenny Thuy Mac

December 2019

Dissertation Committee:
Dr. Bahman Anvari, Chairperson
Dr. Russ Hille
Dr. Valentine Vullev

The Dissertation of Jenny Thuy Mac is approved:

_____

_____

_____

Committee Chairperson

University of California, Riverside

ACKNOWLEDGEMENTS

I would like to thank my advisor Dr. Bahman Anvari for all his support and mentoring throughout my doctorate studies at UC Riverside. Without his guidance, I would not have ended up as the person I am today. Thank you for taking a chance on project ideas that I pitched to expand my work. I would also like to thank my committee members Dr. Russ Hille and Dr. Valentine Vullev for their guidance throughout the years.

I would like to acknowledge my lab mates, Raviraj Vankayala, Joshua Burns, Sabrina Wueste, Dipti Patel for their support as these publications would not be possible without their help.

Lastly, I would like to thank my friends and family for their unconditional support during the time when I sacrificed my personal life for academia.

The text of this dissertation, in part, is a reprint of the material as it appears in Biomedical Optics Express (Chapter 1, April 1, 2016), ACS Biomaterials Science and Engineering (Chapter 2, June 28, 2018), and Biomaterials Science (Chapter 3, April 29, 2019).

ABSTRACT OF THE DISSERTATION

Erythrocyte-Derived Optical Constructs for Targeted Fluorescence Imaging and Combined Chemo-phototheranostics

by

Jenny Thuy Mac

Doctor of Philosophy, Graduate Program in Biochemistry and Molecular Biology
University of California, Riverside, December 2019
Dr. Bahman Anvari, Chairperson

Erythrocyte-derived delivery platforms have potential for personalized theranostics. Key advantages of using this platform include: improved biocompatibility based on fabrication of the constructs from autologously-derived blood, extended in vivo circulation time, tunable size (ranging from nano- to micron-size scale) to provide capability for various clinical applications ranging from tumor to vascular imaging, encapsulation of various payloads (fluorescent probe and/or chemotherapeutic drug), and surface modification for targeted specific biomarkers. In particular, erythrocyte-derived nanoparticles can be doped with near infrared (NIR) chromophores, such as FDA-approved indocyanine green (ICG) and functionalized with antibodies to provide dual capabilities for targeted near-infrared imaging and phototherapy. We demonstrate the synthesis and characterization of these structures, as well as, their capability for in vitro targeting of cancer cells. Furthermore, we studied the effects of particle size on

biodistribution and toxicological evaluation of erythrocyte-derived constructs in healthy mice. In addition, these erythrocyte-derived platforms can be customized for light-triggered combined chemotherapy and phototherapy by co-loading doxorubicin (DOX) and ICG.

Table of Contents

Table of Figures

Introduction

My doctoral research involves the fabrication of biological nanoparticles for biomedical application. In particular, our group has engineered erythrocyte-derived nano-constructs which can be doped with near infrared (NIR) chromophores such as indocyanine green (ICG), currently the only FDA-approved NIR chromophore [1-3]. We refer to these constructs as NIR Erythrocyte-derived Transducers (NETs), since once they are photo-activated by NIR excitation, they can transduce light to emit fluorescence or generate heat. Use of NIR excitation wavelengths (≈700-1450 nm) is particularly advantageous since there is minimal light absorption and scattering by endogenous biomolecules, resulting in increased optical penetration depth on the order of ≈2-3 cm [4]. As a NIR chromophore, ICG has been utilized in an array of medical diagnostics, ranging from ophthalmic angiography to biopsy of sentinel lymph nodes [5-9]. Unfortunately, ICG is non-specific, and short-lived in plasma (half-life on the order of ≈ 2-3 minutes) due to rapid clearance by hepatocytes. Therefore, it is important to develop techniques to sustain ICG circulation. One approach is to encapsulate ICG into erythrocyte-derived nanoparticles. Normal erythrocytes have long circulation times of ~90-120 days [10]. Therefore, encapsulation of chromophores such as ICG into nano-constructs that preserves the molecules (e.g., CD47) responsible for camouflaging of the carrier, can potentially lead to increase circulation time [10]. Other key advantages of NETs are that they are potentially non-immunogenic, and non-toxic since they can be derived autologously or from the biocompatible blood types. Finally, the surface of NETs can be functionalized with

entities (e.g., antibodies) with molecular recognition capabilities to achieve site-targeted delivery.

Most of my dissertation research focuses on the surface modification of NETs for active targeting of cancer cells for fluorescence imaging as well as combinatorial chemo-phototherapeutics. In addition to this work, I contributed to studies elucidating the biodistribution and cytotoxicity of NETs in healthy mice which will not be highlighted in this proposal.

References

1. Bahmani, B.; Bacon, D.; Anvari, B., Erythrocyte-derived photo-theranostic agents: hybrid nano-vesicles containing indocyanine green for near infrared imaging and therapeutic applications. *Sci Rep-Uk* **2013,** *3*. DOI: ARTN 2180

10.1038/srep02180.

2. Burns, J. M.; Saager, R.; Majaron, B.; Jia, W. C.; Anvari, B., Optical properties of biomimetic probes engineered from erythrocytes. *Nanotechnology* **2017,** *28* (3). DOI: Artn 035101

10.1088/1361-6528/28/3/035101.

3. Mac, J. T.; Nunez, V.; Burns, J. M.; Guerrero, Y. A.; Vullev, V. I.; Anvari, B., Erythrocyte-derived nano-probes functionalized with antibodies for targeted near infrared fluorescence imaging of cancer cells. *Biomed Opt Express* **2016,** *7* (4), 1311-1322. DOI: 10.1364/Boe.7.001311.

4. Frangioni, J. V., In vivo near-infrared fluorescence imaging. *Curr Opin Chem Biol* **2003,** *7* (5), 626-634. DOI: 10.1016/j.cbpa.2003.08.007.

5. Hirche, C.; Murawa, D.; Mohr, Z.; Kneif, S.; Hunerbein, M., ICG fluorescence-guided sentinel node biopsy for axillary nodal staging in breast cancer. *Breast Cancer Res Treat* **2010,** *121* (2), 373-8. DOI: 10.1007/s10549-010-0760-z.

6. Sevick-Muraca, E. M.; Sharma, R.; Rasmussen, J. C.; Marshall, M. V.; Wendt, J. A.; Pham, H. Q.; Bonefas, E.; Houston, J. P.; Sampath, L.; Adams, K. E.; Blanchard, D. K.; Fisher, R. E.; Chiang, S. B.; Elledge, R.; Mawad, M. E., Imaging of lymph flow in breast cancer patients after microdose administration of a near-infrared fluorophore: feasibility study. *Radiology* **2008,** *246* (3), 734-41. DOI: 10.1148/radiol.2463070962.

7. Crane, L. M.; Themelis, G.; Arts, H. J.; Buddingh, K. T.; Brouwers, A. H.; Ntziachristos, V.; van Dam, G. M.; van der Zee, A. G., Intraoperative near-infrared fluorescence imaging for sentinel lymph node detection in vulvar cancer: first clinical results. *Gynecol Oncol* **2011,** *120* (2), 291-5. DOI: 10.1016/j.ygyno.2010.10.009.

8. van der Vorst, J. R.; Schaafsma, B. E.; Verbeek, F. P.; Swijnenburg, R. J.; Hutteman, M.; Liefers, G. J.; van de Velde, C. J.; Frangioni, J. V.; Vahrmeijer, A. L., Dose optimization for near-infrared fluorescence sentinel lymph node mapping in patients with melanoma. *Br J Dermatol* **2013,** *168* (1), 93-8. DOI: 10.1111/bjd.12059.

9. Jeschke, S.; Lusuardi, L.; Myatt, A.; Hruby, S.; Pirich, C.; Janetschek, G., Visualisation of the lymph node pathway in real time by laparoscopic radioisotope- and fluorescence-guided sentinel lymph node dissection in prostate cancer staging. *Urology* **2012,** *80* (5), 1080-6. DOI: 10.1016/j.urology.2012.05.050.

10. Hu, C.-M. J.; Fang, R. H.; Zhang, L., Erythrocyte-Inspired Delivery Systems. *Advanced Healthcare Materials* **2012,** *1* (5), 537-547. DOI: doi:10.1002/adhm.201200138.

Chapter 1. Erythrocyte-derived nano-probes functionalized with antibodies for targeted near infrared fluorescence imaging of cancer cells

1.1 Abstract

Constructs derived from mammalian cells are emerging as a new generation of nano-scale platforms for clinical imaging applications. Herein, we report successful engineering of hybrid nano-structures composed of erythrocyte-derived membranes doped with FDA-approved near infrared (NIR) chromophore, indocyanine green (ICG), and surface-functionalized with antibodies to achieve molecular targeting. We demonstrate that these constructs can be used for targeted imaging of cancer cells in vitro. These erythrocyte-derived optical nano-probes may provide a potential platform for clinical translation, and enable molecular imaging of cancer biomarkers.

1.2 Introduction

Fluorescence imaging using near infrared (NIR) wavelengths, particularly in the range between 700-1450 nm, continues to be an important imaging modality in clinical and biomedical applications. There are two key advantages to the use of NIR wavelengths. First, the NIR "transparency window" facilitates relatively deep penetration of light, on the order of 2-3 cm, due to the reduced absorption of photons by water and proteins, as well as the diminished scattering within the NIR spectral band [1-3]. Second, given that

there is minimal auto-fluorescence in NIR spectral bands, the use of an exogenous fluorescent probe enhances the image contrast.

Intraoperative NIR fluorescence imaging has gained entry into early clinical studies [1]. By combining NIR fluorescent probes with molecular targeting agents, the specificity of such probes can be enhanced. One particular NIR exogenous chromophore is indocyanine green (ICG). To-date, ICG remains the only FDA-approved NIR dye for specific imaging applications, and one of the least toxic agents administered to humans [1]. In addition to its current clinical imaging usage for specific indications such as choroidal circulation [4], ICG has been investigated for sentinel lymph node mapping in patients with various types of cancer [5-9], and imaging of intracranial aneurysm and cerebral arteriovenous malformations [10-11].

Despite its use in such medical applications, the major drawbacks of ICG include its non-specificity, and short half-life within plasma (≈ 2-4 min). Encapsulation into nano-sized structures has been investigated as an approach to shield ICG from non-specific interactions with plasma proteins, and extend its circulation time. To-date, ICG has been encapsulated into various nano-sized constructs including those composed of micelles, liposomes, synthetic polymers [12-15], calcium phosphate [16], and silica and silicate matrices [17-18]. We have previously reported on encapsulation of ICG into polymeric nanoparticles, coated with poly ethylene glycol (PEG), as a technique to increase the blood circulation time of ICG and delay this hepatic accumulation up to an hour [19].

Mammalian cells such as erythrocytes, lymphocytes, and macrophages are receiving increased attention as new types of platforms for the delivery of therapeutic or imaging

agents [20-25]. A particular feature of normal erythrocytes that distinguishes them from other cell types is their naturally long circulation time (≈ 90-120 days), attributed to the presence of "self-marker" proteins on their surface to inhibit immune response [23, 25]. One putative self-marker is CD47 glycoprotein [26-27], which impedes phagocytosis through signaling with the phagocyte receptor, SIRPα (CD172a) [28-29] Therefore, a key potential advantage of erythrocytes as a delivery platform is that by making their cargo (e.g. ICG) available over a long time, imaging may be performed over an extended time.

Our group recently reported the first successful engineering of nano-sized structures derived from erythrocytes doped with ICG, and their utility as light-activated theranostic agents for fluorescence imaging and photothermal destruction of human cells [30]. We refer to these constructs as NIR erythrocyte-derived transducers (NETs). Expanding on our previous work, in this paper we report for the first time the successful functionalization of the NETs surface with antibodies as molecular recognition biomolecules, and demonstrate the utility of antibody-functionalized NET as nano-probes for specific NIR fluorescence imaging of cancer cells *in vitro*.

1.3 Materials and Methods

1.3.1 NETs fabrication and functionalization with monoclonal antibodies

Erythrocytes were separated from bovine whole blood (Rockland Immunochemicals, Inc., Limerick, PA) by centrifugation (1000×*g*, 5 min, 4°C). Plasma and the buffy coat were discarded, and the resulting packed erythrocytes were washed three times in 1x (≈ 320 mOsm) phosphate buffer saline (PBS). Packed erythrocytes were then subject to

hypotonic treatment (1 ml of 0.25x PBS (≈ 80 mOsm), pH=8, 5 min, 4°C), after which they were centrifuged (20,000×*g*, 15 min, 4°C). The supernatant was discarded. Hypotonic treatment of erythrocytes in 0.25x PBS, and centrifugation was repeated until hemoglobin was removed, resulting in an opaque white pellet. The pellet was resuspended in 1 ml of 1x PBS. Upon completion of this step, hemoglobin-depleted micron-sized erythrocyte ghosts (EGs) were obtained.

To demonstrate proof-of-principle, we chose antibodies against the human epidermal growth receptor (HER2) as the test antibody to functionalize the NETs. HER2 is a clinically important receptor biomarker involved in carcinogenesis of various solid tumors, particularly breast, colorectal, non-small cell lung cancer, and ovarian cancer [31-32]. Nevertheless, our approach can be readily used to functionalize the NETs with other antibodies.

The functionalization process was as follows, and shown in Figure 1.1. First, we activated the aldehyde functional groups on anti-HER2 (30 μg) (Santa Cruz Biotechnology, Inc., Dallas, TX) using oxidation with sodium periodate (10 μl of 100 mM) (Sigma Aldrich, St. Louis, MO). Excess oxidizing agent was removed by filtering the activated anti-HER2 through 50k Amicon Ultra-4 centrifuge filter units (Millipore, Temecula, CA). Next, to covalently attach the activated anti-HER2 to the NETs surface, we used a linker molecule, 1,2-distearoyl-sn-glycero-3-phosphoethanolamine-polyethylene glycol-amine (DSPE-PEG-NH_2) (2000 Da) (Nanocs, Inc, New York, NY), connected to the surface of EGs through lipid insertion in water followed by filtration and exchange of buffer to 1x PBS through 50k Amicon Ultra-4 centrifuge filter units

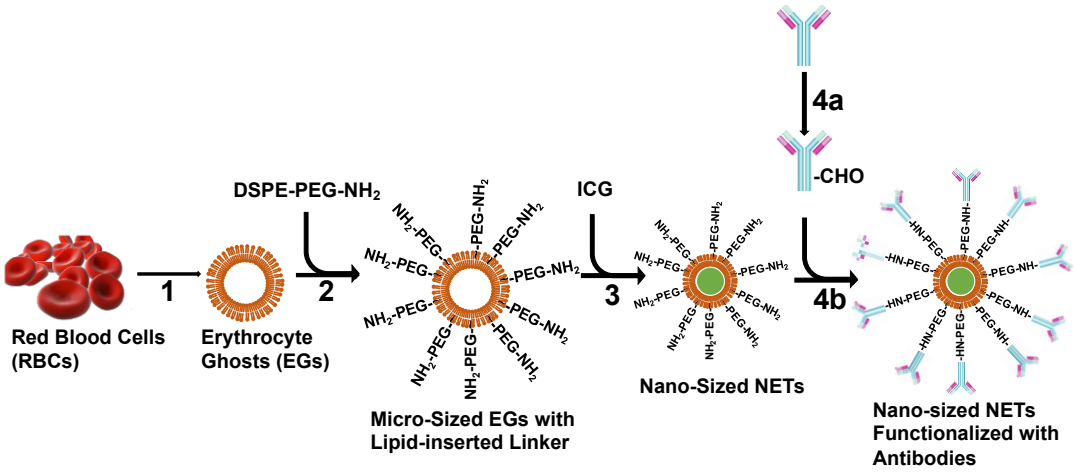

Figure 1.1: Schematic of the methodology to fabricate NETs functionalized with antibodies. The various steps are defined as follows: (1) hemoglobin depletion; (2) lipid insertion of linker molecule DSPE-PEG-NH2; (3) sequential extrusion through 400 nm and 100 nm porous membranes, and ICG loading; (4a) antibody oxidation to activate the aldehyde groups; and (4b) antibody conjugation by reductive amination..

(Millipore, Temecula, CA). A similar lipid insertion method of a linker molecule has been reported for functionalization of erythrocyte membrane-cloaked polymeric nanoparticles [33].

We then extruded the EGs bearing lipid-inserted DSPE-PEG-NH_2, and suspended in 1 ml of PBS containing 100 µM of ICG, 20 times through 400 nm polycarbonate porous membranes followed by 20 additional extrusions through 100 nm diameter membranes using an Avanti mini extruder (Avanti Polar Lipids, Inc., Alabaster, Al). This step results in loading of ICG into the EGs to form NETs. NETs bearing lipid-inserted DSPE-PEG-NH_2 were mixed with activated anti-HER2 for five minutes, and then incubated with 5 µl of 20 mM sodium dithionite, as the reducing agent, for 30 minutes at 4 °C to finally produce NETs functionalized with anti-HER2. Excess reducing agent was removed, and anti-HER2 functionalized NETs were isolated through ultra-centrifugation (≈53,000×*g*, 1 hour, 4ºC). The supernatant was discarded. The pellet was washed three

times, and resuspended in 1 ml of 1x PBS, and stored in the dark at 4 ºC. The procedure for fabrication of non-functionalized NETs was similar as above except that EGs without any additional surface modification were suspended in 1 ml of 1x PBS containing 100 μM of ICG, and extruded.

1.3.3 Characterization of NETs

The hydrodynamic diameters of non-functionalized and anti-HER2 functionalized NETs were measured by dynamic light scattering (DLS) (Zetasizer Nanoseries, NanoZS90, Malvern Instruments, Malvern, UK). The absorption spectra of non-functionalized and anti-HER2 functionalized NETs were obtained using a UV Visible spectrophotometer (Cary 50 UV-Vis spectrophotometer, Agilent Technologies, Santa Clara, CA) with optical path length of 1 cm. The fluorescence spectra of non-functionalized and anti-HER2 functionalized NETs were acquired in response to photo-excitation at 650 nm excitation with a 450W xenon lamp, and recorded using a fluorometer (Fluorolog-3 spectrofluorometer, Edison, NJ).

To prepare samples for scanning electron microscopy (SEM) imaging, samples were fixed with 2.5% glutaraldehyde, overnight. Then, 10 μl of sample was added to poly-L-lysine coated slide for 5 minutes, dried (Critical-point-dryer Balzers CPD0202), sputter coated with platinum, and imaged with SEM FEI NNS450. To confirm successful antibody-functionalization, non-functionalized NETs (control) and anti-HER2 functionalized NETs were incubated with FITC-labeled secondary rabbit antibody (30 μg) (Life Technologies, Carlsbad, CA) for 1 hour. Excess secondary antibody was filtered through 100k Amicon Ultra-4 centrifuge filter (Millipore, Temecula, CA). The

FITC fluorescence spectra were acquired in response to photo-excitation at 488 nm with a 450W xenon lamp, and recorded using a fluorometer (Fluorolog-3 spectrofluorometer, Edison, NJ).

1.3.4 Aggregation assessment

To assess possible aggregation of the NETs, particularly after functionalization, both non-functionalized and functionalized NETs were pelleted and re-suspended in 1 ml of either 1x PBS, Rosewell Park Memorial Institute (RPMI) 1640 cell culture medium (Mediatech, Inc, Manassas, VA), or RPMI 1640 supplemented with 10% fetal bovine serum (FBS) (Thermo Fisher Scientific, Waltham, MA). The hydrodynamic diameter distributions were obtained by DLS within 1-2 hours of incubation of the particles with each of the three dispersion agents.

1.3.5 Assessment of NETs absorption stability

We used miron-sized (non-extruded) EGs to fabricate non-functionalized NETs. EGs were incubated with hypotonic buffer (Na_2HPO_4/ $Na_2H_2PO_4$, 140 mOsm, pH 5.8), and ICG dissolved in water so that the ICG concentration in this loading solvent was 50 μM. Suspensions were then incubated for five minutes at 4 °C in dark, centrifuged at 20,000×g for 15 minutes, and washed twice with 1x PBS to remove any non-encapsulated ICG. The resulting micron-sized NETs were re-suspended in cold 1x PBS buffer solution. We obtained the absorption spectra of the NETs suspended in 1 ml of 1x PBS immediately after fabrication (Day 0), and at every other day post-fabrication for up to 8 days.

1.3.6 Assessment of CD47 presence on NETs

To access for the presence of CD47 on the surface of NETs, we incubated non-extruded (micron-sized) EGs (positive control), and non-functionalized nano-sized NETs fabricated after extrusion of the EGs (as described in section 2.1) with FITC-labeled anti-CD47 (4 μg) (Santa Cruz Biotechnology, Inc, Dallas, TX) for one hour at 4 ºC. As the negative control sample, we used Texas Red-labeled liposomes (which lack CD47), and incubated them with FITC-labeled anti-CD47 in a similar manner as those used for incubation of EGs and NETs. Excess and unbound antibody were removed by centrifugation (≈53,000×g, 1 hour, 4ºC). Fluorescence emission spectra of all samples were acquired in response to photo-excitation at 488 nm with a 450W xenon lamp, and recorded using the fluorometer.

1.3.7 Targeted fluorescence imaging of cancer cells

To validate the effectiveness of anti-HER2 functionalized NETs in targeting the HER2 receptors, we used two types of human epithelial ovarian cancer cells, SKOV3 and OVCAR3, which have relatively high and low HER2 expression levels, respectively [34-35]. We added 100 μl of SKOV3 or OVCAR3 cell suspension (≈10^6 cells/ml) in RPMI 1640 medium supplemented with 1% Penicillin/Streptomycin, and 10% FBS (ATCC, Manassas, VA) to each well of a 96-well flat bottom micro-titer plate. Cell suspensions were plated in 5% CO_2 overnight. On the following day, the old culture medium was replaced with fresh medium. We incubated the cells at 37 °C with 100 μl of 1x PBS (negative control), ≈ 9 μM free ICG (negative control), non-functionalized (positive

control), or anti-HER2 functionalized NET, in separate wells for two hours in the dark. Cells were subsequently washed twice with 1x PBS, and finally incubated with 4',6-diamidino-2-phenylindole (DAPI) for 15 minutes to stain the nuclei for fluorescence imaging.

NIR fluorescence emission (> 770 nm) in response to 740 ± 35 nm excitation by a Nikon halogen lamp was captured by an electron multiplier gained CCD camera (Quant EM-CCD, C9100-14 Hamamatsu, Shizuoka-ken, Japan). The camera exposure time was set at 0.7 s. Fluorescence emission from DAPI in the range of 435–485 nm was collected in response to 360 ± 20 nm excitation by a Nikon halogen lamp. We present falsely colored microscopic fluorescent images as the overlay of the NIR emission due to ICG (red channel), and visible emission due to DAPI-stained nuclei (blue channel).

1.3.8 Calculations

NETs per mL of blood:

https://bionumbers.hms.harvard.edu/bionumber.aspx?s=n&v=2&id=107602

Reference: Ballas SK. Erythrocyte concentration and volume are inversely related. Clin Chim Acta. 1987 Apr 30 164(2):243-4. p.243 top paragraph **PubMed ID** 3594914

$S_{RBC} = 140\ \mu M^2$

$N_{RBC} = 5.0 \times 10^6/\mu L$

Surface Area (S) = $4\pi r^2$

$r_{NET} = 0.05\ \mu M$ ($d_{NET} = 100$ nm)

$S_{NET} = 0.0314\ \mu M^2$

$N_{NET} = S_{RBC} * N_{RBC} / S_{NET} \approx$ **2.23×10^{13} NETs per mL of blood**

<u>Max number ICG molecules per NET:</u>

$$V = \frac{4}{3}\pi r^3$$

$r_{NET} =$ 50 nm (d_{NET} = 100 nm)

$d_{lipid\ membrane}$ = 6 – 8 nm

$r_{NET\ interior}$ = 42 nm

$V_{NET} = 3.10 \times 10^{-16}\ cm^3$

# of molecules = N * density * volume / MW

Density of water = 1 g/cm^3

Molecular Weight (MW) of ICG = 774 g/mol

N (Avogadro's number) 6.022×10^{23} molecules/mol

ICG molecules per NET ≈ **2.41×10^5 ICG/NET**

Effective number of ICG molecules

Example 1: ID-NETs

1xNETs = NETs fabricated from 1mL of whole blood

Loading concentration ≈ 775 μM ICG

Effective concentration ≈ 690 μM (10xNETs sample), estimated by calibration of ICG in water

1ml of 1xNETs = 53.4 μg of ICG

$N_{effective\ ICG} = M_{effective\ ICG} \times N/MW_{ICG} = 4.15 \times 10^{16}$ molecules of ICG /mL of blood

$N_{effective\ ICG/NET} = N_{effective\ ICG}/N_{NET} \approx$ **1863 molecules of ICG/NET**

Example 2: NETs (Chapter 3)

Loading concentration = 15 μM ICG (11.6μg/mL)

Loading efficiency ≈ 25%

$N_{effective\ ICG} = M_{effective\ ICG} \times N/MW_{ICG} = 2.26 \times 10^{16}$ molecules of ICG /mL of blood

$N_{effective\ ICG/NET} = N_{effective\ ICG}/N_{NET} \approx$ **101 molecules of ICG/NET**

1.4 Results and Discussion

1.4.1 Characterization of NETs

In Figure 1.2A, we present the diameter distributions for populations of non-functionalized and anti-HER2 functionalized NETs, as determined by the DLS technique. The estimated mean peak diameter of non-functionalized NETs was ≈ 162 nm with full width at half maximum (FWHM) diameter value of ≈ 85 nm. Upon functionalization with anti-HER2, the mean peak diameter increased to ≈ 252 nm, suggesting that the thickness

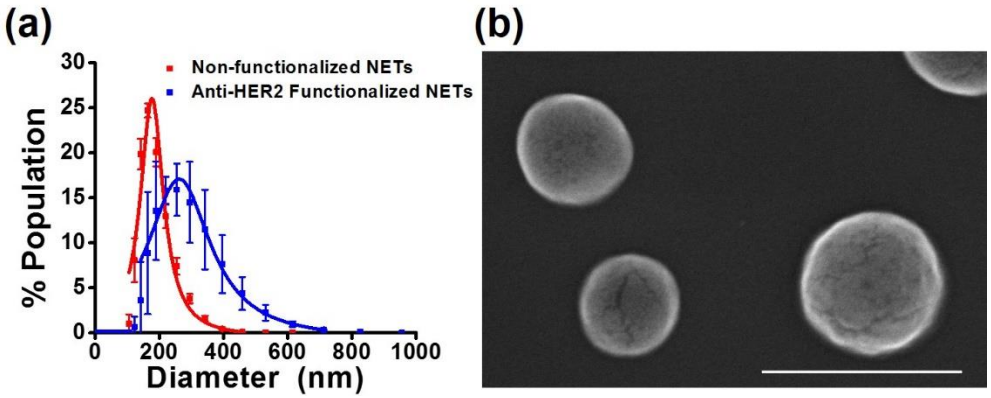

Figure 1.2: (A) Diameter distributions of non-functionalized, and anti-HER2 functionalized NETs as determined by dynamic light scattering. We present the mean of three measurements on each of the samples with error bars representing the standard deviations from the mean. We fitted Lorentzian functions to the measured diameter distributions (solid curves). (B) Illustrative SEM image of anti-HER2 functionalized NETs. Scale bar = 500 nm.

of the DSPE-PEG-NH_2 linker and the antibody grafted onto the NETs was ≈ 45 nm. The FWHM diameter value for population of anti-HER2-functionalized NETs increased to ≈ 225 nm, suggesting possible aggregation among the particles.

We present an SEM image of anti-HER2 functionalized NETs in Figure 1.2B. As demonstrated by this image, the morphology of the anti-HER2 functionalized NETs was

nearly spherical, and the diameter values were consistent with those as determined by the DLS technique.

We validated the functionalization of NETs using a secondary antibody labeled with FITC. As show in Figure 1.3A, the fluorescence emission spectrum of the NETs bearing the primary anti-HER2 and the secondary antibody showed a spectral peak at 520 nm, associated with FITC, in response to photo-excitation at 488 nm, confirming the successful grafting of anti-HER2 onto the NETs.

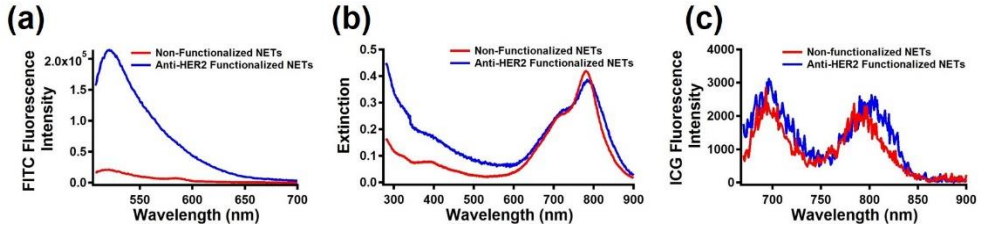

Figure 1.3: (A) Fluorescence emission spectra of non-functionalized NETs, and NETs functionalized with primary and FITC-labeled secondary antibodies. Photo-excitation wavelength was 488 nm, and fluorescence emissions > 508 nm were recorded. (B) Extinction spectra of non-functionalized, and anti-HER2 functionalized NETs. (C) Fluorescence emission spectra of non-functionalized an anti-HER2 functionalized NETs. Photo-excitation wavelength was 650 nm, and fluorescence emissions > 665 nm were recorded.

In Figure 1.3B, we present the extinction spectra, resulting from the combined effects of absorption and scattering, for non-functionalized and anti-HER2 functionalized NETs. The spectra in the 650-900 nm range were nearly identical, and attributed to the presence of ICG. Specifically, spectral peaks at ≈ 735 nm and 795 nm are associated with absorption by H-like aggregate and monomeric forms of ICG, respectively [36]. The value at 280 nm is predominantly associated with the absorption of membrane proteins on NETs, and increased from ≈ 0.16 for non-functionalized NETs to ≈ 0.45 for anti-HER2 functionalized NETs. We attribute this increase to the presence of the antibodies

successfully grafted onto the NETs. The overall increase in the extinction values associated with anti-HER2 functionalized NETs up to 600 nm is likely due to increased scattering by these particles, resulting from both an increase in diameter at the individual particle level after functionalization as well as possible aggregation among some of the particles. As demonstrated in Figure 1.3C, the fluorescence emission spectrum of anti-HER2 functionalized NETs resembled that of the non-functionalized NETs, indicating that functionalization did not alter the emission characteristics of the NETs. In response to photo-excitation at 650 nm, there were spectral peaks at ≈ 700 and 798 nm, which correspond to the H-like aggregate and monomeric forms of ICG, respectively.

1.4.2 Aggregation assessment

As evidenced by the results shown in Figure 1.4A, the mean peak diameter for these populations of non-functionalized NETs increased from ≈ 197 nm to ≈ 278 nm when changing the incubation medium from 1x PBS to RPMI 1640. The FWHM diameter value correspondingly increased from ≈ 98 nm to 187 nm. These increased values in peak and FWHM diameters are suggestive of the aggregation of non-functionalized NETs in RPMI cell culture medium. Similar aggregation effects have been reported for gold [37] and TiO_2 [38] nanoparticles when incubated in RPMI cell culture medium. The RPMI 1640 cell culture medium includes a variety of inorganic salts (e.g., sodium chloride, and sodium bicarbonate) in addition to various amino acids, vitamins, and glucose. The increased salt level reduces the electrostatic repulsion among the particles, leading to their aggregation [38]. When incubated in 10% FBS-supplemented RPMI cell culture medium, which is representative of physiological environment, the mean peak and FWHM diameter values

were reduced to ≈ 157 nm and 74 nm, respectively, suggesting a reduction in aggregate fractions within the population. Adsorption of FBS proteins (predominantly albumin) on the surface of NETs can possibly lead to steric stabilization to produce strong repulsions among the particles, leading to reduced agglomerate content [38-40].

In Figure 1.4B, we present the diameter distribution profiles for anti-HER2 functionalized NETs incubated in 1xPBS, RPMI 1640 cell culture medium, or RPMI 1640 supplemented with 10% FBS. The mean peak diameter for these populations of anti-HER2 functionalized NETs was lowered from ≈ 307 nm to ≈ 272 nm when changing the incubation medium from 1x PBS to RPMI 1640. The FWHM diameter value correspondingly decreased from ≈ 176 nm to 167 nm. These decreased values in peak and FWHM diameters suggest that the presence of increased salt content within the RPMI 1640 cell culture medium was not sufficient to reduce electrostatic repulsions among the anti-HER2 functionalized NETs and cause further aggregation. However,

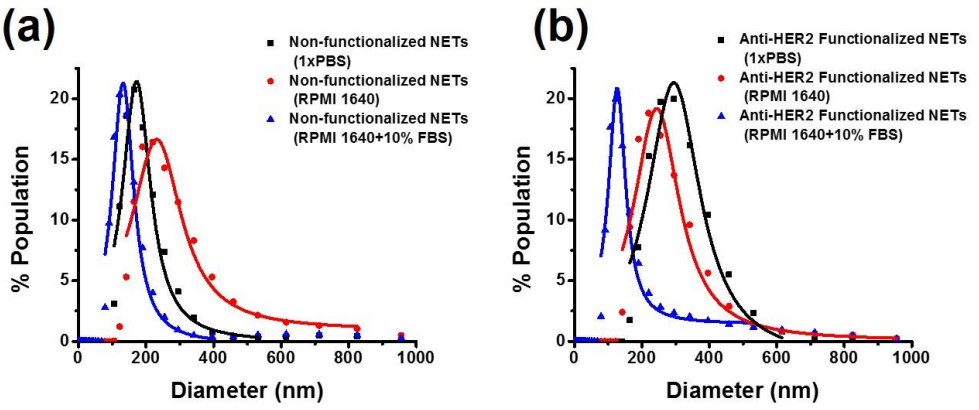

Figure 1.4: Hydrodynamic diameter distributions for (A) non-functionalized, and (B) anti-HER2 functionalized NETs incubated in 1xPBS, RPMI 1640 cell culture medium, and RPMI 1640+10% FBS. Each symbol on the plots represents the average diameter value of three populations of either non-functionalized or anti-HER2 functionalized NETs. Measurements were fitted by Lorentzian functions (solid traces).

when incubated in the physiologically-relevant medium of RPMI 1640 supplemented with 10% FBS, the peak and FWHM diameter values correspondingly decreased to ≈ 173 nm to 68 nm, indicating that there was considerable reduction in the aggregate fractions within the population of anti-HER2 functionalized NETs. Again, this reduced agglomerate content may result from adsorption of FBS serum proteins (mainly albumin) on the surface of anti-HER2 functionalized NETs.

1.4.3 Absorption stability of NETs

As shown in Figure 1.5, the absorption spectra of NETs remained nearly stable for at least 8 days post-fabrication. The absorbance value associated with the monomer form of ICG at 804 nm was reduced by only 5%, suggesting that this fraction of ICG may have leaked out over 8 days.

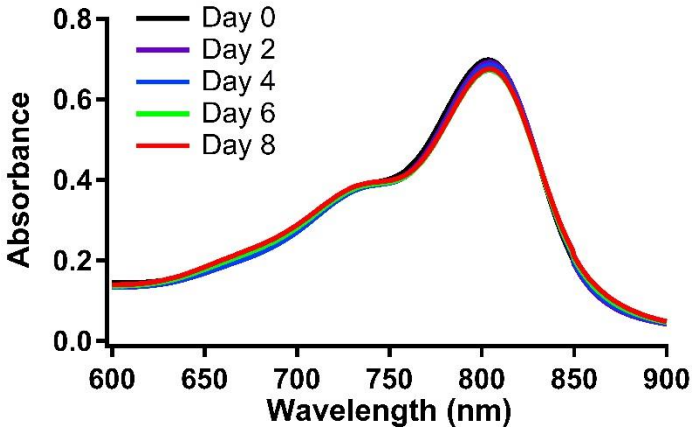

Figure 1.5: Time-dependent absorption spectra of non-functionalized NETs post-fabrication

1.4.4 Presence of CD47

In Figure 1.6, we present the fluorescence emission spectra of micron-sized EGs (non-extruded) (positive control), nano-sized NETs (extruded) conjugated with FITC-labeled

anti-CD47, and Texas Red-labeled liposomes (negative control). The presence of CD47 on both micron-sized (non-extruded) EGs and nano-sized NETs (formed after extruding the EGs) was confirmed by the fluorescence emission spectra, which showed spectral peaks associated with FITC at 520 nm. These results also suggest that the membranes on

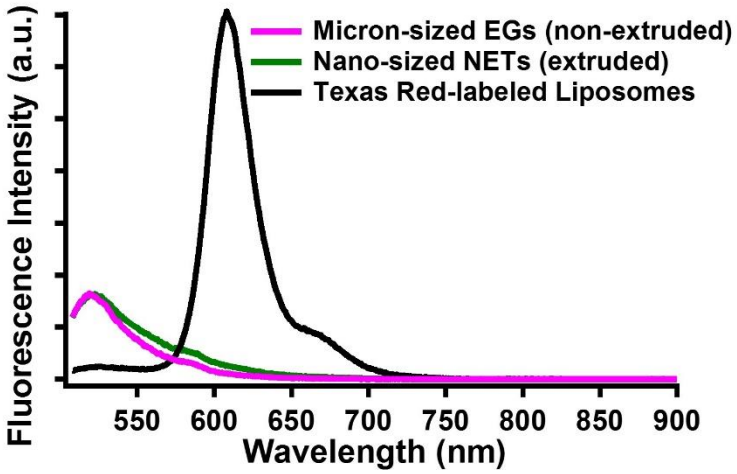

Figure 1.6: Fluorescence emission spectra of micron-sized EGs (non-extruded) (positive control), nano-sized NETs (extruded) conjugated with FITC-labeled anti-CD47, and Texas Red-labeled liposomes (negative control). Emission spectra from EGs and NETs show FITC-associated spectral peaks at 520 nm (488 nm photo-excitation wavelength), indicating the presence of CD47. Liposomes exhibited an emission peak associated with Texas Red at 609 nm (488 nm photo-excitation wavelength).

NETs remained as the right-side-out to accommodate anti-CD47 binding. The liposomes only showed an emission peak associated with Texas Red at 609 nm, indicating that they did not bind to anti-CD47.

1.4.5 Specific molecular targeting using functionalized NETs

We investigated the specific molecular targeting capability of functionalized NETs by fluorescence imaging of OVCAR3 and SKOV3 cancer cells, which have relatively low and high expression levels of the HER2 receptor. The overlay of the visible fluorescence emission due to DAPI (falsely colored in blue) and NIR emission due to ICG (falsely

colored in red), corresponding to OVCAR3 and SKOV3 cells, are shown in Figures 1.7A and 1.7B, respectively. There was minimal NIR emission from OVCAR3 cells following two hours of incubation with anti-HER2 functionalized NETs at physiological temperature (37 °C). However, NIR emission from SKOV3 was detected after two hours of incubation with anti-HER2 functionalized NETs, indicating the effectiveness of these nano-constructs in targeting HER2. We quantified the fluorescence emission from the cell images by integrating the emission over the spectral band > 770 nm. Results of such

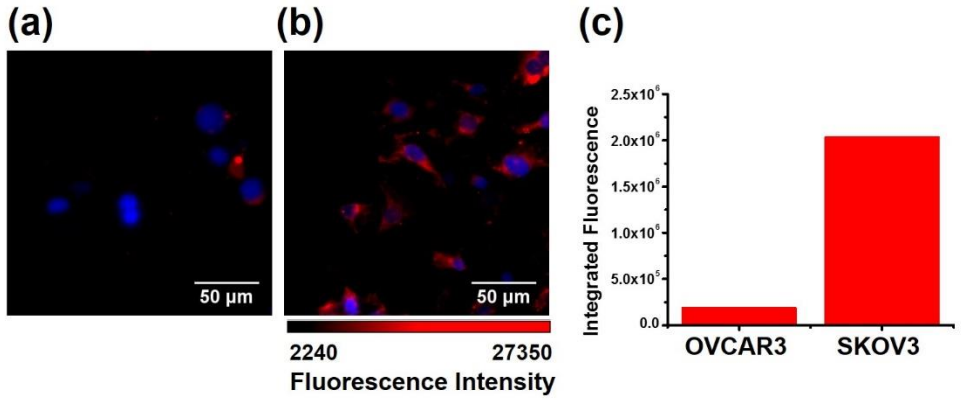

Figure 1.7: Fluorescent images of (A) OVCAR3 cells (low HER2 expression), and (B) SKOV3 cells (high HER2 expression) following two hours of incubation at 37 °C with anti-HER2 functionalized NETs. Images are falsely colored. Blue channel: DAPI. Red channel: NIR emission due to ICG. (c) NIR fluorescence emission of images (a-b) integrated over the >770 nm spectral band.

quantification are shown in Figure 1.7C. The integrated NIR emission from SKOV3 cells was nearly 11 times higher than that from OVCAR3 cells, indicating the effectiveness of anti-HER2 functionalized in targeted fluorescence imaging of SKOV3 cells that have high over-expression of HER2 receptors.

To further validate the specificity of anti-HER2 functionalized NETs in targeting the HER2 receptors, we incubated the SKOV3 cells with 1x PBS and free (non-encapsulated) ICG as negative controls, non-functionalized NETs (positive control), and

anti-HER2 functionalized NETs for two hours at 37 °C. Results of these experiments are presented in Figure 1.8. As shown in Figures 1.8A-1.8D, while there were none or minimal NIR emission from SKOV3 cells incubated with the control agents, NIR emission was detected from these cells following incubation with anti-HER2 functionalized NETs. NIR emission from these cell images was quantified as spectrally integrated emission values, and presented in Figure 1.8E, after subtracting the integrating emission from cells incubated in 1x PBS. The integrated NIR emission from SKOV3 cells incubated with anti-HER2 functionalized NETs was nearly 2.5 times higher than that of the SKOV3 cells incubated with non-functionalized NETs. The fluorescence emission from SKOV3 cells incubated with free ICG and non-functionalized NETs can be attributed to non-receptor mediated endocytosis. Anti-HER2 functionalized NETs undergo receptor-mediated endocytosis, and can be fluorescently imaged within the SKOV3 cells. These results confirm that specific targeting of HER2 receptors at physiological temperature can be achieved with anti-HER2 functionalized NETs, and

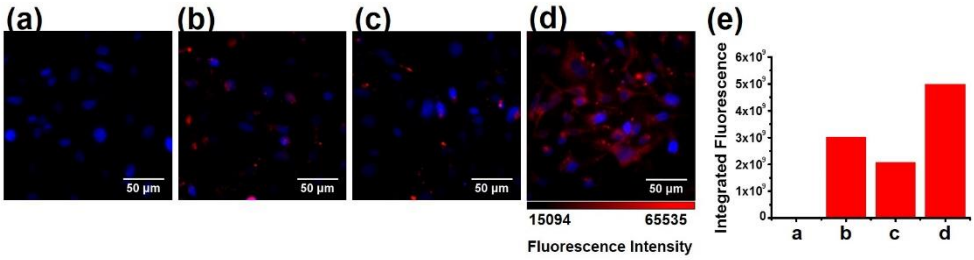

Figure 1.8: Fluorescent images of SKOV3 cells following two hours of incubation at 37 °C with (A) 1x PBS, (B) free ICG, (C) non-functionalized NETs, and (D) anti-HER2 functionalized NETs. Images are falsely colored. Blue channel: DAPI. Red channel: NIR emission due to ICG. (E) NIR fluorescence emission of images (A-E) integrated over the >770 nm spectral band.

demonstrate the potential of NETs equipped with molecular recognition biomolecules for targeted imaging of cancer cells.

To the best of our knowledge, this is the first report of successful engineering of nano-sized optical vesicles derived from erythrocyte-derived and functionalized at the surface with antibodies for targeted NIR imaging of cancer cells. NETs offer several potential advantages: As constructs that can be engineered autologously, or from compatible blood types, NETs may potentially serve as non-immunogenic, and non-toxic platforms for optical imaging. In a previous *in vitro* study, we demonstrated human cells remained viable after incubation with NETs [30]. While the biocompatibility of NETs needs to be ultimately established, Flower et al. reported no immune or allergic responses, even after multiple injections of ICG-loaded human-derived EGs into monkeys and rabbits [41].

While the *in vivo* circulation kinetics of NETs has yet to be determined, Hu et al., reported that 80 nm diameter nano-constructs, composed of a poly (lactic-co-glycolic acid) core coated with erythrocyte-derived membranes, were retained in mice blood for three days with circulation half-life of nearly 40 hrs [42]. Rahmer et al. demonstrated that EGs loaded with superparamagnetic iron oxide nanoparticles were detectable in mice blood 24 hrs after tail vain injection [43]. A mean circulation half-life of 21.6 days has been reported for unloaded autologously-derived EGs in healthy humans [44]. Bossa et al. reported detectable levels of autologously-derived EGs containing dexamethasone in plasma of humans at 14 days post-infusion [45]. In a recent study, Rao et al. demonstrated that erythrocyte-membrane coated Fe_3O_4 nanoparticles were retaind in mice circulation at 48 hours post injection [46].

NETs are constructed easily at non-extreme temperatures (in the range of 4-25°C) without the use of any major chemical synthesis procedures. They are also are highly cost effective and fabricated without the need for expensive equipment. Currently, only a few liposomal drugs, none with targeting capability and none with imaging capability, have been approved by the FDA for different clinical applications [47]. Other presently non-FDA approved nano-based platforms are in various phases of clinical studies, [48-49] emphasizing the importance of such constructs in biomedicine. NETs provide a new class of optical nano-constructs, and may have widespread implications in medicine, particularly in relation to imaging of different cancer types. Moreover, NETs offer the potential to overcome the existing limitations of ICG (i.e., short half-life and lack of targeting ability). Given the existing FDA-approved status of ICG as well as humanized antibodies (e.g., Herceptin, Perjeta, and Kadcyla which target the HER2 receptor) antibody-functionalized NETs may provide an excellent platform for clinical translation.

The focus of this study has been to show that the NETs could be functionalized with antibodies as targeting moieties, and subsequently, demonstrate the proof-of-principle that such functionalized NETs could be used for targeted NIR imaging of cancer cells expressing particular receptors (e.g., HER2). For ultimate *in vivo* applications, further important studies are needed. In particular, the concentration of ICG utilized in fabrication of the NETs will need to be optimized in order to maximize the fluorescence emission of the NETs. Another important step in that direction is to determine the circulation kinetics and biodistribution of NETs. Finally, the effectiveness of functionalized NETs for cancer imaging will need to be validated in animal models. We

are currently pursuing such studies, and will be reporting the results as they become available.

1.5 Conclusion

We have demonstrated the successful engineering of erythrocyte-derived nanoparticles doped with ICG, and their surface functionalization with antibodies. Our experimental results demonstrate the effectiveness of NETs functionalized with anti-HER2 in targeted imaging of HER2 expressing cancer cells in vitro.

1.6 References

1. Frangioni, J. V., In vivo near-infrared fluorescence imaging. *Curr Opin Chem Biol* **2003,** *7* (5), 626-634. DOI: 10.1016/j.cbpa.2003.08.007.

2. Cheong, W. F.; Prahl, S. A.; Welch, A. J., A Review of the Optical-Properties of Biological Tissues. *Ieee J Quantum Elect* **1990,** *26* (12), 2166-2185. DOI: Doi 10.1109/3.64354.

3. Hilderbrand, S. A.; Kelly, K. A.; Niedre, M.; Weissleder, R., Near infrared fluorescence-based bacteriophage particles for ratiometric pH imaging. *Bioconjugate Chem* **2008,** *19* (8), 1635-1639. DOI: 10.1021/bc800188p.

4. Yannuzzi, L. A., Indocyanine Green Angiography: A Perspective on Use in the Clinical Setting. *Am J Ophthalmol* **2011,** *151* (5), 745-751. DOI: 10.1016/j.ajo.2011.01.043.

5. Hirche, C.; Murawa, D.; Mohr, Z.; Kneif, S.; Hunerbein, M., ICG fluorescence-guided sentinel node biopsy for axillary nodal staging in breast cancer. *Breast Cancer Res Treat* **2010,** *121* (2), 373-8. DOI: 10.1007/s10549-010-0760-z.

6. Sevick-Muraca, E. M.; Sharma, R.; Rasmussen, J. C.; Marshall, M. V.; Wendt, J. A.; Pham, H. Q.; Bonefas, E.; Houston, J. P.; Sampath, L.; Adams, K. E.; Blanchard, D. K.; Fisher, R. E.; Chiang, S. B.; Elledge, R.; Mawad, M. E., Imaging of lymph flow in breast cancer patients after microdose administration of a near-infrared fluorophore: feasibility study. *Radiology* **2008,** *246* (3), 734-41. DOI: 10.1148/radiol.2463070962.

7. Crane, L. M.; Themelis, G.; Arts, H. J.; Buddingh, K. T.; Brouwers, A. H.; Ntziachristos, V.; van Dam, G. M.; van der Zee, A. G., Intraoperative near-infrared fluorescence imaging for sentinel lymph node detection in vulvar cancer: first clinical results. *Gynecol Oncol* **2011,** *120* (2), 291-5. DOI: 10.1016/j.ygyno.2010.10.009.

8. van der Vorst, J. R.; Schaafsma, B. E.; Verbeek, F. P.; Swijnenburg, R. J.; Hutteman, M.; Liefers, G. J.; van de Velde, C. J.; Frangioni, J. V.; Vahrmeijer, A. L., Dose optimization for near-infrared fluorescence sentinel lymph node mapping in patients with melanoma. *Br J Dermatol* **2013,** *168* (1), 93-8. DOI: 10.1111/bjd.12059.

9. Jeschke, S.; Lusuardi, L.; Myatt, A.; Hruby, S.; Pirich, C.; Janetschek, G., Visualisation of the lymph node pathway in real time by laparoscopic radioisotope- and fluorescence-guided sentinel lymph node dissection in prostate cancer staging. *Urology* **2012,** *80* (5), 1080-6. DOI: 10.1016/j.urology.2012.05.050.

10. Zaidi, H. A.; Abla, A. A.; Nakaji, P.; Chowdhry, S. A.; Albuquerque, F. C.; Spetzler, R. F., Indocyanine green angiography in the surgical management of cerebral arteriovenous malformations: lessons learned in 130 consecutive cases. *Neurosurgery* **2014,** *10 Suppl 2*, 246-51; discussion 251. DOI: 10.1227/neu.0000000000000318.

11. Roessler, K.; Krawagna, M.; Dorfler, A.; Buchfelder, M.; Ganslandt, O., Essentials in intraoperative indocyanine green videoangiography assessment for intracranial aneurysm surgery: conclusions from 295 consecutively clipped aneurysms and review of the literature. *Neurosurg Focus* **2014,** *36* (2), E7. DOI: 10.3171/2013.11.focus13475.

12. Kraft, J. C.; Ho, R. J., Interactions of indocyanine green and lipid in enhancing near-infrared fluorescence properties: the basis for near-infrared imaging in vivo. *Biochemistry* **2014,** *53* (8), 1275-83. DOI: 10.1021/bi500021j.

13. Toyota, T.; Fujito, H.; Suganami, A.; Ouchi, T.; Ooishi, A.; Aoki, A.; Onoue, K.; Muraki, Y.; Madono, T.; Fujinami, M.; Tamura, Y.; Hayashi, H., Near-infrared-fluorescence imaging of lymph nodes

by using liposomally formulated indocyanine green derivatives. *Bioorg Med Chem* **2014,** *22* (2), 721-7. DOI: 10.1016/j.bmc.2013.12.026.

14. Wu, L.; Fang, S.; Shi, S.; Deng, J.; Liu, B.; Cai, L., Hybrid polypeptide micelles loading indocyanine green for tumor imaging and photothermal effect study. *Biomacromolecules* **2013,** *14* (9), 3027-33. DOI: 10.1021/bm400839b.

15. Yaseen, M. A.; Yu, J.; Wong, M. S.; Anvari, B., Stability assessment of indocyanine green within dextran-coated mesocapsules by absorbance spectroscopy. *J Biomed Opt* **2007,** *12* (6), 064031. DOI: 10.1117/1.2821423.

16. Kester, M.; Heakal, Y.; Fox, T.; Sharma, A.; Robertson, G. P.; Morgan, T. T.; Altinoglu, E. I.; Tabakovic, A.; Parette, M. R.; Rouse, S. M.; Ruiz-Velasco, V.; Adair, J. H., Calcium phosphate nanocomposite particles for in vitro imaging and encapsulated chemotherapeutic drug delivery to cancer cells. *Nano Lett* **2008,** *8* (12), 4116-21. DOI: 10.1021/nl802098g.

17. Sharma, P.; Bengtsson, N. E.; Walter, G. A.; Sohn, H. B.; Zhou, G.; Iwakuma, N.; Zeng, H.; Grobmyer, S. R.; Scott, E. W.; Moudgil, B. M., Gadolinium-doped silica nanoparticles encapsulating indocyanine green for near infrared and magnetic resonance imaging. *Small* **2012,** *8* (18), 2856-68. DOI: 10.1002/smll.201200258.

18. Kim, G.; Huang, S. W.; Day, K. C.; O'Donnell, M.; Agayan, R. R.; Day, M. A.; Kopelman, R.; Ashkenazi, S., Indocyanine-green-embedded PEBBLEs as a contrast agent for photoacoustic imaging. *J Biomed Opt* **2007,** *12* (4), 044020. DOI: 10.1117/1.2771530.

19. Bahmani, B.; Lytle, C. Y.; Walker, A. M.; Gupta, S.; Vullev, V. I.; Anvari, B., Effects of nanoencapsulation and PEGylation on biodistribution of indocyanine green in healthy mice: quantitative fluorescence imaging and analysis of organs. *Int J Nanomedicine* **2013,** *8*, 1609-20. DOI: 10.2147/ijn.s42511.

20. Gutierrez Millan, C.; Colino Gandarillas, C. I.; Sayalero Marinero, M. L.; Lanao, J. M., Cell-based drug-delivery platforms. *Therapeutic delivery* **2012,** *3* (1), 25-41.

21. Antonelli, A.; Magnani, M., Red blood cells as carriers of iron oxide-based contrast agents for diagnostic applications. *J Biomed Nanotechnol* **2014,** *10* (9), 1732-50.

22. Agrawal, V.; Woo, J. H.; Borthakur, G.; Kantarjian, H.; Frankel, A. E., Red blood cell-encapsulated L-asparaginase: potential therapy of patients with asparagine synthetase deficient acute myeloid leukemia. *Protein Pept Lett* **2013,** *20* (4), 392-402.

23. Hu, C.-M. J.; Fang, R. H.; Zhang, L., Erythrocyte-Inspired Delivery Systems. *Advanced Healthcare Materials* **2012,** *1* (5), 537-547. DOI: doi:10.1002/adhm.201200138.

24. Muzykantov, V. R., Drug delivery by red blood cells: vascular carriers designed by mother nature. *Expert Opin Drug Deliv* **2010,** *7* (4), 403-27. DOI: 10.1517/17425241003610633.

25. Yoo, J. W.; Irvine, D. J.; Discher, D. E.; Mitragotri, S., Bio-inspired, bioengineered and biomimetic drug delivery carriers. *Nat Rev Drug Discov* **2011,** *10* (7), 521-35. DOI: 10.1038/nrd3499.

26. Bentley, A. A.; Adams, J. C., The Evolution of Thrombospondins and Their Ligand-Binding Activities. *Mol Biol Evol* **2010,** *27* (9), 2187-2197. DOI: 10.1093/molbev/msq107.

27. Oldenborg, P. A.; Zheleznyak, A.; Fang, Y. F.; Lagenaur, C. F.; Gresham, H. D.; Lindberg, F. P., Role of CD47 as a marker of self on red blood cells. *Science* **2000,** *288* (5473), 2051-2054. DOI: DOI 10.1126/science.288.5473.2051.

28. Oldenborg, P. A., CD47: A Cell Surface Glycoprotein Which Regulates Multiple Functions of Hematopoietic Cells in Health and Disease. *ISRN Hematol.* **2013,** *2013*, 614619. DOI: 10.1155/2013/614619.

29. Rodriguez, P. L.; Harada, T.; Christian, D. A.; Pantano, D. A.; Tsai, R. K.; Discher, D. E., Minimal "Self" Peptides That Inhibit Phagocytic Clearance and Enhance Delivery of Nanoparticles. *Science* **2013,** *339* (6122), 971-975. DOI: 10.1126/science.1229568.

30. Bahmani, B.; Bacon, D.; Anvari, B., Erythrocyte-derived photo-theranostic agents: hybrid nano-vesicles containing indocyanine green for near infrared imaging and therapeutic applications. *Sci Rep-Uk* **2013,** *3*. DOI: ARTN 2180

10.1038/srep02180.

31. Yan, M.; Parker, B. A.; Schwab, R.; Kurzrock, R., HER2 aberrations in cancer: implications for therapy. *Cancer Treat Rev* **2014,** *40* (6), 770-80. DOI: 10.1016/j.ctrv.2014.02.008.

32. English, D. P.; Roque, D. M.; Santin, A. D., HER2 expression beyond breast cancer: therapeutic implications for gynecologic malignancies. *Mol Diagn Ther* **2013,** *17* (2), 85-99. DOI: 10.1007/s40291-013-0024-9.

33. Fang, R. H.; Hu, C. M.; Chen, K. N.; Luk, B. T.; Carpenter, C. W.; Gao, W.; Li, S.; Zhang, D. E.; Lu, W.; Zhang, L., Lipid-insertion enables targeting functionalization of erythrocyte membrane-cloaked nanoparticles. *Nanoscale* **2013,** *5* (19), 8884-8. DOI: 10.1039/c3nr03064d.

34. Delord, J. P.; Allal, C.; Canal, M.; Mery, E.; Rochaix, P.; Hennebelle, I.; Pradines, A.; Chatelut, E.; Bugat, R.; Guichard, S.; Canal, P., Selective inhibition of HER2 inhibits AKT signal transduction and prolongs disease-free survival in a micrometastasis model of ovarian carcinoma. *Ann. Oncol.* **2005,** *16* (12), 1889-97. DOI: 10.1093/annonc/mdi405.

35. Tolmachev, V.; Wallberg, H.; Sandstrom, M.; Hansson, M.; Wennborg, A.; Orlova, A., Optimal specific radioactivity of anti-HER2 Affibody molecules enables discrimination between xenografts with high and low HER2 expression levels. *Eur J Nucl Med Mol Imaging* **2011,** *38* (3), 531-9. DOI: 10.1007/s00259-010-1646-3.

36. Jung, B. S.; Vullev, V. I.; Anvari, B., Revisiting Indocyanine Green: Effects of serum and physiological temperature on absorption and fluorescence characteristics. *IEEE J. Sel. Top. Quant.* **2014,** *20* (2). DOI: 10.1109/jstqe.2013.2278674.

37. Mahl, D.; Greulich, C.; Meyer-Zaika, W.; Koller, M.; Epple, M., Gold nanoparticles: dispersibility in biological media and cell-biological effect. *Journal of Materials Chemistry* **2010,** *20* (29), 6176-6181. DOI: 10.1039/C0JM01071E.

38. Allouni, Z. E.; Cimpan, M. R.; Hol, P. J.; Skodvin, T.; Gjerdet, N. R., Agglomeration and sedimentation of TiO2 nanoparticles in cell culture medium. *Colloids and surfaces. B, Biointerfaces* **2009,** *68* (1), 83-7. DOI: 10.1016/j.colsurfb.2008.09.014.

39. Tadros, T., Steric Stabilization. In *Encyclopedia of Colloid and Interface Science*, Tadros, T., Ed. Springer Berlin Heidelberg: Berlin, Heidelberg, 2013; pp 1048-1049. DOI: 10.1007/978-3-642-20665-8_146.

40. Kittler, S.; Greulich, C.; Gebauer, J. S.; Diendorf, J.; Treuel, L.; Ruiz, L.; Gonzalez-Calbet, J. M.; Vallet-Regi, M.; Zellner, R.; Koller, M.; Epple, M., The influence of proteins on the dispersability and cell-biological activity of silver nanoparticles. *Journal of Materials Chemistry* **2010,** *20* (3), 512-518. DOI: 10.1039/B914875B.

41. Flower, R.; Peiretti, E.; Magnani, M.; Rossi, L.; Serafini, S.; Gryczynski, Z.; Gryczynski, I., Observation of Erythrocyte Dynamics in the Retinal Capillaries and Choriocapillaris Using ICG-Loaded Erythrocyte Ghost Cells. *Invest Ophth Vis Sci* **2008,** *49* (12), 5510-5516. DOI: 10.1167/iovs.07-1504.

42. Hu, C. M. J.; Zhang, L.; Aryal, S.; Cheung, C.; Fang, R. H.; Zhang, L. F., Erythrocyte membrane-camouflaged polymeric nanoparticles as a biomimetic delivery platform. *P Natl Acad Sci USA* **2011,** *108* (27), 10980-10985. DOI: 10.1073/pnas.1106634108.

43. Rahmer, J.; Antonelli, A.; Sfara, C.; Tiemann, B.; Gleich, B.; Magnani, M.; Weizenecker, J.; Borgert, J., Nanoparticle encapsulation in red blood cells enables blood-pool magnetic particle imaging hours after injection. *Phys Med Biol* **2013,** *58* (12), 3965-3977. DOI: 10.1088/0031-9155/58/12/3965.

44. Bax, B. E.; Bain, M. D.; Talbot, P. J.; Parker-Williams, E. J.; Chalmers, R. A., Survival of human carrier erythrocytes in vivo. *Clin Sci* **1999,** *96* (2), 171-178. DOI: Doi 10.1042/Cs19980229.

45. Bossa, F.; Latiano, A.; Rossi, L.; Magnani, M.; Palmieri, O.; Dallapiccola, B.; Serafini, S.; Damonte, G.; De Santo, E.; Andriulli, A.; Annese, V., Erythrocyte-Mediated Delivery of Dexamethasone in Patients With Mild-to-Moderate Ulcerative Colitis, Refractory to Mesalamine: A Randomized, Controlled Study. *Am J Gastroenterol* **2008,** *103* (10), 2509-2516. DOI: 10.1111/j.1572-0241.2008.02103.x.

46. Rao, L.; Bu, L. L.; Xu, J. H.; Cai, B.; Yu, G. T.; Yu, X.; He, Z.; Huang, Q.; Li, A.; Guo, S. S.; Zhang, W. F.; Liu, W.; Sun, Z. J.; Wang, H.; Wang, T. H.; Zhao, X. Z., Red Blood Cell Membrane as a Biomimetic Nanocoating for Prolonged Circulation Time and Reduced Accelerated Blood Clearance. *Small* **2015,** *11* (46), 6225-36. DOI: 10.1002/smll.201502388.

47. Shi, J. J.; Xiao, Z. Y.; Kamaly, N.; Farokhzad, O. C., Self-Assembled Targeted Nanoparticles: Evolution of Technologies and Bench to Bedside Translation. *Accounts Chem Res* **2011,** *44* (10), 1123-1134. DOI: 10.1021/ar200054n.

48. Kamaly, N.; Xiao, Z. Y.; Valencia, P. M.; Radovic-Moreno, A. F.; Farokhzad, O. C., Targeted polymeric therapeutic nanoparticles: design, development and clinical translation. *Chem Soc Rev* **2012,** *41* (7), 2971-3010. DOI: 10.1039/c2cs15344k.

49. Peer, D.; Karp, J. M.; Hong, S.; Farokhzad, O. C.; Margalit, R.; Langer, R., Nanocarriers as an emerging platform for cancer therapy. *Nat. Nanotechnol.* **2007,** *2* (12), 751-760. DOI: 10.1038/nnano.2007.387.

Chapter 2. Erythrocyte-Derived Optical Nano-Probes Doped with ICG-Bound Albumin: Material Characteristics and Preliminary Evaluation for Cancer Cell Imaging

2.1 Abstract

Nano-sized structures activated by near infrared (NIR) photo-excitation can provide an optical platform for image-guided removal of small tumor nodules. We have engineered nanoparticles derived from erythrocytes that can be doped with NIR fluorophore, indocyanine green (ICG). We refer to these constructs as NIR erythrocyte-derived transducers (NETs). The objective of this study was to determine if ICG bound albumin (IbA), as the doping material, could enhance the fluorescence emission of NETs, and evaluate the capability of these nano-probes in imaging cancer cells. Erythrocytes were isolated from bovine whole blood and depleted of hemoglobin to form erythrocyte ghosts (EGs). EGs were then extruded through nano-sized porous membranes in the presence of 10-100 μm ICG or ICG:albumin (1:1 molar ratio) to form ICG- or IbA-doped NETs. The resulting nano-sized constructs were characterized for their diameters, zeta potentials, absorption, and fluorescence emission spectra. We used fluorescence microscopic imaging to evaluate the capability of the constructs in imaging SKOV3 ovarian cancer cells. Based on dynamic light scattering measurements, ICG- and IbA-doped NETs had similar diameter distributions (z-average diameter of 236 and 238 nm, respectively) in phosphate buffer saline supplemented with 10% fetal bovine serum, which remained nearly constant over the course of two hours at 37°C. Despite a much lower loading

efficiency of IbA (≈ 0.7 – 8%) as compared to ICG (10 – 45%), the integrated normalized fluorescence emission of IbA-NETs was two to sixfold higher than ICG-doped NETs. IbA-NETs also demonstrated an enhanced capability in fluorescence imaging of SKOV3 ovarian cancer cells, and can serve as potentially effective nano-probes for fluorescence imaging of cancerous cells.

2.2 Introduction

Near infrared (NIR) fluorescent molecules and nano-sized structures can provide a capability for use in image-guided surgery, particularly as applied to removal of tumors.[1-3] To-date, indocyanine green (ICG) remains as the only FDA-approved NIR fluorophore. The utility of ICG in sentinel lymph node mapping, and cancer staging and imaging is under studies by many investigators.[4-6]

Despite its usage in clinical practice, two key drawbacks of ICG are: (1) its short plasma half-life (≈ 2-3 minutes), resulting from interactions with blood proteins, particularly albumin, and other macromolecules;[7-10] and (2) relatively weak fluorescence emission. To shield ICG from binding to blood macromolecules, and subsequently, increase its circulation time, ICG has been encapsulated into a variety of nano-sized structures composed of such materials as liposomes,[11-12] silica,[13] plant-virus,[14] and polymers.[15]

As an alternative to such encapsulating materials, mammalian cells including erythrocytes, stem cells, and lymphocytes are receiving increasing interest as a delivery platform for therapeutics or imaging agents.[16-25] Erythrocytes, in particular, are

advantageous because of their naturally long circulation time of 90-120 days.[26-27] The plasma membrane of erythrocytes contains particular moieties such as the CD47 protein which can impede recognition by cells of the immune system.[26-28] Therefore, autologous erythrocytes or those obtained from compatible blood types may present a promising biocompatible platform for encapsulation of ICG to increase its circulation time and bioavailability. For example, Hu et al., reported that polymeric nano-constructs, coated with erythrocyte-derived membranes, were retained in mice blood for three days with circulation half-life of nearly 8 hours.[29] Domenech et al. reported that circulating erythrocytes loaded with L-asparaginase were still detectable within the vasculature at 24 days following the first injection.[30] Bossa et al. reported detectable levels of autologously-derived EGs containing dexamethasone in plasma of humans at 14 days post-infusion.[31]

A second drawback of ICG is related to its relatively low fluorescence emission. ICG in aqueous solution tends to aggregate (at concentrations ≈ >15 μM), and exhibits self-quenching, resulting in relatively low fluorescence quantum yield (≈ 2.5% in water).[32-33] The binding of ICG to albumin has been exploited as a method to reduce self-aggregation and increases fluorescence by two to threefold.[5, 16, 33-35]

Our group previously reported the first results in the engineering of erythrocyte-derived nanoparticles doped with ICG as theranostic agents for targeted fluorescent imaging[36] and photothermal destruction of human cells.[37] We refer to these constructs as NIR Erythrocyte-derived Transducers (NETs). As a method to increase the fluorescence emission of NETs, herein we investigate the effects of ICG-bound albumin (IbA) as the

doping material. We refer to these constructs as IbA-NETs, and evaluate their performance in fluorescence imaging of ovarian cancer cells *in vitro*. To the best of our knowledge, this is the first study to quantitatively compare the fluorescence characteristics and cancer cell imaging capability of NETs doped with ICG or IbA. We emphasize that this is not an *in vivo* study of using IbA-NETs in fluorescence imaging of tumors implanted in animal models. Instead, our objectives in this manuscript are to: (1) demonstrate the engineering and fabrication of these nano-sized probes doped with IbA; (2) present some of their key physical and optical properties; (3) provide quantitative information on their fluorescence characteristics, particularly as a function of the concentration of IbA as the doping agent; (4) quantify the enhancement in fluorescence emission of IbA-NETs as compared to NETs doped with ICG; and (5) demonstrate their capability in enhanced fluorescence imaging of tumor cells *in vitro* as compared to NETs doped with ICG alone. These nano-probes fabricated with appropriate material properties and characteristics can subsequently be investigated for their potential in tumor imaging in relevant animal models. This study is the first step in that direction.

2.3 Materials and Methods

2.2.1 Reagents and Cell Lines

We obtained the following reagents from commercial sources: bovine whole blood (Rockland Immunochemicals, Inc., Limerick, PA), phosphate buffered saline (PBS) (Fisher BioReagents, Hampton, NH), indocyanine green (ICG) (MP Biomedicals, Santa Ana, CA), bovine serum albumin (BSA) (Sigma–Aldrich, St. Louis, MO),

Penicillin/Streptomycin (ATCC, Manassas, VA), Tween-20 (Sigma–Aldrich, St. Louis, MO), 4',6-diamidino-2-phenylindole (DAPI) (Thermo Fisher Scientific, Waltham, MA). We used SKOV3 Ovarian Cancer Cell line (ATCC®, Manassas, VA) grown in Roswell Park Memorial Institute (RPMI 1640) medium supplemented with 10% fetal bovine serum (FBS), and 1% Penicillin/Streptomycin (Corning Inc., Corning, NY).

2.2.2 Fabrication of NETs and IbA-NETs

Erythrocytes were isolated from whole bovine blood and washed in ≈310 mOsm PBS (referred to as the 1X PBS solution). Packed erythrocytes were subject to hypotonic (≈80 mOsm) treatment to deplete the hemoglobin content of the cell, resulting in erythrocyte ghosts (EGs). EGs were stored in 1X PBS at 4°C up to two weeks until NETs fabrication. EGs were mixed with prepared concentrations of ICG in the range of 10 – 100 μM, or IbA complex (using the same ICG concentration range and in 1:1 molar ratio), and extruded sequentially through 400, 200 and 100 nm diameter porous membranes (Avanti Polar Lipids, Inc., Alabaster, Alabama). We define the loading buffer during extrusion as 9 parts 1X PBS containing EGs, and 1 part ICG or IbA in water where the overall solution is nearly isotonic at 0.9X PBS. The resulting NETs or IbA-NETs suspensions were then centrifuged and washed twice with 1X PBS (Figure 2.1).

2.2.3 Time-Dependent Measurements of NETs Diameters

NETs and IbA-NETs were incubated in 1X PBS supplemented with 10% FBS in PBS for up to two hours at 37°C. At specific time (t) points ($t = 0^+$, 20, 40, 60, 120 minutes), samples were drawn and their diameters were measured using the dynamic light

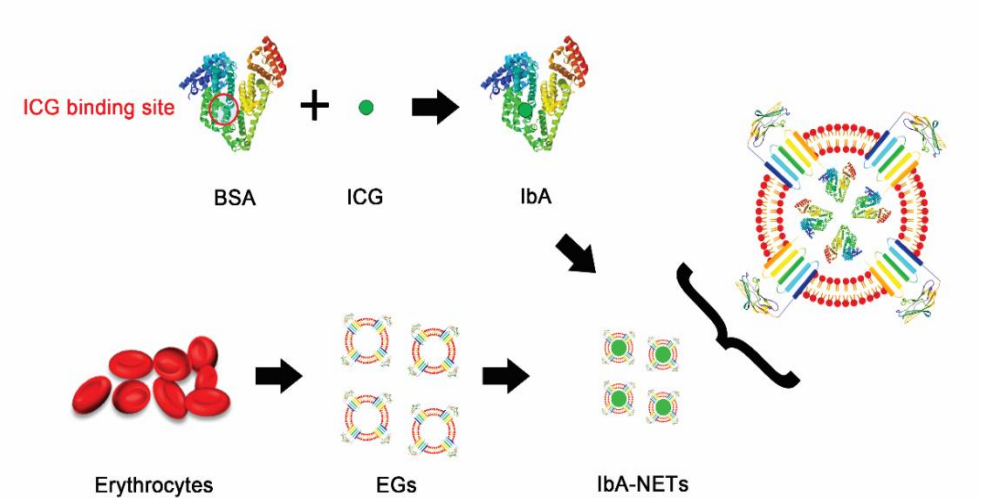

Figure 2.1: NETs fabrication. ICG was mixed with BSA (1:1 molar ratio) prior to encapsulation into IbA-NETs.

scattering (DLS) method (Zetasizer Nanoseries, NanoZS90, Malvern Instruments, Malvern, UK). Measurements were repeated three times for each sample. We report the Z-average diameter, which is the intensity-based harmonic mean of the light-scattering particles, and the Lognormal fits to the measurements.

2.2.4 Characterization of NETs and IbA-NETs

The zeta potentials of NETs and IbA-NETs suspended in 1X PBS were determined by electrophoretic light scattering (Zetasizer Nanoseries, NanoZS90, Malvern Instruments, Malvern, UK). Absorption spectra of NETs and IbA-NETs were obtained using a UV-Visible spectrophotometer (Cary 50 UV-Vis spectrophotometer, Agilent Technologies, Santa Clara, CA) with optical path length of 1 cm. Each individual absorption spectrum was normalized to its absorbance value at 280 nm to account for the loss of erythrocyte membrane materials during fabrication process.

The fluorescence spectra of NETs and IbA-NETs were acquired in response to photo-excitation at 720 ± 2.5 nm wavelength using a 450W xenon lamp, and recorded by a fluorimeter (Fluorolog-3 spectrofluorometer, Edison, NJ). We obtained the normalized fluorescence spectra $\zeta(\lambda)$ as:

$$\zeta(\lambda) = \frac{F(\lambda)}{[1-10^{-A(\lambda_{ex})}]} \qquad (1)$$

where $F(\lambda)$ is the recorded emission intensity at wavelength λ, and $A(\lambda_{ex})$ is the absolute absorbance value of the sample at excitation wavelength λ_{ex}. We quantified the integrated normalized fluorescence emission ζ^* as:

$$\zeta^* = \int_{735}^{900} \zeta(\lambda) d\lambda \qquad (2)$$

Finally, we present the fluorescence enhancement of IbA-NETs, E, as:

$$E = \frac{\zeta^*_{(IbA-NETs)}}{\zeta^*_{(NETs)}} \qquad (3)$$

2.2.5 Effective Concentration and Encapsulation Efficiency

We define the effective concentration of ICG or IbA as the concentration of these agents loaded into a given population of NETs. Thus, the effective concentration of ICG or IbA within NETs is an estimate of the concentration of ICG or IbA that would be dispersed in solution if NETs were disintegrated to release their ICG or IbA content. We estimated these values by comparing the monomeric peak absorbance values of NETs or IbA-NETs to an absorbance vs. concentration calibration curve of ICG or IbA in water. We chose

water as the solvent used in calibration since the absorption spectrum of ICG encapsulated in erythrocyte-derived nanoparticles closely resembles that of free ICG in water at low concentrations (≈ < 14 μM) as opposed to that of ICG in 1X PBS. We calculated encapsulation efficiency, η (%), as:

$$\eta(\%) = \frac{[ICG]_{effective}}{[ICG]_{loading}} \times 100 \quad (4)$$

where $[ICG]_{loading}$ is the concentration of ICG within the loading buffer during extrusion.

2.2.6 Fluorescence Imaging

We incubated NETs and IbA-NETs with SKOV3 ovarian cancer cells as model cancer cells. We added 200 μl of SKOV3 cell suspension (≈ 10^6 cells/ml) in RPMI 1640 medium supplemented with 10% FBS, and 1% Penicillin/Streptomycin to each well of a 96-well plate. Cell suspensions were plated in 5% CO_2 overnight. All samples were diluted to have absorbance value of one at the spectral peak. On the following day, the cells were washed and incubated with various agents consisting of 1X PBS, free ICG (≈13.1 μM), free IbA (≈14.2 μM), NETs, or IbA-NETs, in separate wells for two hours in the dark at 37 °C. After incubation, cells were subsequently washed twice with 1X PBS and fixed using 4% paraformaldehyde, permeabilized with 2% Tween-20, and finally incubated with DAPI for 5 minutes to stain the nuclei for fluorescence imaging.

NIR fluorescence emission (> 770 nm) in response to 740 ± 30 nm excitation by a Nikon halogen lamp was captured by an electron multiplier gained CCD camera (Quant EM-CCD, C9100-14 Hamamatsu, Shizuoka-ken, Japan). The camera exposure time was

set at 0.7 s. Fluorescence emission from DAPI-stained nuclei in the range of 435–485 nm was collected in response to 360 ± 20 nm excitation by the Nikon halogen lamp. We present falsely-colored microscopic fluorescent images as the overlay of the NIR emission due to ICG (red channel), and visible emission due to DAPI (blue channel).

2.2.7 Quantification of Fluorescence Imaging

The acquired fluorescence images were analyzed using ImageJ software. Background baseline fluorescence emission intensity of SKOV3 cells in media without incubation with NETs or IbA-NETs was subtracted from the those associated with cells in media but incubated with NETs or IbA-NETs. The resulting mean total fluorescence emission intensity $\bar{I}$ values were then calculated as:

$$\overline{I} = \frac{\sum_{i=1}^{n}\sum_{j=1}^{m} I_j}{n} \qquad (5)$$

where m is the total number of pixels in an image, I_j is the fluorescence emission intensity at the j^{th} pixel of an image, and n corresponds to the number of images acquired.

2.3 Results

Hydrodynamic distribution profiles of NETs and IbA-NETs fabricated using 50 μM ICG or IbA in the loading buffer, and measured in 37 °C PBS supplemented with 10% FBS immediately after incubation are presented in Figure 2.2A. The Z-average diameters for these NETs and IbA-NETs were ≈ 236 nm and 238 nm, respectively.

In Figure 2.2B, we present the Z-average diameter of NETs and IbA-NETs as a function of incubation time in 37 °C PBS supplemented with 10%, fabricated using fabricated using 50 µM and 100 µM ICG or IbA in the loading buffer. There were no statistically significant differences in Z-average diameter values among the samples at a given incubation time point, or as a function of incubation time. The Z-average diameter values normalized to the respective values for NETs and IbA-NETs fabricated at 50 and 100 µM at time $t = 0$ remained at nearly one for all samples (inset Figure 2.2B).

The mean ± standard deviation (SD) zeta-potential values for erythrocytes, EGs, free IbA, NETs and IbA-NETs were ≈ -12.37±1.70 mV, -11.07±0.66 mV, -12.77± 2.63 mV, -11.87±0.40 mV and -11.57±0.30 mV, respectively. Statistical analysis showed that the mean values of the zeta potentials for these populations were not significantly different from each other.

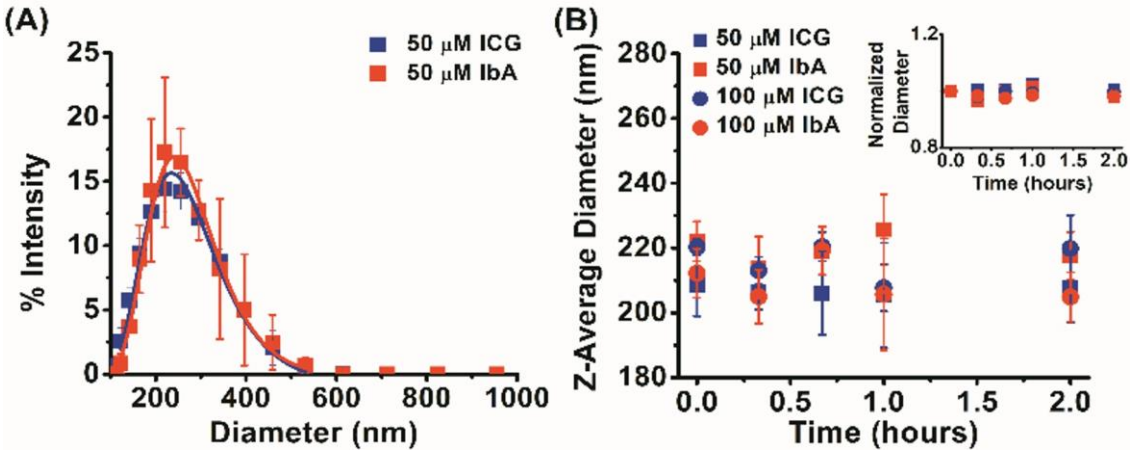

Figure 2.2: Hydrodynamic diameters of NETs and IbA-NETs incubated at 37 °C PBS supplemented with 10% FBS measured by DLS method. (A) Diameter profiles of NETs and IbA-NETs fabricated using 50 µM ICG or IbA immediately after incubation (t = 0). Profiles were fitted by Lognormal functions. (B) Z-average diameters as a function of incubation time (t = 0, 20, 40, 60, 120 minutes) for NETs and IbA-NETs fabricated using 50 µM and 100 µM ICG or IbA. Inset shows the Z-average diameter values normalized to the respective values for NETs and IbA-NETs fabricated at 50 and 100 µM at t = 0. DLS measurements were done in triplicates for each sample. Error bars represent standard deviations associated with each measurement.

Normalized absorption spectra for NETs and IbA-NETs fabricated at various respective concentrations of ICG or IbA are presented in Figure 2.3A. We attribute the absorption at 280 nm to tyrosine and tryptophan residues in membrane proteins and BSA. Absorbance values in the range of 600-900 nm increased as higher concentrations of ICG were used to fabricate the NETs. The primary peak at 800 nm is associated with the monomer form of ICG encapsulated in NETs.[36-38] The normalized absorbance values at 808 nm spectral peak is associated with the monomeric form of ICG in NETs, and increased from 0.1 to 0.9 as the ICG concentration in the loading buffer increased from 10 μM to 100 μM. For ICG loading concentrations greater than 20 μM, a shoulder in the spectral range of 650-750 nm emerged for NETs. Absorption over this shoulder is associated with H-like aggregate forms of ICG.[35-38] With increasing ICG concentrations above 20 μM, the absorbance values over the spectral shoulder increased, suggesting that progressively higher fractions of H-like aggregates were within the NETs.

The normalized absorbance values of the monomer form of ICG in IbA-NETs on the other hand, reached a maximum normalized absorbance of 0.15 regardless of IbA concentration in the loading buffer increasing from 50 μM to 100 μM. The absence of a pronounced spectral shoulder suggests that there were none or minimal levels of H-like aggregate forms of ICG in IbA-NETs. This result further suggests that ICG molecules were bound onto albumin, preventing formation of aggregates.

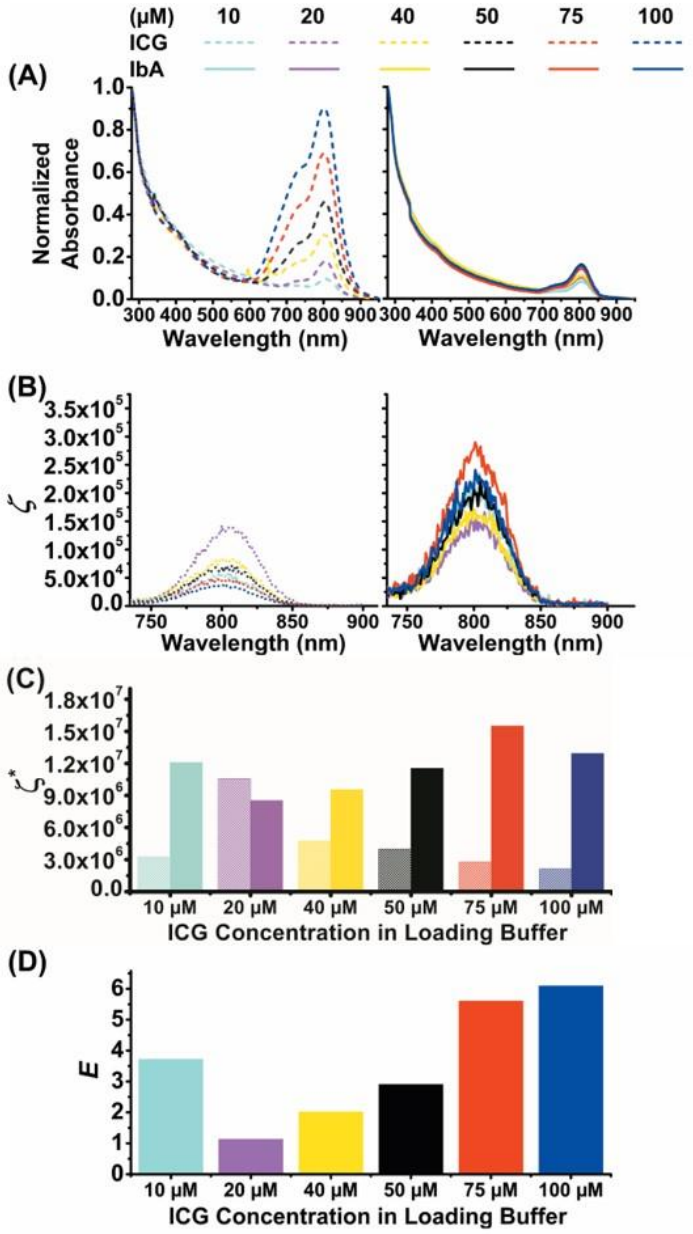

Figure 2.3: (A) Absorption spectra with each spectrum normalized to its 280 nm absorbance value, (B) normalized fluorescence emission spectra (ζ) (see equation 1), (C) Spectrally integrated values of the normalized fluorescence emission spectra (ζ^*) (see equation 2), and (D) fluorescence enhancement value (E) by IbA-NETs (see equation 3). Excitation wavelength for the results shown in Figures 2B-2D was 720±2.5 nm.

The normalized fluorescence emission spectra, ζ, of NETs and IbA-NETs were recorded in response to 720±2.5 nm photo-excitation (Figure 2.3B). The emission peak at 798 nm for NETs is associated with the monomeric form of ICG, and was

bathochromically shifted to 804 nm for IbA-NETs. There was a non-linear change in the peak value of ζ when encapsulating increasing amounts of ICG alone, with maximal values observed when using ICG concentration of 20 µM ICG in the loading buffer.

Depending on the IbA concentration in the loading buffer, the peak value of ζ for IbA-NETs was two to three times higher than those NETs fabricated using the same ICG concentration (with the exception of when using 20 µM ICG and 20 µM IbA) (Figure 2.3B). Except for 20 µM ICG or 20 µM IbA, IbA-NETs showed higher values of ζ^* (Figure 2.3C). Highest values of ζ^* for NETs and IbA-NETs were obtained when using ICG and IbA concentrations of 10 and 75 µM, respectively. For IbA-NETs fabricated using 100 µM IbA, a sixfold enhancement in ζ^* was achieved as compared to NETs fabricated at the same ICG concentration (Figure 2.3D).

The encapsulation efficiency (η) of ICG in NETs increased from ≈ 10 to 45%, and appeared to approach a saturating value when using ICG concentration of 100 µM in the loading buffer (Figure 2.4A). Values of η ranged between 0.7 – 8 % for IbA-NETs, and

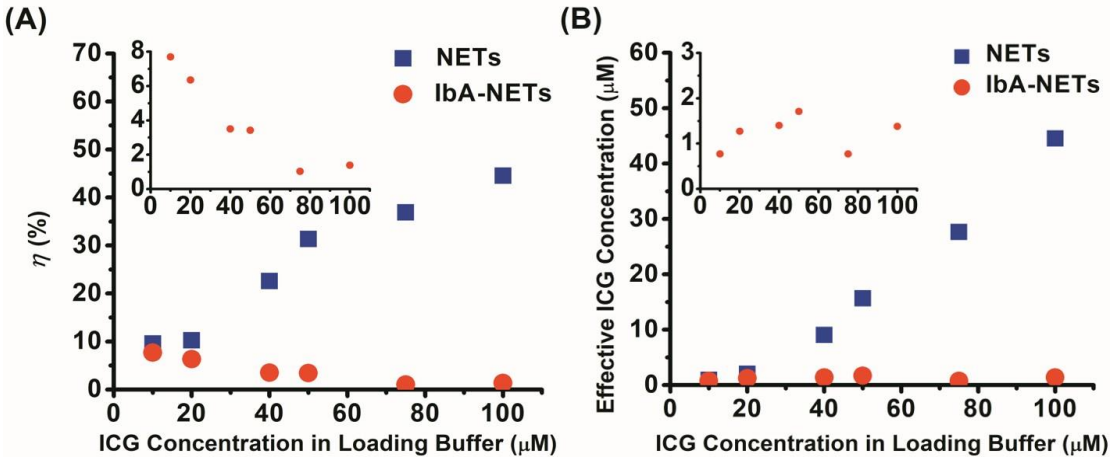

Figure 2.4: (A) Encapsulation efficiency (η) of NETs and IbA-NETs. (B) Effective ICG concentration loaded into NETs or IbA-NETs. Insets show the results for IbA-NETs on a smaller scale.

showed a decreasing trend with increased values of ICG concentration in the loading buffer. Correspondingly, the effective ICG concentration in NETs increased from ≈ 1 to 44 μM as the ICG concentration in loading buffer increased from 10 to 100 μM (Figure 2.4B). The effective ICG concentration loaded into IbA-NETs did not vary much (≈ 0.7 – 2 μM), regardless of ICG concentration in the loading buffer.

We performed *in vitro* fluorescence microscopic imaging of SKOV3 ovarian cancer cells. SKOV3 cells were incubated with control, free ICG, free IbA, NETs and IbA-NETs for two hours at 37°C (Figure 2.5A). There was minimal NIR fluorescence emission from SKOV3 cells incubated with free ICG or free IbA. Increased NIR fluorescence emission was detected from SKOV3 cells incubated with NETs and IbA-NETs. According to these images, NETs and IbA-NETs appeared to be localized within the cytosol of the cells.

Results of our quantitative analyses of the fluorescent images based on equation

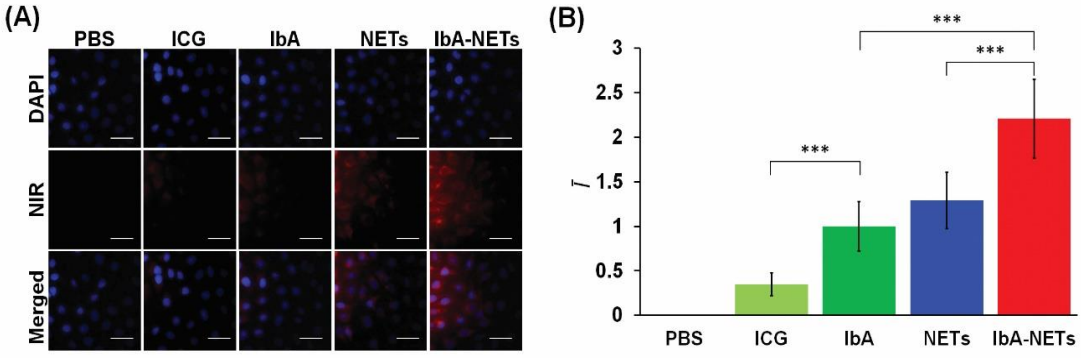

Figure 2.5: (A) Fluorescent images of SKOV3 cells incubated with media containing PBS, free ICG, free IbA, NETs and IbA-NETs at 37°C for two hours. Images were analyzed using ImageJ where DAPI was falsely-colored in blue and NIR fluorescence in red. (Scale bars = 50 μm) (B) Values of mean total fluorescence emission intensity obtained from images of SKOV3 cells incubated with the indicated agents. Asterisks indicate statistically significant differences among the indicated pairs ($p < 0.001$). Values of $\bar{I}$ are multiplied by 10^6, but not shown the Figure.

(5) are shown in Figure 5b. Value of mean total fluorescence emission intensity, $\bar{I}$, based on imaging by IbA-NETs was ≈ 2 times greater than that associated with NETs ($p <$ 0.001).

2.4 Discussion

NETs and IbA-NETs have similar diameter distribution profiles and Z-average diameter values that do not differ significantly with respect to each other or as a function of incubation time in 37 °C PBS supplemented with 10% FBS for up to two hours (Figure 2.2). The fact that the Z-average diameter of NETs and IbA-NETs were independent of the ICG or IbA concentration in the loading buffer (50 or 100 μM) suggests that these agents were localized within the interior of these nanoparticles. Considering that albumin is nearly 80 times larger than ICG (respective molecular weights of 65 kDa and 775 Da), membrane embedment of IbA would otherwise suggest an increase in the particle diameter.

Adsorption of albumin to erythrocyte membrane is a weak interaction that is easily reversible by the washing steps.[39] Therefore, any non-encapsulated IbA is likely removed during washing steps of the fabrication process. Since the Z-average diameter values of NETs and IbA-NETs did not significantly vary for up to two hours when incubated at 37 °C PBS supplemented with 10% FBS suggests that there were no aggregation effects at physiologically relevant conditions.. Another group has shown stability of nano-erythrosomes in serum for up to 96 hours.[40] Our results are also consistent with another study where a hard protein corona was not formed around

erythrocyte-derived nanoparticles after four hours of incubation in plasma, and that the diameter of particles remained stable when stored in serum for up to 15 days.[41]

An important physical feature influencing the biodistribution of nanoparticles is their surface charge.[18, 42] The zeta potential is related to the surface charge of the particle when dispersed in a particular medium. The zeta potential of erythrocytes, EGs, free IbA, NETs and IbA-NETs all fall around -11 mV in PBS, suggesting that the overall distributions of membrane constituents responsible for the surface charge remain unaltered despite the extrusion and loading processes. The negative zeta potential creates repulsive forces that prevent erythrocyte-erythrocyte and erythrocyte-macromolecules interactions.[43] The similar zeta potential of NETs and IbA-NETs suggest IbA is not exposed to the extracellular environment as it would alter the surface charge of IbA-NETs, further substantiating that IbA complex is not embedded within the membrane, but localized to the interior of the particle.

Maintaining the erythrocyte membrane composition responsible for surface charge has implications for extended circulation time of erythrocyte-derived constructs. The negative charge of erythrocytes prevents opsonization by serum proteins and further recognition by mononuclear phagocyte system (MPS).[22] Most of this negative charge is attributed to the membrane sialic acid constituents.[44-46]

A particular membrane protein that contributes to evading of erythrocytes by cells of the immune system is CD-47, commonly referred to as the “don’t eat me” protein.[26-28, 47-48] In a previous study, we showed evidence to support that CD47 remains present on the surface of NETs.[36] With their potential ability to evade the immune system as well as

the ability to functionalize their surface with targeting moieties,[36] NETs present a promising biomimetic platform for nanotheranostics.

Upon increasing the ICG concentration from 10 to 100 μM within the loading buffer, the absorption in the 600-900 spectral band for the fabricated NETs progressively increased. This result suggests that the NETs were able to continue accommodating the relatively small molecules of ICG (774 Da). As more ICG was introduced into the NETs, a spectral shoulder around 710 nm becomes more prominent, indicating the presence of greater H-like aggregate forms of ICG. For IbA-NETs, ICG was predominantly in its monomeric form as evidenced by a single spectral peak at 805 nm (Figure 2.3A). IbA-NETs exhibited a narrow NIR band with a bathochromic shift, suggesting that ICG existed in an altered conformation when bound to albumin.

We have previously reported on the absorption and fluorescence of ICG in water, cell culture medium, and cell culture medium supplemented with fetal bovine serum.[35] Here, we show that encapsulation of ICG or IbA into NETs results in peak absorptions at 798 and 804 nm, respectively. These spectral peaks represent bathochromic shifts of ≈ 7 and 13 nm with respect to peak absorption of free ICG in cell culture medium supplemented with fetal bovine serum. These nano-encapsulation induced shifts can be attributed to the amphipathic nature of ICG that result in its interactions with the phospholipid tails, phospholipid polar heads within the inner leaflet, and membrane proteins of the erythrocyte-derived particles. Nano-encapsulation could also induce conformational changes to the IbA complex. Such interactions and structural changes can

ultimately alter the electronic states of ICG and IbA to result in the observed bathochromic shifts.

The reported values of ICG binding constant to BSA or HSA at 1:1 molar ratio are in the range of 5.5-5.7 x 10^{-5} M^{-1}, indicating a strongly bound dye to albumin. [49-51] Assuming that ICG binds to the hydrophobic pocket of albumin (site IIA), molecular docking experiments have suggested that the most favorable ICG conformation is the trans configuration.[49-50] This tight configuration likely affects the photoisomerization behavior of ICG. In response to photo-excitation, IbA cannot undergo photoisomerization to the cis conformation, a configuration where ICG exhibits aggregation, such as π-π stacking,[35] thereby stabilizing the ICG to achieve higher fluorescence quantum yield.

As the amount of ICG in the loading buffer increased, we observed the maximum value of ζ when using 20 μM ICG (Figure 2.3B). Despite an increasing trend in η with higher values of ICG concentration in the loading buffer, the decrease in ζ for NETs is likely due to the presence of the aggregated forms of ICG within NETs. In general, IbA-NETs showed higher peak values of ζ (Figure 2.3C). We observed a two to sixfold enhancement in ζ^* for IbA-NETs when compared to the values associated with NETs formed at corresponding ICG concentrations (Figure 2.3D) despite the lower loading efficiency of IbA as compared to that of ICG (Figure 2.4A). We attribute this enhancement to ICG's binding to the hydrophobic pocket of BSA.[33, 50-51] ICG likely exists in the trans-configuration when tightly bound to albumin such that it cannot interact with other molecules of ICG to form aggregates. Herein, we have demonstrated

fluorescence enhancement in NETs as a result of using an IbA complex as the NIR-activated agent. Such an enhancement may make IbA-NETs as sensitive and effective nano-probes for tumor imaging. In order to achieve maximum fluorescence emission, IbA concentration level used in fabrication of NETs needs to be optimized. Our results (Figures 2.3B-2.3C) suggest that IbA concentration of 75 μM may be an optimum concentration in fabrication of IbA-NETs to produce maximum fluorescence emission in response to 720 nm photo-excitation. Even at suboptimal concentration of 50 μM IbA where a threefold increase in fluorescence emission was observed (Figure 2.3D), we still achieved ≈ twofold enhancement in emission intensity when imaging the cells with IbA-NETs as compared with NETs (Figure 2.5B). Although fluorescence imaging of cells was not performed using 75 μM IbA, we would expect even greater emission intensity.

Since NETs were not functionalized with any molecular targeting agents, their cellular internalization can result from non-receptor mediated endocytosis,[52] which can include clathrin-mediated endocytosis[53] as well as non-clathrin mediated endocytic mechanisms through caveolae and macropinosomes.[54] Our future studies will include surface functionalization of IbA-NETs to achieve specific molecular targeting, and evaluation of their imaging capabilities in animal model systems.

2.5 Conclusion

We report the engineering and characterization of erythrocyte-derived optical nanoparticles with ICG and ICG bound albumin (IbA). Our results demonstrate that use of IbA as the NIR-activated optical agent can enhance the fluorescence emission of these

nanoparticles by approximately two to sixfold depending on the ICG concentration used to fabricate the particles. These constructs may ultimately serve as effective nano-probes tumor imaging.

2.7 References

1. Hill, T. K.; Kelkar, S. S.; Wojtynek, N. E.; Souchek, J. J.; Payne, W. M.; Stumpf, K.; Marini, F. C.; Mohs, A. M., Near Infrared Fluorescent Nanoparticles Derived from Hyaluronic Acid Improve Tumor Contrast for Image-Guided Surgery. *Theranostics* **2016,** *6* (13), 2314-2328. DOI: 10.7150/thno.16514.

2. Xi, L.; Zhou, G.; Gao, N.; Yang, L.; Gonzalo, D. A.; Hughes, S. J.; Jiang, H., Photoacoustic and Fluorescence Image-guided Surgery Using a Multifunctional Targeted Nanoprobe. *Ann. Surg. Oncol.* **2014,** *21* (5), 1602-9. DOI: 10.1245/s10434-014-3541-9.

3. Gioux, S.; Choi, H. S.; Frangioni, J. V., Image-guided Surgery Using Invisible Near-infrared Light: Fundamentals of Clinical Translation. *Mol. Imaging* **2010,** *9* (5), 237-55.

4. Tummers, Q. R. J. G.; Boogerd, L. S. F.; de Steur, W. O.; Verbeek, F. P. R.; Boonstra, M. C.; Handgraaf, H. J. M.; Frangioni, J. V.; van de Velde, C. J. H.; Hartgrink, H. H.; Vahrmeijer, A. L., Near-infrared fluorescence sentinel lymph node detection in gastric cancer: A pilot study. *World Journal of Gastroenterology* **2016,** *22* (13), 3644-3651. DOI: 10.3748/wjg.v22.i13.3644.

5. Schaafsma, B. E.; Mieog, J. S. D.; Hutteman, M.; Van der Vorst, J. R.; Kuppen, P. J. K.; Lowik, C. W. G. M.; Frangioni, J. V.; Van de Velde, C. J. H.; Vahrmeijer, A. L., The Clinical Use of Indocyanine Green as a Near-Infrared Fluorescent Contrast Agent for Image-Guided Oncologic Surgery. *J Surg Oncol* **2011,** *104* (3), 323-332. DOI: 10.1002/jso.21943.

6. Polom, K.; Murawa, D.; Rho, Y.-s.; Nowaczyk, P.; Hünerbein, M.; Murawa, P., Current trends and emerging future of indocyanine green usage in surgery and oncology. *Cancer* **2011,** *117* (21), 4812-4822. DOI: 10.1002/cncr.26087.

7. Landsman, M. L.; Kwant, G.; Mook, G. A.; Zijlstra, W. G., Light-absorbing properties, stability, and spectral stabilization of indocyanine green. *J Appl. Physiol.* **1976,** *40* (4), 575-83.

8. Shimizu, S.; Kamiike, W.; Hatanaka, N.; Yoshida, Y.; Tagawa, K.; Miyata, M.; Matsuda, H., New method for measuring ICG Rmax with a clearance meter. *World J. Surg.* **1995,** *19* (1), 113-8; discussion 118.

9. Ohnishi, S.; Lomnes, S. J.; Laurence, R. G.; Gogbashian, A.; Mariani, G.; Frangioni, J. V., Organic Alternatives to Quantum Dots for Intraoperative Near-Infrared Fluorescent Sentinel Lymph Node Mapping. *Mol. Imaging* **2005,** *4* (3), 172-181.

10. Yoneya, S.; Saito, T.; Komatsu, Y.; Koyama, I.; Takahashi, K.; Duvoll-Young, J., Binding properties of indocyanine green in human blood. *Invest Ophth Vis Sci* **1998,** *39* (7), 1286-1290.

11. Toyota, T.; Fujito, H.; Suganami, A.; Ouchi, T.; Ooishi, A.; Aoki, A.; Onoue, K.; Muraki, Y.; Madono, T.; Fujinami, M.; Tamura, Y.; Hayashi, H., Near-Infrared-Fluorescence Imaging of Lymph Nodes by Using Liposomally Formulated Indocyanine Green Derivatives. *Bioorg. Med. Chem.* **2014,** *22* (2), 721-7. DOI: 10.1016/j.bmc.2013.12.026.

12. Wu, L.; Fang, S.; Shi, S.; Deng, J.; Liu, B.; Cai, L., Hybrid polypeptide micelles loading indocyanine green for tumor imaging and photothermal effect study. *Biomacromolecules* **2013,** *14* (9), 3027-33. DOI: 10.1021/bm400839b.

13. Sharma, P.; Bengtsson, N. E.; Walter, G. A.; Sohn, H. B.; Zhou, G.; Iwakuma, N.; Zeng, H.; Grobmyer, S. R.; Scott, E. W.; Moudgil, B. M., Gadolinium-doped silica nanoparticles encapsulating indocyanine green for near infrared and magnetic resonance imaging. *Small* **2012,** *8* (18), 2856-68. DOI: 10.1002/smll.201200258.

14. Guerrero, Y.; Singh, S. P.; Mai, T.; Murali, R. K.; Tanikella, L.; Zahedi, A.; Kundra, V.; Anvari, B., Optical Characteristics and Tumor Imaging Capabilities of Near Infrared Dyes in Free and Nano-

Encapsulated Formulations Comprised of Viral Capsids. *ACS Appl. Mater. Inter.* **2017,** *9* (23), 19601-19611. DOI: 10.1021/acsami.7b03373.

15. Bahmani, B.; Guerrero, Y.; Bacon, D.; Kundra, V.; Vullev, V. I.; Anvari, B., Functionalized Polymeric Nanoparticles Loaded with Indocyanine Green as Theranostic Materials for Targeted Molecular Near Infrared Fluorescence Imaging and Photothermal Destruction of Ovarian Cancer Cells. *Laser Surg Med* **2014,** *46* (7), 582-592. DOI: 10.1002/lsm.22269.

16. Agrawal, V.; Woo, J. H.; Borthakur, G.; Kantarjian, H.; Frankel, A. E., Red blood cell-encapsulated L-asparaginase: potential therapy of patients with asparagine synthetase deficient acute myeloid leukemia. *Protein Pept. Lett.* **2013,** *20* (4), 392-402.

17. Antonelli, A.; Magnani, M., Red blood cells as carriers of iron oxide-based contrast agents for diagnostic applications. *J. Biomed. Nanotechnol.* **2014,** *10* (9), 1732-50.

18. Blanco, E.; Shen, H.; Ferrari, M., Principles of nanoparticle design for overcoming biological barriers to drug delivery. *Nat Biotechnol* **2015,** *33* (9), 941-951. DOI: 10.1038/nbt.3330.

19. Gutierrez Millan, C.; Colino Gandarillas, C. I.; Sayalero Marinero, M. L.; Lanao, J. M., Cell-based drug-delivery platforms. *Therapeutic delivery* **2012,** *3* (1), 25-41.

20. Hu, C. M.; Fang, R. H.; Zhang, L., Erythrocyte-inspired delivery systems. *Advanced Healthcare Materials* **2012,** *1* (5), 537-47. DOI: 10.1002/adhm.201200138.

21. Muzykantov, V. R., Drug delivery by red blood cells: vascular carriers designed by mother nature. *Expect Opin. Drug Deliv.* **2010,** *7* (4), 403-27. DOI: 10.1517/17425241003610633.

22. Tan, S. W.; Wu, T. T.; Zhang, D.; Zhang, Z. P., Cell or Cell Membrane-Based Drug Delivery Systems. *Theranostics* **2015,** *5* (8), 863-881. DOI: 10.7150/thno.11852.

23. Yoo, J. W.; Irvine, D. J.; Discher, D. E.; Mitragotri, S., Bio-inspired, bioengineered and biomimetic drug delivery carriers. *Nat. Rev. Drug Discov.* **2011,** *10* (7), 521-35. DOI: 10.1038/nrd3499.

24. Su, Y.; Xie, Z.; Kim, G. B.; Dong, C.; Yang, J., Design Strategies and Applications of Circulating Cell-Mediated Drug Delivery Systems. *ACS Biomaterials Science & Engineering* **2015,** *1* (4), 201-217. DOI: 10.1021/ab500179h.

25. Aryal, S.; Nguyen, T. D. T.; Pitchaimani, A.; Shrestha, T. B.; Biller, D.; Troyer, D., Membrane Fusion-Mediated Gold Nanoplating of Red Blood Cell: A Bioengineered CT-Contrast Agent. *ACS Biomaterials Science & Engineering* **2017,** *3* (1), 36-41. DOI: 10.1021/acsbiomaterials.6b00573.

26. Oldenborg, P. A.; Zheleznyak, A.; Fang, Y. F.; Lagenaur, C. F.; Gresham, H. D.; Lindberg, F. P., Role of CD47 as a marker of self on red blood cells. *Science* **2000,** *288* (5473), 2051-2054. DOI: DOI 10.1126/science.288.5473.2051.

27. Rodriguez, P. L.; Harada, T.; Christian, D. A.; Pantano, D. A.; Tsai, R. K.; Discher, D. E., Minimal "Self" Peptides That Inhibit Phagocytic Clearance and Enhance Delivery of Nanoparticles. *Science* **2013,** *339* (6122), 971-975. DOI: 10.1126/science.1229568.

28. Oldenborg, P. A., CD47: A Cell Surface Glycoprotein Which Regulates Multiple Functions of Hematopoietic Cells in Health and Disease. *ISRN Hematol.* **2013,** *2013*, 614619. DOI: 10.1155/2013/614619.

29. Hu, C.-M. J.; Zhang, L.; Aryal, S.; Cheung, C.; Fang, R. H.; Zhang, L., Erythrocyte membrane-camouflaged polymeric nanoparticles as a biomimetic delivery platform. *P Natl Acad Sci USA* **2011,** *108* (27), 10980-10985. DOI: 10.1073/pnas.1106634108.

30. Domenech, C.; Thomas, X.; Gueyffier, F.; Mazingue, F.; Auvrignon, A.; Corm, S.; Dombret, H.; Chevallier, P.; Galambrun, C.; Huguet, F.; Legrand, F.; Mechinaud, F.; Vey, N.; Philip, I.; Liens, D.; Godfrin, Y.; Rigal, D.; Bertrand, Y., L-asparaginase loaded red blood cells in refractory or relapsing acute

lymphoblastic leukaemia in children and adults: results of the GRASPALL 2005-01 randomized trial. *Br. J. Haematol.* **2010,** *153*, 58-65.

31. Bossa, F.; Latiano, A.; Rossi, L.; Magnani, M.; Palmieri, O.; Dallapiccola, B.; Serafini, S.; Damonte, G.; De Santo, E.; Andriulli, A.; Annese, V., Erythrocyte-Mediated Delivery of Dexamethasone in Patients With Mild-to-Moderate Ulcerative Colitis, Refractory to Mesalamine: A Randomized, Controlled Study. *Am. J. Gastroenterol.* **2008,** *103* (10), 2509-2516.

32. Frangioni, J. V., In vivo near-infrared fluorescence imaging. *Curr Opin Chem Biol* **2003,** *7* (5), 626-634. DOI: 10.1016/j.cbpa.2003.08.007.

33. Philip, R.; Penzkofer, A.; Bäumler, W.; Szeimies, R. M.; Abels, C., Absorption and fluorescence spectroscopic investigation of indocyanine green. *Journal of Photochemistry and Photobiology A: Chemistry* **1996,** *96* (1–3), 137-148. DOI: http://dx.doi.org/10.1016/1010-6030(95)04292-X.

34. Ohtsubo, S.; Kusano, M., Indocyanine Green Fluorescence Properties. In *ICG Fluorescence Imaging and Navigation Surgery*, Kusano, M.; Kokudo, N.; Toi, M.; Kaibori, M., Eds. Springer Japan: Tokyo, 2016; pp 9-20. DOI: 10.1007/978-4-431-55528-5_2.

35. Jung, B. S.; Vullev, V. I.; Anvari, B., Revisiting Indocyanine Green: Effects of Serum and Physiological Temperature on Absorption and Fluorescence Characteristics. *IEEE J. Sel. Top. Quant.* **2014,** *20* (2). DOI: 10.1109/Jstqe.2013.2278674.

36. Mac, J. T.; Nunez, V.; Burns, J. M.; Guerrero, Y. A.; Vullev, V. I.; Anvari, B., Erythrocyte-derived nano-probes functionalized with antibodies for targeted near infrared fluorescence imaging of cancer cells. *Biomed Opt Express* **2016,** *7* (4), 1311-1322. DOI: 10.1364/Boe.7.001311.

37. Bahmani, B.; Bacon, D.; Anvari, B., Erythrocyte-derived photo-theranostic agents: hybrid nano-vesicles containing indocyanine green for near infrared imaging and therapeutic applications. *Sci Rep-Uk* **2013,** *3*. DOI: ARTN 2180

10.1038/srep02180.

38. Burns, J. M.; Saager, R.; Majaron, B.; Jia, W. C.; Anvari, B., Optical properties of biomimetic probes engineered from erythrocytes. *Nanotechnology* **2017,** *28* (3). DOI: Artn 035101

10.1088/1361-6528/28/3/035101.

39. Jay, A. W. L., Geometry of Human Erythrocyte .1. Effect of Albumin on Cell Geometry. *Biophys J* **1975,** *15* (3), 205-222. DOI: Doi 10.1016/S0006-3495(75)85812-7.

40. Kuo, Y. C.; Wu, H. C.; Hoang, D.; Bentley, W. E.; D'Souza, W. D.; Raghavan, S. R., Colloidal Properties of Nanoerythrosomes Derived from Bovine Red Blood Cells. *Langmuir* **2016,** *32* (1), 171-179. DOI: 10.1021/acs.langmuir.5b03014.

41. Rao, L.; Meng, Q. F.; Bu, L. L.; Cai, B.; Huang, Q. Q.; Sun, Z. J.; Zhang, W. F.; Li, A.; Guo, S. S.; Liu, W.; Wang, T. H.; Zhao, X. Z., Erythrocyte Membrane-Coated Upconversion Nanoparticles with Minimal Protein Adsorption for Enhanced Tumor Imaging. *ACS Appl. Mater. Inter.* **2017,** *9* (3), 2159-2168. DOI: 10.1021/acsami.6b14450.

42. Wilhelm, S.; Tavares, A. J.; Dai, Q.; Ohta, S.; Audet, J.; Dvorak, H. F.; Chan, W. C. W., Analysis of nanoparticle delivery to tumours. *Nat Rev Mater* **2016,** *1*, 16014. DOI: 10.1038/natrevmats.2016.14

http://www.nature.com/articles/natrevmats201614#supplementary-information.

43. Fernandes, H. P.; Cesar, C. L.; Barjas-Castro, M. d. L., Electrical properties of the red blood cell membrane and immunohematological investigation. *Rev Bras Hematol Hemoter.* **2011,** *33* (4), 297-301. DOI: 10.5581/1516-8484.20110080.

44. Durocher, J. R.; Payne, R. C.; Conrad, M. E., Role of sialic acid in erythrocyte survival. *Blood* **1975,** *45* (1), 11-20.

45. Eylar, E. H.; Madoff, M. A.; Brody, O. V.; Oncley, J. L., The contribution of sialic acid to the surface charge of the erythrocyte. *J. Biol. Chem.* **1962,** *237*, 1992-2000.

46. Luk, B. T.; Jack Hu, C.-M.; Fang, R. H.; Dehaini, D.; Carpenter, C.; Gao, W.; Zhang, L., Interfacial interactions between natural RBC membranes and synthetic polymeric nanoparticles. *Nanoscale* **2014,** *6* (5), 2730-2737. DOI: 10.1039/C3NR06371B.

47. Bentley, A. A.; Adams, J. C., The Evolution of Thrombospondins and Their Ligand-Binding Activities. *Mol Biol Evol* **2010,** *27* (9), 2187-2197. DOI: 10.1093/molbev/msq107.

48. Hu, C.-M. J.; Fang, R. H.; Luk, B. T.; Chen, K. N. H.; Carpenter, C.; Gao, W.; Zhang, K.; Zhang, L., 'Marker-of-self' functionalization of nanoscale particles through a top-down cellular membrane coating approach. *Nanoscale* **2013,** *5* (7), 2664-2668. DOI: 10.1039/c3nr00015j.

49. Berezin, M. Y.; Guo, K.; Akers, W.; Livingston, J.; Solomon, M.; Lee, H.; Liang, K.; Agee, A.; Achilefu, S., Rational Approach To Select Small Peptide Molecular Probes Labeled with Fluorescent Cyanine Dyes for in Vivo Optical Imaging. *Biochemistry* **2011,** *50* (13), 2691-2700. DOI: 10.1021/bi2000966.

50. Nairat, M.; Konar, A.; Kaniecki, M.; Lozovoy, V. V.; Dantus, M., Investigating the role of human serum albumin protein pocket on the excited state dynamics of indocyanine green using shaped femtosecond laser pulses. *Physical Chemistry Chemical Physics* **2015,** *17* (8), 5872-5877. DOI: 10.1039/C4CP04984E.

51. Moody, E. D.; Viskari, P. J.; Colyer, C. L., Non-covalent labeling of human serum albumin with indocyanine green: a study by capillary electrophoresis with diode laser-induced fluorescence detection. *J. Chromatogr. B Biomed. Sci. Appl.* **1999,** *729* (1–2), 55-64. DOI: http://dx.doi.org/10.1016/S0378-4347(99)00121-8.

52. Deng, J.; Gao, C. Y., Recent advances in interactions of designed nanoparticles and cells with respect to cellular uptake, intracellular fate, degradation and cytotoxicity. *Nanotechnology* **2016,** *27* (41). DOI: 10.1088/0957-4484/27/41/412002.

53. Royle, S. J., The cellular functions of clathrin. *Cell Mol Life Sci* **2006,** *63* (16), 1823-32. DOI: 10.1007/s00018-005-5587-0.

54. Nichols, B. J.; Lippincott-Schwartz, J., Endocytosis without clathrin coats. *Trends Cell Biol* **2001,** *11* (10), 406-12.

Chapter 3. Biodistribution and toxicological evaluation of micron- and nano-sized erythrocyte-derived optical particles in healthy Swiss Webster mice

3.1 Abstract

Particle-based systems provide a capability for the delivery of imaging and/or therapeutic payloads. We have engineered constructs derived from erythrocytes, and doped with the FDA-approved near infrared dye, indocyanine green (ICG). We refer to these optical particles as NIR erythrocyte-mimicking transducers (NETs). A particular feature of NETs is that their diameters can be tuned from micron- to nano-scale. Herein, we investigated the effects of micron- (≈ 2.6 μm diameter), and nano- (≈ 145 nm diameter) sized NETs on their biodistribution, and evaluated their acute toxicity in healthy Swiss Webster mice. Following tail vein injection of free ICG and NETs, animals were euthanized at various time points up to 48 hours. Fluorescence analysis of blood showed that nearly 11% of the injected amount of nano-sized NETs (nNETs) remained in blood at 48 hours post-injection as compared to ≈ 5% for micron-sized NETs (μNETs). Similarly, at this time point, higher levels of nNETs were present in various organs including the lungs, liver, and spleen, indicating that nano-encapsulation of ICG in these constructs provided a method to prolong its circulation. Histological analyses of various organs, extracted at 24 hours post-injection of NETs, did not show pathological alterations. Serum biochemistry profiles, in general, did not show elevated levels of the various analyzed biomarkers associated with liver and kidney functions. Values of various hematological profiles

remained within the normal ranges following the administration of μNETs and nNETs. Results of this study suggest that erythrocyte-derived particles can potentially provide a non-toxic platform for delivery of ICG.

3.2 Introduction

Particle-based systems play a prominent role in the field of clinical medicine as they provide a capability to deliver imaging or therapeutic agents to specific sites within the body.[1-2] In relation to particles that deliver optical agents for imaging or phototherapeutic applications, the use of materials that are photo-activated by near infrared (NIR) excitation wavelengths (≈700–1300 nm) is especially advantageous since at this optically transparent window there is minimal light absorption by water and proteins, and diminished scattering by biological components, leading to increased depth of penetration on the order of a few centimeters.[3] Furthermore, given that there is negligible tissue autofluorescence over this spectral window, the use of exogenous fluorescent materials can enhance the image contrast.

One particular NIR exogenous dye is indocyanine green (ICG). It is a tricarbocyanine molecule with maximum spectral peak in the range of ≈ 780 – 810 nm, depending on the solvent and concentration.[4-5] To date, ICG remains as the only NIR-activated agent approved by United States Food and Drug Administration for specific applications such as ophthalmic angiography, and assessment of liver and cardiovascular functions.[6] Additionally, considerable efforts have been devoted to utilize ICG as a photothermal therapy reagent and photosensitizer for photodynamic therapy.[7-10]

Despite its effective usage in clinical medicine, the major limitations of ICG are its short half-life within plasma (2~4 minutes), with nearly exclusive uptake by hepatocytes and elimination from the body through the hepatobiliary mechanism.[11-12] Encapsulation of ICG has been used as a strategy to reduce its non-specific interactions with plasma biomolecules, and increase its circulation time.[13] Previously, we reported the encapsulation of ICG into a synthetic polymer, poly (allylamine) hydrochloride cross-linked to sodium phosphate.[14] When coated with 5 kDa poly (ethylene) glycol, these ICG-containing nanoparticles with peak diameter of ≈ 80 nm remained detectable within the circulation at 90 minutes post intravenous injection in mice.

Apart from synthetic polymers,[14-15] and liposomes [16] attention has been given to the use of mammalian cells as carriers for delivery of imaging/contrast reagents or therapeutic payloads.[16-17] We previously provided the first report on the engineering of erythrocyte-derived nano-sized vesicles loaded with ICG, and their utility for fluorescence imaging and photo-destruction of human mammalian cells.[18] We refer to these constructs as NETs (NIR erythrocyte-derived transducers) as they can convert the absorbed NIR light to emit fluorescence, generate heat, or induce photochemistry.[19]

Recently, other investigators have encapsulated ICG or other agents such as gold nanoparticle and doxorubicin into erythrocytes-derived nano-constructs.[20-24] For example, nano-constructs (≈ 80 nm diameter) composed of poly (lactic-co-glycolic acid) (PLGA) core fused with erythrocyte-derived membranes were retained in mice blood at two days post tail vein injection.[25] Piao et al have reported that gold nanocages cloaked with erythrocyte membranes (≈ 90 nm diameter) were present in mice blood 24 hours after tail

vein injection.[23] Godfrin et al have demonstrated the half-life of L-asparaginase encapsulated into erythrocytes as ~28 days for treatment of acute lymphocytic leukemia.[26] Hence, constructs derived from erythrocytes may offer a promising approach for increased circulation time within the vasculature.

A particular feature of NETs is that their diameters can be tuned from nano- to micron-scale levels based on appropriate mechanical manipulation methods.[27] The nano-sized NETs (nNETs) have relevance to optical imaging and phototherapy of tumors since particles with diameters $< \approx 200$ nm are effective for extravasation into tumors by the enhanced permeability and retention effect resulting from leaky tumor vasculature and impaired lymphatic drainage.[28-29] Micron-sized NETs (μNETs) have relevance to phototherapy of vasculature. An example of abnormal vasculature is associated with cutaneous capillary malformations such as port wine stain lesions where NETs can potentially serve as the target of laser irradiation to induce photo-destruction of the abnormal vasculature plexus.[30] To the best of our knowledge, there have not been prior studies to investigate the effects of the diameter of erythrocyte-derived constructs such as NETs on their resulting circulation kinetics. Additionally, we investigate the effects of NETs diameter on toxicology profiles of these particles in healthy mice. Results of this study provide important information not only towards identifying the window of time over which NETs-based optical imaging or phototherapy can be performed, but may also be useful for investigators interested in various optical sensing, imaging, or photo-therapeutic applications of erythrocyte-derived platforms.

3.3 Materials and Methods

3.3.1 Fabrication of μNETs and nNETs

A schematic of the NETs fabrication process is presented in Figure 3.1. Erythrocytes were separated from bovine whole blood (Rockland Immunochemicals, Inc., Limerick, PA, USA) by centrifugation process. Approximately, 1 ml of bovine whole blood was taken in an eppendorf, and centrifuged for 10 minutes (1600×*g* at 4 ºC). The supernatant

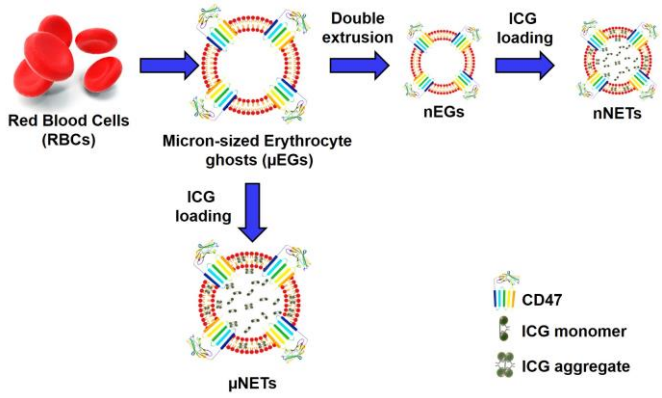

Figure 3.1: Schematic representation for fabrication of μNETs and nNETs.

containing the plasma and buffy coat were discarded, and the resulting packed erythrocytes were washed twice with 310 mOsm, phosphate buffer solution (PBS) (referred to as the 1x solution) (Fisher Scientific, Hampton, NH, USA) at pH ~ 8.0. The erythrocytes were then subjected to sequential hypotonic treatment with 0.5× (155 mOsm, pH ~ 8.0) and 0.25× (80 mOsm, pH ~ 8.0) PBS, respectively. The centrifugation process (20,000×*g*, 15 minutes, 4 ºC) was repeated until all the hemoglobin was depleted, resulting in an opaque white pellet. The obtained pellet containing micron-sized erythrocyte ghosts (μEGs) were resuspended in 1 ml of 1x PBS. To obtain nano-sized

erythrocyte ghosts (nEGs), μEGs were extruded 20 times through 400 nm polycarbonate porous membranes, followed by 20 more extrusions through 100 nm polycarbonate porous membranes using an extruder (Avanti mini extruder, Avanti Polar Lipids, Alabaster, AL, USA).

To load ICG (MP Biomedicals, Santa Ana, CA, USA) into micron/nano-sized EGs, 350 μl of μEGs or nEGs suspended in 1x PBS were incubated with 23 μl of ICG stock solution (645 μM), 350 μl of Sorenson's buffer (Na_2HPO_4/NaH_2PO_4, 140 mOsm, pH ~8.0) and 280 μl nanopure water for 5 minutes at 4 ºC in the dark. Resulting concentration of ICG in this loading buffer was 15 μM. Suspension was then centrifuged and washed twice with 1x PBS at 20,000×*g* for 20 minutes at 4 ºC, or 100,000×*g* for 60 minutes to form μNETs and nNETs, respectively. The resulting μNETs and nNETs formulations were then re-suspended in 1 ml of 1x cold PBS. We note that the use of 15 μM ICG in the loading buffer can result in production of μNETs and nNETs with near maximum values of spectrally-integrated fluorescence emission.[27]

3.3.2 Characterizations

Absorption spectra of free 15 μM ICG, μNETs and nNETs suspended in 1x PBS were obtained using a UV-visible spectrophotometer (Jasco-V670 UV-vis spectrophotometer, JASCO, Easton, MD, USA) with optical path length of 1 cm. Fluorescence emission spectra of NETs in response to 720 ± 2.5 nm excitation light, spectrally filtered from a 450 W xenon lamp, were recorded in the range of 735–900 nm using a fluorometer

(Fluorolog-3 spectrofluorometer, Horiba Jobin Yvon, Edison, NJ, USA). We normalized the fluorescence emission spectra as:

$$\zeta(\lambda)=\frac{F(\lambda)}{1-10^{-A(\lambda_{ex})}} \qquad (1)$$

where A and F are the respective wavelength (λ)-dependent absorbance and intensity of the emitted fluorescence light, and λ_{ex} is the excitation wavelength. The hydrodynamic diameters and zeta potentials of μNETs and nNETs suspended in 1x PBS were measured by dynamic light scattering (DLS) (Zetasizer Nano ZS90, Malvern Instruments Ltd, Westborough, MA, USA). We fitted lognormal functions to the DLS-based estimates of NETs' hydrodynamic diameters.

We imaged the μNETs by confocal laser scanning microscopy (CLSM). Sample solution (~ 10 μl) was added to Poly-L-lysine coated glass slide, followed by placing a coverslip on the top of the glass slide, and then imaging it with a confocal microscope (ZEISS 510, Carl Zeiss AG, Oberkochen, Germany). We imaged the nNETs by scanning electron microscopy (SEM). nNETs were fixed with 2.5% glutaraldehyde (Sigma Aldrich, St. Louis, MO, USA) overnight. Subsequently, 10 μl of the nNETs solution was added to Poly-L-lysine coated slide and dried (Critical-point-dryer, Balzers CPD0202) for 30 minutes followed by sputter coating with platinum for 20 s, and then imaging with SEM (FEI NNS450).

3.3.3 Assessment of ICG leakage from μNETs and nNETs under physiological temperature

Approximately, 2 ml of μNETs and nNETs suspensions were transferred into various eppendorf tubes, and incubated at 37 °C in the dark. After specific incubation times (0, 2, 4, 6, 24 and 48 hours), the NETs suspensions were centrifuged, and the pellet was then resuspended in 1 ml of fresh 1x PBS. Subsequently, the absorption spectra of re-suspended pellet and supernatant were recorded and compared to those for day 0 to assess the ICG leakage from μNETs or nNETs. The percentage of ICG leakage (υ) in μNETs and nNETs as a function of time were calculated as:

$$\upsilon(\%) = \frac{A_{\text{supematant}}}{(A_{\text{pellet}} + A_{\text{supernatant}})} * 100 \qquad (2)$$

where A_{pellet} and $A_{\text{supernatant}}$ are the absorbance values of the pellet and supernatant recorded at 804 nm for each specific time point. Results of these experiments are presented as Electronic Supplementary Information (Figure 3.S1).

3.3.4 Biodistribution experimental design

Female Swiss Webster mice (≈ 20–25 g; ≈ 8–10 weeks old) were procured from Taconic Biosciences (Rensselaer, NY, USA) and utilized in this study under a protocol approved by the University of California, Riverside Institutional Animal Care and Use Committee. Animals were anesthetized by inhalation of 2% isoflurane in oxygen. Free ICG, μNETs or nNETs were administered intravenously via tail-vein injection while the animal was anesthetized. The injection volume for all samples was ≈ 100 μl. Injected dosages of ICG in our experiments were estimated as ≈ 58, 26.16, 14.5 μg/kg weight of the mouse for

free ICG, μNETs, and nNETs respectively. For example, the injection dosage of free ICG used was estimated as follows: based on the molecular weight of ICG (775 Da), injection concentration of 15 μM free ICG corresponds to ≈ 11.6 μg/ml. Given the injection volume of ≈ 0.1 ml into each mouse, and an average mouse weight of ≈ 20 g, dosage of free ICG administered into an animal was ≈ 0.058 μg/g (11.6 μg/ml × 0.1 ml)/20 g, or ≈ 58 μg/kg. Taking into account the respective loading efficiency of 15 μM ICG into μNETs and nNETs as ≈ 45% and 25%,[27] the administered dosage of ICG in μNETs and nNETs formulations were estimated as ≈ 26.16 μg/kg and 14.5 μg/kg, respectively. These injected dosages of ICG were much lower than the lethal dosage in 50% of animals (LD_{50}) of ~ 62 mg/kg in mice.[31] We also note that loading efficiency of ICG is not the only metric that constitutes the ideal preparation of NETs. Other important metrics are the relative fluorescence quantum yield of NETs and their total fluorescence emission over a spectral band of interest. As we have reported previously, concentration of ICG in the loading buffer, ICG loading efficiency, and NETs' fluorescence quantum yield and total emission are inter-related parameters.[27] Increased levels of the indicated optical metrics can be associated with lower values of ICG loading efficiency.[27]

Mice were euthanized with compressed CO_2 gas at various times (5 minutes, 45 minutes, 2, 6, 24, and 48 hours) following injection with free ICG, μNETs or nNETs. Three mice were used for 5 minutes, 45 minutes and 2 hours time points, whereas, five mice were used for 6, 24 and 48 hours time points for each of the imaging agents, giving a total of 72 animals for the biodistribution studies.

3.3.5 Fluorescence imaging and analysis of extracted organs

Following euthanasia, liver, spleen, kidney (single), stomach, intestine, heart and lungs (two) were extracted and imaged fluorescently in a luminescence dark box. Two light emitting diodes (LEDs) delivering excitation light in the range of 700 ± 30 nm were used for illumination. Fluorescence emission from the organs was captured using a charge-coupled device (CCD) camera (Pixis 1024B, Roper Scientific, Trenton, NJ, USA) equipped with a long pass filter transmitting wavelengths greater than 810 nm. Camera exposure time was set to 90 s. Acquired fluorescent images were analyzed using ImageJ software. Regions of interests (ROIs) were selected for each organ. The mean intensity ($\bar{I}$) values per gram of each organ acquired from a given ROI at different post-injection times were calculated as:

$$\bar{I} = \frac{\sum_{k=1}^{n}\left(\frac{1}{m_k}\right)\sum_{j=1}^{p}\frac{I_j}{p}}{n} \qquad (3)$$

where p is the total number of pixels in the ROI, m is the mass of a given organ, n is the numbers of a given organ, and I_j is the pixel intensity at the j^{th} pixel of a given image.

3.3.6 Biodistribution analysis

Extracted organs were grinded using Omni Tissue Homogenizer (Omni International, Inc., Kennesaw, GA, USA), and then incubated in 4 ml of sodium dodecyl sulfate (SDS) (Sigma Aldrich, St. Louis, MO, USA) solution (5% w/v in water) for one hour to lyse the cells causing the release of ICG. We also collected 300 µl of blood from the heart by cardiac puncture. The blood sample was mixed with 1 ml of SDS solution and incubated

for 30 minutes. This approach would ensure that any ICG or NETs uptaken by blood cells would also be released. Lysed organs and blood samples were centrifuged in the SDS solution at 16,000×g for one hour at 10 ^{o}C. Then the supernatants of the blood samples and homogenized organs were collected, and the corresponding fluorescence emission spectra in response to 720 ± 2.5 nm excitation wavelength were recorded using the fluorometer. ICG concentration in each organ was estimated by comparing the integrated fluorescence emission signal over the 735–900 nm spectral band with a calibration curve that related the integrated fluorescence emission over the same wavelength range to various concentrations of ICG in SDS solution. Specifically, we present the percentage of ICG recovered from each organ with respect to the initial dose (ID) injected per gram of organ (%ID/g).

For blood samples, the calibration curve related the spectrally-integrated fluorescence emission over the same wavelength range to various concentrations of ICG and blood in SDS solution. The integrated fluorescence emission value of whole blood in SDS solution without free ICG or NETs was subtracted from the integrated fluorescence emission values obtained for blood samples containing free ICG or NETs. The fluorescence profiles of ICG extracted from SDS-treated organs closely resembled that of free ICG dissolved in SDS (data not shown). This result validated that the fluorescence of ICG extracted from the various organs was not degraded in the presence of 5% SDS, and that autofluorescence was not a contributor to fluorescence emission at 720 ± 2.5 nm excitation wavelength.

3.3.7 Hematological, enzymatic, and histological evaluations

We injected ≈100 µl of µNETs or nNETs solutions via the tail-vein into anesthetized mice. At 24 hours post-injection, mice were euthanized, and blood samples were collected for serum biochemistry and enzymatic evaluations. This included three assays of hepatic function (Alanine Aminotransferase (ALT), Aspartate Aminotransferase (AST) and Alkaline Phosphatase (ALP)), and two renal assays (Urea nitrogen and creatinine) performed by a blood biochemical autoanalyzer (Roche Integra 400 Plus, Roche, Basel, Switzerland). A complete blood count (CBC) was also performed, which included white blood cells (WBCs) count, red blood cells (RBCs) count, mean corpuscular volume (MCV), hemoglobin, hematocrit, and platelets performed by a blood count analyzer (Drew HemaVet 950 FS, Drew Scientific, Miami Lakes, FL, USA).

A complete necropsy was performed and major organs including heart, liver, spleen, lungs and kidneys were collected. Tissues were fixed in 10% neutral buffered formalin (Fisher Scientific, Waltham, MA, USA), processed routinely into paraffin blocks and sectioned at 4 µm. These sections were stained with hematoxylin and eosin (H&E), and examined histologically for toxicity changes including thrombosis, inflammation, and necrosis. Ten mice were used for each agent for CBC and serum biochemistry, giving a total of 30 animals. Out of these, five mice were used for each agent for histological evaluations.

3.3.8 Statistical analysis

Statistical analyses were conducted using the Graphpad Instat 3.0 software by the one-way ANOVA analysis. We defined statistically significant differences at $*p < 0.05$.

3.4 Results and Discussion

3.4.1 Characterizations

Based on the analysis of CLSM images (Figure 3.2A), average diameter of µNETs was ~ 3 µm. The SEM image of nNETs demonstrated the nano-sized dimensions of these NETs

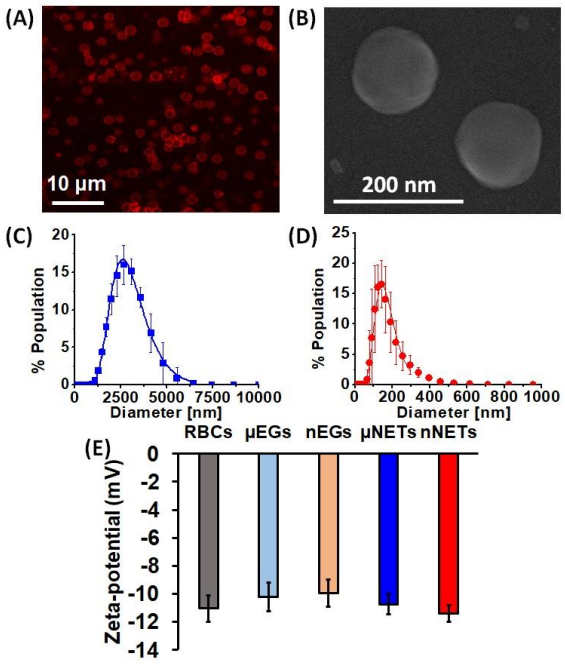

Figure 3.2: (A) Confocal laser scanning microscopy image of µNETs. A 633 nm laser was used for photo-excitation and a long-pass filter transmitting $\lambda > 650$ nm was used to collect the emitted NIR fluorescent light, falsely-colored in red. (B) Scanning electron microscopy (SEM) image for nNETs. Panels (C) and (D) represent the dynamic light scattering-based measurements of diameter distributions for µNETs and nNETs in 1x PBS, respectively. We present the mean of each measurement with errors bars representing standard deviations from the mean values. We fitted Lognormal functions to the measured diameter distributions. (E) Zeta-potentials for RBCs, µEGs, nEGs, µNETs and nNETs recorded in 1x PBS. Error bars represent the standard deviation for the three independent measurements.

(Figure 3.2B). The estimated mean peak values of hydrodynamic diameters for μNETs and nNETs, as estimated by the DLS method were 2.6 μm and 145 nm, respectively (Figures 3.2C – 3.2D).

The mean ± standard deviation (SD) zeta-potential values for red blood cells (RBCs), μEGs, nEGs, μNETs and nNETs formulations in 1x PBS (pH ~ 7.4) were -11.03 ± 1.91 mV, -10.2 ± 1.93 mV, -9.96 ± 1.74 mV, -10.7 ± 1.42 mV and -11.4 ± 1.13 mV, respectively (Figure 3.2E). Statistical analysis showed that the mean values of these zeta-potentials were not significantly different from each other. The similar zeta-potential values of μEGs, nEGs, μNETs and nNETs suggest that the sulfonate portions of ICG molecules, which carry the negative charge of ICG, were not exposed to the extracellular environment, but rather localized within the membrane or within the interior core of NETs. The overall negative charge of erythrocyte-derived constructs can be attributed to the presence of the carboxylic groups of the sialic acid on erythrocytes membranes,[32-34] suggesting that these groups were preserved on both EGs and NETs.

The peak of the absorption spectrum for 15 μM free ICG dissolved in nanopure water was at 780 nm, and is associated with the monomeric form of ICG (Figure 3.3A).[4] The absorption peak at 280 nm for μNETs and nNETs corresponds to the membrane proteins present on the surface of the NETs. The absorption spectra of μNETs and nNETs showed bathochromic (red) shifts in the monomeric peak of ICG from 780 nm to 804 nm, compared to free ICG.

We attribute this shift to encapsulation-induced changes in ICG including the formation of membrane protein-bound and phospholipid-bound forms with altered

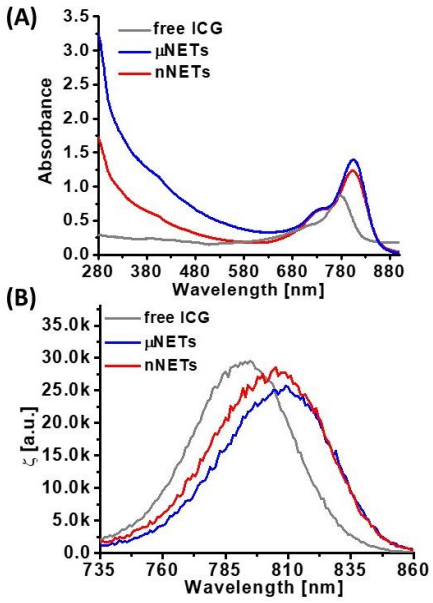

Figure 3.3: Representative (A) Absorption and (B) normalized fluorescence emission spectra of 15 μM free ICG, μNETs, and nNETs. Both μNETs and nNETs were fabricated using 15 μM ICG in the loading buffer. Spectra for μNETs and nNETs were recorded in 1x PBS, and in nanopure water for free ICG. Prior to absorption and fluorescence spectral recordings, ICG and NETs solution were diluted by 50 and 10 times, respectively. Emission spectra were obtained in response to photo-excitation at 720 ± 2.5 nm.

electronic states as compared to free form of ICG.[18, 27] Normalized fluorescence emission spectra of 15 μM free ICG, μNETs and nNETs in response to 720 nm excitation wavelength are presented in Figure 3.3B. The respective spectral peak emission values for free ICG, μNETs and nNETs were at 793 nm, 809 nm, and 806 nm, corresponding to the monomeric forms of ICG.[4, 18]

Absorption spectra of μNETs and nNETs and supernatant after centrifugation at physiological temperature in dark over a period of 48 hours are shown in Figures 3.S1A and 3.S1B. Using equation (2), we estimate the percentage leakage of ICG from μNETs and nNETs as ≈ 9.1% and 5.6%, respectively, at physiological temperature over time period of 48 hours (Figure 3.S1C).

3.4.2 Quantitative fluorescence imaging of extracted organs

Fluorescence emission from extracted liver was relatively weak at 6 hours post-injection of free ICG (Figure 3.4A). This result suggests that by this time most of ICG was eliminated from the liver, its primary accumulation site. The weak fluorescence emission from the stomach could be due to the presence of chlorophyll (alfalfa) in the rodent diet,[35] or from the ICG eliminated from the liver and excreted into the intestine via bile.[36] At 24 and 48 hours post-injection, negligible fluorescence emission from the liver and intestines, and none from the remaining harvested organs were detected, suggesting that free ICG was eliminated from the body.

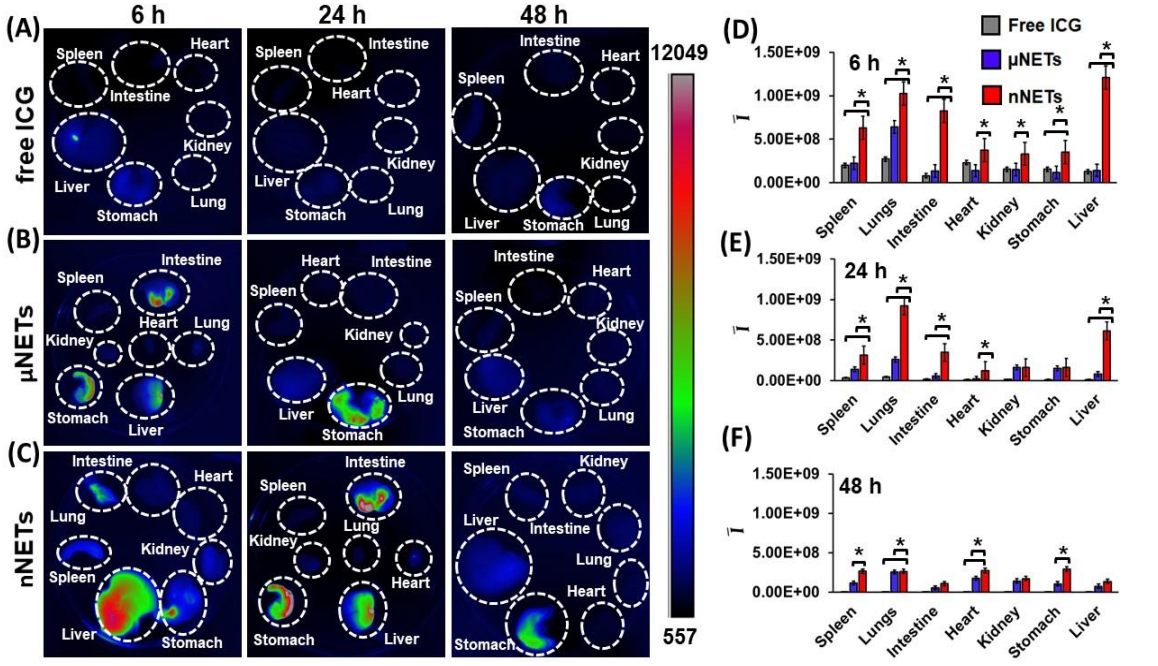

Figure 3.4: Fluorescence images of organs extracted from healthy mice at 6, 24 and 48 hours post tail-vein injection with (a) indocyanine green (ICG) (15 μM), (b) μNETs, and (c) nNETs. Scale bar on the right (in arbitrary units) corresponds to fluorescence emission intensity. (d-f) Mean ROI fluorescence intensities per gram of extracted organ (see equation 3) from healthy mice at (d) 6, (e) 24, and (f) 48 hours post tail-vein injection of ICG (15 μM), μNETs and nNETs. Error bars represent standard deviation and the single asterisks denote statistically significant differences ($p < 0.05$) between the indicated pairs.

μNETs and nNETs showed higher fluorescence signals from the extracted liver, intestine, and stomach at 6 hours post-injection (Figures 3.4B-3.4C), suggesting a lower clearance rate of these particles from systemic circulation. Fluorescence emissions associated with μNETs and nNETs were detectable in liver up to 48 hours post-injection, suggesting that NETs had prolonged the availability of ICG within the body.

The mean fluorescence intensity ($\bar{I}$) values per gram of each extracted organ for free ICG, μNETs, and nNETs at 6, 24, and 48 hours post-injection time points are shown in Figs. 3.4D-F. When compared to free ICG and μNETs, nNETs showed statistically significant ($p < 0.05$) higher values of $\bar{I}$ in all extracted organs at 6 hours post-injection (Figure 3.4D), indicating the higher accumulation of nNETs in these organs. At 24 hours post-injection, value of $\bar{I}$ associated with nNETs was significantly higher in spleen, lungs, intestine, heart and liver as compared to free ICG and μNETs (Figure 3.4E).

At 48 hours post-injection, value of $\bar{I}$ associated with nNETs remained significantly higher in spleen, lungs, heart, and stomach than those for free ICG and μNETs (Figure 3.4F). In contrast, there were no statistically significant differences between free ICG and μNETs at 48 hours in all organ samples.

3.4.3 Quantification of ICG content in blood

Fluorescence emission spectra of blood collected from healthy mice at 6 and 48 hours post-injection with μNETs and nNETs are presented in Figure 3.5A. Fluorescence emission intensity of μNETs at 6 hours post-injection was higher than that at 48 hours post-injection over the spectral band 735–900nm, indicating that the fraction of these

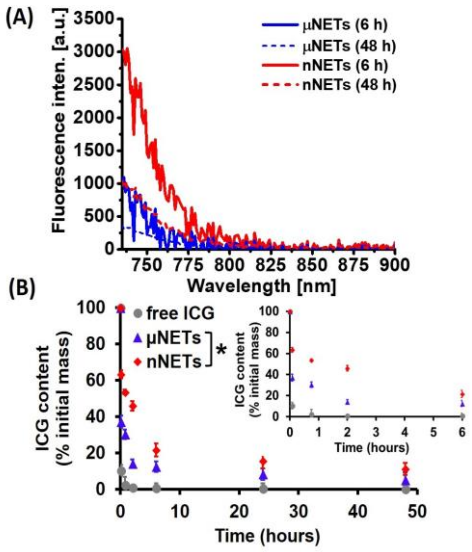

Figure 3.5: (A) Fluorescence emission spectra of blood collected from healthy mice at 6 and 48 hours post tail-vein injection with μNETs and nNETs (λ_{ex} = 720 ± 2.5 nm) after baseline subtraction of blood emission spectra in SDS. (B) Estimated percentages of ICG recovered from mice blood after tail vein injection of ICG (circles ●), μNETs (triangles ▲) and nNETs (diamonds ◆) as a function of time. The inset represents the estimated percentages of ICG recovered from mice blood for the three agents at 0 min, 5 min, 45 min, 2 and 6 hours respectively. Error bars represent standard deviations, and the single asterisk denotes statistically significant differences ($p < 0.05$) between the indicated pairs for all the time points.

particles in the bloodstream was reduced between 6–48 hours. Nano-encapsulation improved the longevity of ICG in bloodstream as compared to micro-encapsulation as evidenced by higher fluorescence emission intensity of nNETs at 48 hours post-injection when compared to that of μNETs at 48 hours post-injection (Figure 3.5A). Fluorescence emission spectrum of nNETs at 48 hours post-injection was comparable to that of μNETs at 6 hours post-injection.

We estimated the relative ICG content of blood at 5 min, 45 min, 2, 6, 24 and 48 h post-injection of free ICG, μNETs and nNETs formulations (Figure 3.5B). nNETs showed higher levels of retention in blood than μNETs. Specifically, the relative ICG content of blood at 6 hours post-injection for nNETs was ≈ 21.6% as compared ≈ 12.5% for μNETs. At 48 hours post-injection, the relative amounts of ICG for nNETs and μNETs were ≈ 11.3% and 5.3%, respectively. The lower circulation time of μNETs as

compared to nNETs can result from the increased uptake of μNETs in circulation by the mononuclear phagocytic system (MPS) that include the spleen and liver macrophages.

3.4.4 Biodistribution profiles

We quantified the relative amounts of free ICG, μNETs and nNETs in various organs at 6, 24 and 48 hours post-injections after homogenizing the organs (Figure 3.6). In all organs, there were significantly greater levels of nNETs than μNETs and free ICG at 48 hours post-injection ($p < 0.05$). For example, at 48 hours post-injection, ≈ 18.8%, 12.8%, and 8% ID/g of nNETs, μNETs, and free ICG were present in the heart, respectively (Figure 3.6A).

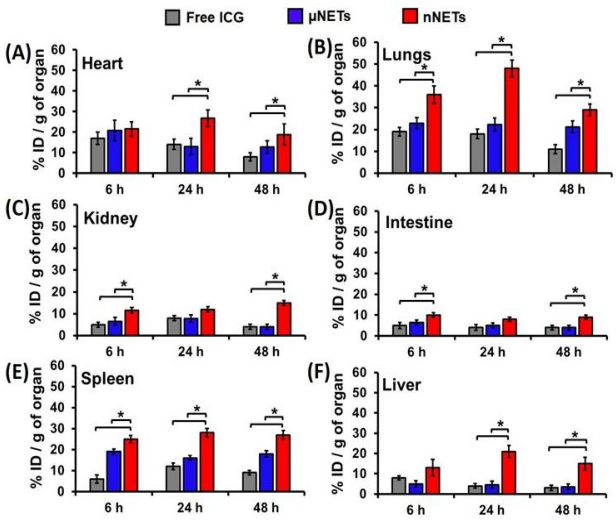

Figure 3.6: Estimated percentage of ICG recovered from organs of mice with respect to the initial dose injected per gram of organ at 6, 24 and 48 hours post tail-vein injection with indocyanine green (ICG) (15 μM), μNETs and nNETs for (a) heart, (b) lungs, (c) kidney, (d) intestine, (e) spleen, and (f) liver. Error bars represent standard deviations, and the single asterisks denote statistically significant differences ($p < 0.05$) between the indicated pairs.

Lungs were another organ site for significantly higher accumulation of nNETs (Figure 3.6B). The higher accumulation level of the nNETs in the lungs can be attributed due to their effective entrapment in the pulmonary capillaries. It is believed that endocytosis process by endothelial cells of the lungs capillaries is more effective in

internalization of nano-sized particles as compared with micron-sized particles.[13, 37] At 48 hours post-injection time point, as compared to μNETs and free ICG, statistically significantly higher levels of nNETs were also detected in kidney (≈ 15% ID/g) and intestine (9% ID/g) (Figures 3.6C-3.6D).

At 48 hours post-injection, there were ≈ 27% and 15% ID/g of nNETs in spleen and liver, respectively. In contrast, at this time point, there were only about ≈ 18% and 3.6% ID/g of μNETs, and ≈ 9% and 3% ID/g of free ICG in spleen and liver, respectively (Figures 3.6E-3.6F). A higher level of nNETs in spleen at 48 hours post-injection suggests that nNETs were still within the circulation and passing through the spleen.

In addition to filtering foreign body materials, spleen is also involved in removal of and damaged or aged erythrocytes from the blood.[38] In the open blood circulation system of spleen, the arterial blood arrives into cords in the red pulp, which contain the splenic macrophages. Blood from the cords enters the venous sinuses of the red pulp through interendothelial slits with an average width of ≈ 650 nm.[39-40] Due to their smaller diameters, nNETs (~ 145 nm mean peak diameter) can pass through these slits, and gain re-entry into the circulatory system. Some fraction of nNETs may also be uptaken by splenic macrophages of the red pulp located in the cords.

The circulation time of red blood cells (RBCs) depends on various biochemical and physical characteristics. For example, the presence of key membrane glycoproteins such as CD47, decay-accelerating factor (DAF), CD59, and CR1 on the RBC surface can impede phagocytosis and prolong the circulation time of RBCs.[41-44] Our previous results indicate that CD47 remains on the surface of μEGs and nNETs, suggesting that CD47

can survive the mechanical extrusion of μEGs,[45] and contribute to the extended circulation time of NETs by keeping them shielded from phagocytosis.

In addition to the presence of appropriate biochemical markers, healthy RBCs also have appropriate mechanical properties that allow them to deform and pass through the splenic slits. In contrast, senescent RBCs have reduced deformability.[46-47] For example, nearly 35% increase in membrane surface viscosity is reported for aged RBCs as compared to young cells.[48] A reduction in deformability of senescent RBCs impairs their capability to pass through interendothelial slits. Aged RBCs are eventually phagocytosed by the red pulp macrophages,[39] and eliminated from circulation. Similarly, μNETs (~ 2.6 μm mean peak diameter) may have reduced deformability to allow them to squeeze through splenic slits. This reduced deformability may be partially due to loss of hemoglobin during the fabrication process of NETs. Nash and Meiselman have reported that fresh micron-sized EGs with average reduction of approximately 125 times in cellular hemoglobin content had nearly 68% increase in average elastic shear modulus as compared to young intact RBCs.[48] With compromised mechanical integrity, specifically due to lowered deformability, μNETs are likely to remain within the cords and ultimately phagocytosed by the splenic macrophages. Combined with slowed blood flow rate in spleen,[40] resident red pulp macrophages can efficiently recognize μNETs and remove them from circulation. Changes in the deformability of NETs, as compared to RBCs, can also arise from alterations in membrane integral proteins such as the sialic acid-rich glycophorin A and B and 3 to affect their interactions with the membrane lipids and

major cytoskeletal proteins, spectrin, actin and ankyrin, as well as alterations in cytoskeletal cross-linking itself.[49-50]

Liver is another site for the elimination of foreign agents. Blood from both hepatic artery and portal vein are mixed together in the hepatic sinusoids before draining out of the liver to the heart through the central vein. Endothelial cells in liver sinusoids form a fenestrated lining containing pores with diameter of ≈ 170 nm,[51] which allow for passage of blood plasma to interact with hepatocytes.[52] A fraction of nNETs with diameters less than the pores' diameter are likely to leave the sinusoids and extravasate into the space of Disse where they can go undergo endocytosis by hepatocytes, and subsequently, secreted into the bile ducts, passaged into duodenum, and finally eliminated from the body. This mechanism of nNETs elimination is consistent with the hepatobiliary clearance of nanoparticles with diameters in the range of 150-200 nm,[52] and resembles hepatocytes-mediated elimination of liposomes and lipid-coated PLGA nanoparticles with similar characteristics consisting of mean diameters in the range of ≈ 150-195 nm and average zeta potentials between ≈ -19 to -10.6 mV.[53-55] Nanoerythrosomes with diameters <100 nm have also been reported to accumulate in hepatic parenchymal cells.[56]

In addition to hepatocytes, hepatic stellate cells located in the space of Disse between parenchymal and sinusoidal endothelial cells, can also uptake the nNETs extravasated out of the sinusoids. This mechanism of nanoparticles elimination has been reported for liposomes with average diameter of 92 nm and zeta potential of ≈ -20 mV.[57] The fraction of nNETs with diameters greater than the diameter of sinusoid pores, and μNETs can be uptaken by the Kupffer cells, macrophages adherent to the endothelial

lining of the liver sinusoids.[52] This phagocytic uptake is consistent with the reported accumulation of nanoerythrosomes in Kupffer cells.[56]

A particular hydrodynamic phenomenon resulting from the high (≈ 50%) occupancy of blood volume by RBCs is the margination of particles to the vessels wall.[42] Under this phenomenon, RBCs avoid the micron-scale marginal layer of the blood that directly contacts the vessel wall and allow for other circulating particles to come in contact with the wall.[58-59] It has been reported that 2 μm diameter hydrogel particles had enhanced margination when compared to their 500 nm diameters counterparts.[60] In relation to NETs, the margination phenomenon implies that μNETs may be in closer approximately to Kupffer and endothelial cells that line the sinusoids, resulting in greater uptake of these particles as compared to nNETs. Ultimately, degradation of μNETs by the splenic and hepatic MPS can result in their reduced circulation time

3.4.5 Pathology, serum biochemistry and hematology

H&E stained sections of heart, liver, spleen, lung and kidney after 24 hours post intravenous injection of μNETs and nNETs were similar to PBS-injected (control) mice (Figure 3.7A), indicating that NETs did not induce pathological alterations in these organs. The levels of blood biomarker enzymes (ALP, ALT, and AST) associated with the liver, and urea nitrogen and creatinine, associated with kidney functions are presented in Figures 3.7B-3.7C, respectively. Given that less than 20% of the injected dosages of NETs per gram of liver were detected at 48 hours (Figure 3.6F), there may not be concerns with chronic toxicity to liver parenchyma that may otherwise arise as a result of prolonged retention of particles in liver. In contrast, nearly 53% of the injected dose of 20

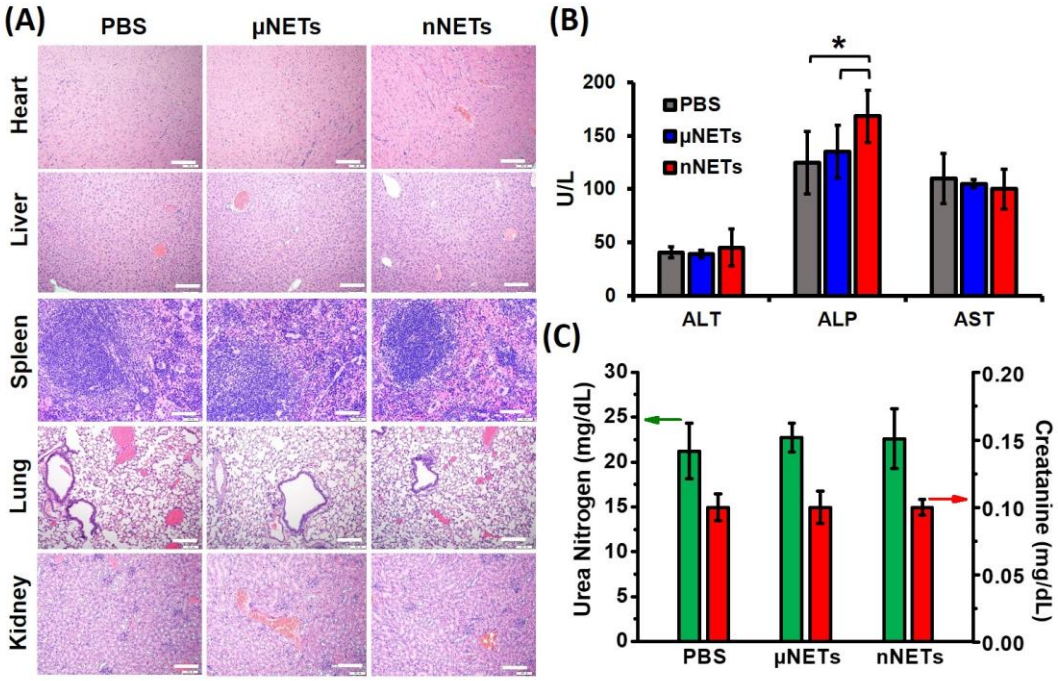

Figure 3.7: (A) Representative H&E stained images of major organs collected from healthy mice at 24 hours post tail-vein injection with PBS, μNETs, and nNETs derived from bovine blood. Scale bars indicate 100 μm. (B) Levels of Alanine Aminotransferase (ALT), Aspartate Aminotransferase (AST) and Alkaline Phosphatase (ALP), associated with hepatic function. (C) Levels of Urea nitrogen and creatinine associated with renal function. Error bars represent standard deviations and the single asterisks denote statistically significant differences ($p < 0.05$) between the indicated pairs.

nm diameter zinc oxide,[61] and 80% of 30 nm diameter superparamagnetic iron oxide nanoparticles[62] were retained in liver for at least 21 and 84 days, respectively.

ALT and AST levels for μNETs and nNETs were similar to those for PBS-injected (control) mice (Figure 3.7B). However, ALP levels were higher ($p < 0.05$) for nNETs when compared to those for PBS and μNETs. Levels of urea nitrogen and creatinine did not statistically differ as a function of the administered agent (Figure 3.7C).

While the values for various hematological parameters can vary with the mouse strain, age, sex, and other factors, our measurements are within the normal ranges reported for these parameters,[63-64] regardless of the administered agent (Table 1). Values

Parameter	Normal Range	Free ICG	PBS	µNETs	nNETs
WBCs (K/µL)	3.0 – 14.2[63]	5.0 ±2.3[65]	10.2 ± 1.4	6.0 ± 1.3	9 ± 1.6
			*	*	
RBCs (K/µL)	5.0 – 9.5[63]	6.1 ±1.1[65]	8.9 ± 0.6	9.1 ± 1.0	9.0 ± 0.3
MCV (fL)	48.0 – 56.0[63]	57.2 ± 1.9[65]	48.6 ± 5.1	48.6 ± 3.9	50.4 ± 5.4
Hemoglobin (g/dL)	10.9 – 16.3[63]	12.8 ± 2.2[65]	14 ± 0.7	12.8 ± 1.2	13.4 ± 0.6
Hematocrit (%)	41.5 – 48.2[64]	34.9 ±6.3[65]	43 ± 3.5	42.4 ± 5.0	43.5 ±3.1
Platelets (K/µL)	930 -1626[64]	721.2 ± 462.7[65]	1167 ± 155	1005 ± 145	1148 ± 193
			*	*	

Table 3.1: Hematology profiles of mice at 24 hours post tail vein injection of PBS (control), µNETs, and nNETs derived from bovine blood. Each experiment was repeated five times. Values represent the mean ± standard deviations. WBCs: white blood cells; RBCs: red blood cells; MCV: mean corpuscular volume. K denotes 1000. Single asterisks denote statistically significant differences of $p < 0.05$ between the indicated pairs. Reported ranges from reference 63 are based on values from various mouse strains, sex, and age. Reported ranges from reference 64 are for 16 weeks female Swiss Webster mice from Charles River Laboratories, Inc. Reported values from reference 65 are in response to 20 mg/kg of free ICG injection into Sprague-Dawley rats.

of RBCs, MCV, hemoglobin and % hematocrit did not statistically differ as a function of the administered agent (Table 1). Despite our results that the levels of WBCs and platelets were significantly lower ($p < 0.05$) in response to administration of µNETs, as compared to those following the administration of PBS and nNETs, they were still within the normal ranges. Similarly, Marshall et al. have also reported a reduction in WBCs and platelets counts, but still within the normal range, upon injection of 20 mg/kg of free ICG into Sprague-Dawley rats (Table 1), [65] a dosage substantially higher than our estimated dosages of 58 µg/kg for free ICG, and 26.16 and 14.5 µg/kg of ICG in µNETs and nNETs formulations, respectively.

Activation of Kupffer cells through interaction with NETs in the liver can induce the secretion of various cytokines for recruitment of circulating neutrophils to engulf NETs and become activated apoptotic cells. Kupffer cells then recognize and phagocytose apoptotic neutrophils expressing phosphatidylserine through P-selectin-medicated hepatic sequestration.[66] These endocytosed apoptotic cells are then degraded

through phagosome maturation.[67-68] This process results in elimination of neutrophils from circulation, corresponding to a decrease in WBCs count. Based on our results, this mechanism for elimination of neutrophils, which includes activation of Kupffer cells and interaction of neutrophils with NETs, appears to be more sensitive to μNETs as compared to nNETs.

Platelets interact with leukocytes in liver and spleen.[69] They bind to the hepatic sinusoidal endothelium in an integrin-dependent manner, leading to platelet and endothelial activation and leukocyte recruitment.[70] Activated platelets overexpress p-selectin glycoprotein ligand-1 (PSGL-1) can bind to leukocytes, neutrophils and monocytes resulting in platelet aggregation followed by the release of pro-inflammatory cytokines leading to clearance by the macrophages present in the complement system.[69, 71-72] Our findings appear to suggest that the mechanisms leading to platelets activation, aggregation, and their ultimate clearance may have been more prone to μNETs as compared to nNETs. It is also possible that platelets aggregation and clumping, which may have been more prevalent in response to presence of μNETs, could have led to a decrease in the automated platelets count, as suggested in literature.[73] Finally, our findings are consistent with another study where noticeable signs of toxicity as determined by blood biochemical, hematological and histological assays were not observed in mice at 15 days post tail-vein injection of upconversion nanoparticles coated with RBC membranes.[22]

3.5 Conclusions

We have engineered erythrocyte-derived optical particles doped with ICG. The diameter of these constructs, referred to as NETs, can be adjusted from micron to nano scale. Nano-sized NETs were retained at higher levels in blood and various organs at 48 hours post tail vein injection as compared to free ICG and micron-sized NETs. Histological analyses of various organs, extracted at 24 hours post intravenous injection of NETs, did not show any pathological alterations. Serum biochemistry, in general, did not show elevated levels of the various analyzed biomarkers associated with liver and kidney functions. Values of various hematological profiles remained within the normal ranges following the administration of μNETs and nNETs. Results of this study suggest that erythrocyte-derived particles can potentially provide a non-toxic platform for delivery of payloads, and when constructed at nano-size scale, can extend the circulation time of their cargo. As optical platforms, NETs offer a great potential for clinical translation for light-based theranostic applications.

3.6 Appendix A. Electronic Supplementary Information

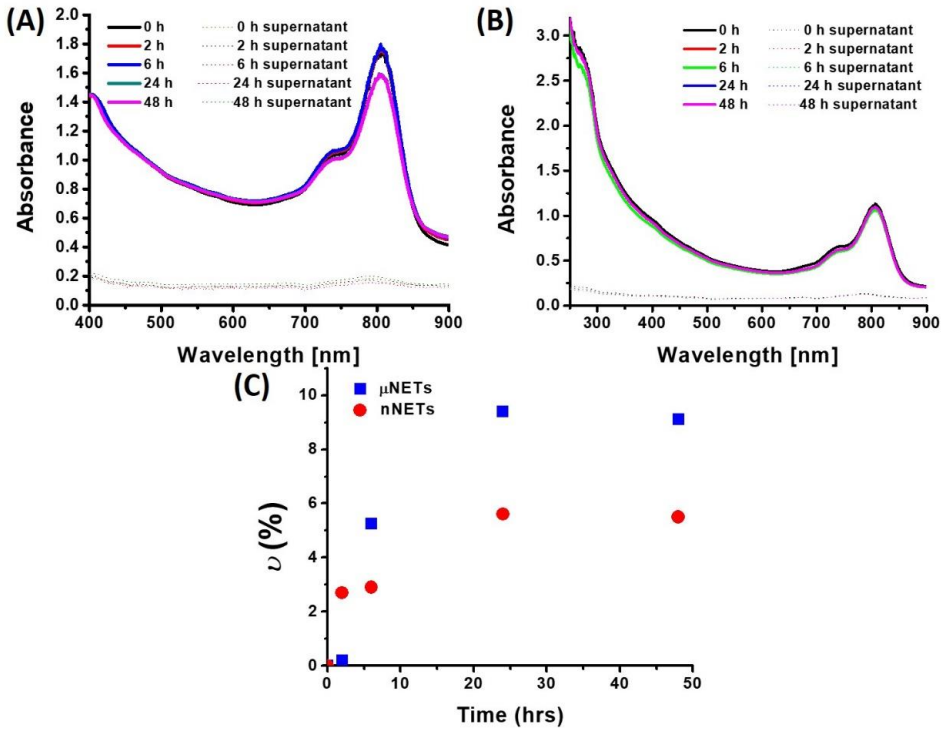

Figure 3.S1: Time-dependent absorption spectra of (A) μNETs, and (B) nNETs and the corresponding supernatant solutions at 37 °C. (C) % ICG leakage (υ) from μNETs and nNETs as a function of time.

Absorption spectra of μNETs and nNETs and their supernatants after centrifugation at physiological temperature in dark over a period of 48 hours are shown in Figure 3.S1A and 3.S1B, respectively. Using equation 2 (see manuscript text), the percentage leakage of ICG from μNETs and nNETs were calculated as ≈ 9.1% and 5.6%, respectively, at 48 hours post fabrication (Fig. 3.S1C).

3.7 References

1. Kelkar, S. S.; Reineke, T. M., Theranostics: Combining Imaging and Therapy. *Bioconjugate Chem* **2011,** *22* (10), 1879-1903. DOI: 10.1021/bc200151q.

2. Lim, E. K.; Kim, T.; Paik, S.; Haam, S.; Huh, Y. M.; Lee, K., Nanomaterials for Theranostics: Recent Advances and Future Challenges. *Chem. Rev.* **2015,** *115* (1), 327-394. DOI: DOI 10.1021/cr300213b.

3. Smith, A. M.; Mancini, M. C.; Nie, S. M., Bioimaging second window for in vivo imaging. *Nat. Nanotechnol.* **2009,** *4* (11), 710-711. DOI: 10.1038/nnano.2009.326.

4. Philip, R.; Penzkofer, A.; Bäumler, W.; Szeimies, R. M.; Abels, C., Absorption and fluorescence spectroscopic investigation of indocyanine green. *Journal of Photochemistry and Photobiology A: Chemistry* **1996,** *96* (1–3), 137-148. DOI: http://dx.doi.org/10.1016/1010-6030(95)04292-X.

5. Haritoglou, C.; Gandorfer, A.; Schaumberger, M.; Tadayoni, R.; Gandorfer, A.; Kampik, A., Light-absorbing properties and osmolarity of indocyanine-green depending on concentration and solvent medium. *Invest Ophth Vis Sci* **2003,** *44* (6), 2722-2729. DOI: 10.1167/iovs.02-1283.

6. Frangioni, J. V., In vivo near-infrared fluorescence imaging. *Curr Opin Chem Biol* **2003,** *7* (5), 626-634. DOI: 10.1016/j.cbpa.2003.08.007.

7. Lim, H. J.; Oh, C. H., Indocyanine green-based photodynamic therapy with 785nm light emitting diode for oral squamous cancer cells. *Photodiagnosis Photodyn. Ther.* **2011,** *8* (4), 337-42. DOI: 10.1016/j.pdpdt.2011.06.002.

8. Smretschnig, E.; Ansari-Shahrezaei, S.; Hagen, S.; Glittenberg, C.; Krebs, I.; Binder, S., Half-Fluence Photodynamic Therapy in Chronic Central Serous Chorioretinopathy. *Retina-J. Ret. Vit. Dis.* **2013,** *33* (2), 316-323. DOI: 10.1097/IAE.0b013e318280769c.

9. Tuchin, V. V.; Genina, E. A.; Bashkatov, A. N.; Simonenko, G. V.; Odoevskaya, O. D.; Altshuler, G. B., A pilot study of ICG laser therapy of Acne vulgaris: Photodynamic and photothermolysis treatment. *Laser Surg Med* **2003,** *33* (5), 296-310. DOI: 10.1002/lsm.10211.

10. Klein, A.; Szeimies, R. M.; Baumler, W.; Zeman, F.; Schreml, S.; Hohenleutner, U.; Landthaler, M.; Koller, M.; Babilas, P., Indocyanine green-augmented diode laser treatment of port-wine stains: clinical and histological evidence for a new treatment option from a randomized controlled trial. *Br. J. Dermatol.* **2012,** *167* (2), 333-342. DOI: 10.1111/j.1365-2133.2012.10950.x.

11. Yoneya, S.; Saito, T.; Komatsu, Y.; Koyama, I.; Takahashi, K.; Duvoll-Young, J., Binding properties of indocyanine green in human blood. *Invest Ophth Vis Sci* **1998,** *39* (7), 1286-1290.

12. Ho, C.-M.; Dhawan, A.; Hughes, R. D.; Lehec, S. C.; Puppi, J.; Philippeos, C.; Lee, P.-H.; Mitry, R. R., Use of indocyanine green for functional assessment of human hepatocytes for transplantation. *Asian J. Surg.* **2012,** *35* (1), 9-15. DOI: https://doi.org/10.1016/j.asjsur.2012.04.017.

13. Yaseen, M. A.; Yu, J.; Jung, B. S.; Wong, M. S.; Anvari, B., Biodistribution of Encapsulated Indocyanine Green in Healthy Mice. *Mol. Pharmaceut.* **2009,** *6* (5), 1321-1332. DOI: 10.1021/mp800270t.

14. Bahmani, B.; Lytle, C. Y.; Walker, A. M.; Gupta, S.; Vullev, V. I.; Anvari, B., Effects of nanoencapsulation and PEGylation on biodistribution of indocyanine green in healthy mice: quantitative fluorescence imaging and analysis of organs. *International Journal of Nanomedicine* **2013,** *8*, 1609-1620. DOI: 10.2147/Ijn.S42511.

15. El-Daly, S. M.; Gamal-Eldeen, A. M.; Abo-Zeid, M. A. M.; Borai, I. H.; Wafay, H. A.; Abdel-Ghaffar, A. R. B., Photodynamic therapeutic activity of indocyanine green entrapped in polymeric nanoparticles. *Photodiagnosis Photodyn. Ther.* **2013,** *10* (2), 173-185. DOI: 10.1016/j.pdpdt.2012.08.003.

16. Lajunen, T.; Kontturi, L. S.; Viitala, L.; Manna, M.; Cramariuc, O.; Rog, T.; Bunker, A.; Laaksonen, T.; Viitala, T.; Murtomaki, L.; Urtti, A., Indocyanine Green-Loaded Liposomes for Light-Triggered Drug Release. *Mol. Pharmaceut.* **2016,** *13* (6), 2095-2107. DOI: 10.1021/acs.molpharmaceut.6b00207.

17. Couto, D.; Freitas, M.; Porto, G.; Lopez-Quintela, M. A.; Rivas, J.; Freitas, P.; Carvalho, F.; Fernandes, E., Polyacrylic acid-coated and non-coated iron oxide nanoparticles induce cytokine activation in human blood cells through TAK1, p38 MAPK and JNK pro-inflammatory pathways. *Arch. Toxicol.* **2015,** *89* (10), 1759-1769. DOI: 10.1007/s00204-014-1325-4.

18. Bahmani, B.; Bacon, D.; Anvari, B., Erythrocyte-derived photo-theranostic agents: hybrid nano-vesicles containing indocyanine green for near infrared imaging and therapeutic applications. *Sci. Rep.* **2013,** *3*, 2180. DOI: 10.1038/srep02180.

19. Burns, J. M.; Vankayala, R.; Mac, J. T.; Anvari, B., Erythrocyte-Derived Theranostic Nanoplatforms for Near Infrared Fluorescence Imaging and Photodestruction of Tumors. *ACS Appl. Mater. Inter.* **2018,** *10* (33), 27621-27630. DOI: 10.1021/acsami.8b08005.

20. Pei, Q.; Hu, X. L.; Zheng, X. H.; Liu, S.; Li, Y. W.; Jing, X. B.; Xie, Z. G., Light-Activatable Red Blood Cell Membrane-Camouflaged Dimeric Prodrug Nanoparticles for Synergistic Photodynamic/Chemotherapy. *ACS Nano* **2018,** *12* (2), 1630-1641. DOI: 10.1021/acsnano.7b08219.

21. Wan, G. Y.; Chen, B. W.; Li, L.; Wang, D.; Shi, S. R.; Zhang, T.; Wang, Y.; Zhang, L. Y.; Wang, Y. S., Nanoscaled red blood cells facilitate breast cancer treatment by combining photothermal/photodynamic therapy and chemotherapy. *Biomaterials* **2018,** *155*, 25-40. DOI: 10.1016/j.biomaterials.2017.11.002.

22. Rao, L.; Meng, Q. F.; Bu, L. L.; Cai, B.; Huang, Q. Q.; Sun, Z. J.; Zhang, W. F.; Li, A.; Guo, S. S.; Liu, W.; Wang, T. H.; Zhao, X. Z., Erythrocyte Membrane-Coated Upconversion Nanoparticles with Minimal Protein Adsorption for Enhanced Tumor Imaging. *ACS Appl. Mater. Inter.* **2017,** *9* (3), 2159-2168. DOI: 10.1021/acsami.6b14450.

23. Piao, J. G.; Wang, L. M.; Gao, F.; You, Y. Z.; Xiong, Y. J.; Yang, L. H., Erythrocyte Membrane Is an Alternative Coating to Polyethylene Glycol for Prolonging the Circulation Lifetime of Gold Nanocages for Photothermal Therapy. *ACS Nano* **2014,** *8* (10), 10414-10425. DOI: 10.1021/nn503779d.

24. Peng, J. R.; Yang, Q.; Li, W. T.; Tan, L. W.; Xiao, Y.; Chen, L. J.; Hao, Y.; Qian, Z. Y., Erythrocyte-Membrane-Coated Prussian Blue/Manganese Dioxide Nanoparticles as H2O2-Responsive Oxygen Generators To Enhance Cancer Chemotherapy/Photothermal Therapy. *ACS Appl. Mater. Inter.* **2017,** *9* (51), 44410-44422. DOI: 10.1021/acsami.7b17022.

25. Hu, C.-M. J.; Zhang, L.; Aryal, S.; Cheung, C.; Fang, R. H.; Zhang, L., Erythrocyte membrane-camouflaged polymeric nanoparticles as a biomimetic delivery platform. *P Natl Acad Sci USA* **2011,** *108* (27), 10980-10985. DOI: 10.1073/pnas.1106634108.

26. Godfrin, Y.; Thomas, X.; Bertrand, Y.; Duget, C., L-Asparaginase Loaded into Erythrocytes (GRASPA): Principle and Interests in Acute Lymphoblastic Leukemia. *Blood* **2007,** *110* (11), 4325-4325.

27. Tang, J. C.; Partono, A.; Anvari, B., Near-Infrared-Fluorescent Erythrocyte-Mimicking Particles: Physical and Optical Characteristics. *IEEE Trans. Biomed. Eng.* **2018**. DOI: 10.1109/TBME.2018.2866368.

28. Peer, D.; Karp, J. M.; Hong, S.; Farokhzad, O. C.; Margalit, R.; Langer, R., Nanocarriers as an emerging platform for cancer therapy. *Nat. Nanotechnol.* **2007,** *2* (12), 751-760. DOI: 10.1038/nnano.2007.387.

29. Blanco, E.; Shen, H.; Ferrari, M., Principles of nanoparticle design for overcoming biological barriers to drug delivery. *Nat Biotechnol* **2015,** *33* (9), 941-951. DOI: 10.1038/nbt.3330.

30. Burns, J. M.; Jia, W.; Nelson, J. S.; Majaron, B.; Anvari, B., Photothermal treatment of port-wine stains using erythrocyte-derived particles doped with indocyanine green: a theoretical study. *J. Biomed. Opt.* **2018,** *23* (12), 1-10. DOI: 10.1117/1.JBO.23.12.121616.

31. Ebert, B.; Riefke, B.; Sukowski, U.; Kai, L. C., Cyanine dyes as contrast agents for near-infrared imaging in vivo: acute tolerance, pharmacokinetics, and fluorescence imaging. *J. Biomed. Opt.* **2011,** *16* (6), 066003. DOI: 10.1117/1.3585678.

32. Kuo, Y. C.; Wu, H. C.; Hoang, D.; Bentley, W. E.; D'Souza, W. D.; Raghavan, S. R., Colloidal Properties of Nanoerythrosomes Derived from Bovine Red Blood Cells. *Langmuir* **2016,** *32* (1), 171-179. DOI: 10.1021/acs.langmuir.5b03014.

33. Eylar, E. H.; Madoff, M. A.; Brody, O. V.; Oncley, J. L., The contribution of sialic acid to the surface charge of the erythrocyte. *J. Biol. Chem.* **1962,** *237*, 1992-2000.

34. Durocher, J. R.; Payne, R. C.; Conrad, M. E., Role of sialic acid in erythrocyte survival. *Blood* **1975,** *45* (1), 11-20.

35. Kwon, S.; Davies-Venn, C.; Sevick-Muraca, E. M., In vivo dynamic imaging of intestinal motions using diet-related autofluorescence. *Neurogastroent. Motil.* **2012,** *24* (5), 494-497. DOI: 10.1111/j.1365-2982.2012.01886.x.

36. Eguchi, S.; Takatsuki, M.; Yamanouchi, K.; Hidaka, M.; Soyama, A.; Tomonaga, T.; Tajima, Y.; Kanematsu, T., Indocyanine Green Dye Excretion in Bile Reflects Graft Function After Living Donor Liver Transplantation. *Transplantation* **2009,** *88* (5), 747-748. DOI: 10.1097/TP.0b013e3181b2a22a.

37. Koren, E.; Torchilin, V. P., Drug Carriers for Vascular Drug Delivery. *IUBMB Life* **2011,** *63* (8), 586-595. DOI: 10.1002/iub.496.

38. Moghimi, S. M., Mechanisms of Splenic Clearance of Blood-Cells and Particles - Towards Development of New Splenotropic Agents. *Adv. Drug Deliver. Rev.* **1995,** *17* (1), 103-115. DOI: Doi 10.1016/0169-409x(95)00043-7.

39. Mebius, R. E.; Kraal, G., Structure and function of the spleen. *Nat. Rev. Immunol.* **2005,** *5* (8), 606-616. DOI: 10.1038/nri1669.

40. Pivkin, I. V.; Peng, Z. L.; Karniadakis, G. E.; Buffet, P. A.; Dao, M.; Suresh, S., Biomechanics of red blood cells in human spleen and consequences for physiology and disease. *P Natl Acad Sci USA* **2016,** *113* (28), 7804-7809. DOI: 10.1073/pnas.1606751113.

41. Muzykantov, V. R.; Murciano, J. C.; Taylor, R. P.; Atochina, E. N.; Herraez, A., Regulation of the complement-mediated elimination of red blood cells modified with biotin and streptavidin. *Anal. Biochem.* **1996,** *241* (1), 109-19. DOI: 10.1006/abio.1996.0384.

42. Villa, C. H.; Anselmo, A. C.; Mitragotri, S.; Muzykantov, V., Red blood cells: Supercarriers for drugs, biologicals, and nanoparticles and inspiration for advanced delivery systems. *Adv. Drug Deliver. Rev.* **2016,** *106* (Pt A), 88-103. DOI: 10.1016/j.addr.2016.02.007.

43. Hagmann, M., Immunology - A new way to keep immune cells in check. *Science* **2000,** *288* (5473), 1945-1946. DOI: DOI 10.1126/science.288.5473.1945.

44. Oldenborg, P. A.; Zheleznyak, A.; Fang, Y. F.; Lagenaur, C. F.; Gresham, H. D.; Lindberg, F. P., Role of CD47 as a marker of self on red blood cells. *Science* **2000,** *288* (5473), 2051-2054. DOI: DOI 10.1126/science.288.5473.2051.

45. Mac, J. T.; Nunez, V.; Burns, J. M.; Guerrero, Y. A.; Vullev, V. I.; Anvari, B., Erythrocyte-derived nano-probes functionalized with antibodies for targeted near infrared fluorescence imaging of cancer cells. *Biomed Opt Express* **2016,** *7* (4), 1311-1322. DOI: 10.1364/Boe.7.001311.

46. Mohanty, J. G.; Nagababu, E.; Rifkind, J. M., Red blood cell oxidative stress impairs oxygen delivery and induces red blood cell aging. *Front. Physiol.* **2014,** *5*, 84. DOI: 10.3389/fphys.2014.00084.

47. Kim, J.; Lee, H.; Shin, S., Advances in the measurement of red blood cell deformability: A brief review. *J. Cell. Biotech.* **2015,** *1* (1), 63-79. DOI: 10.3233/JCB-15007.

48. Nash, G. B.; Meiselman, H. J., Red-Cell and Ghost Viscoelasticity - Effects of Hemoglobin Concentration and Invivo Aging. *Biophys J* **1983,** *43* (1), 63-73. DOI: Doi 10.1016/S0006-3495(83)84324-0.

49. Chien, S., Red-Cell Deformability and Its Relevance to Blood-Flow. *Annu. Rev. Physiol.* **1987,** *49*, 177-192. DOI: DOI 10.1146/annurev.ph.49.030187.001141.

50. Bratosin, D.; Mazurier, J.; Tissier, J. P.; Estaquier, J.; Huart, J. J.; Ameisen, J. C.; Aminoff, D.; Montreuil, J., Cellular and molecular mechanisms of senescent erythrocyte phagocytosis by macrophages. A review. *Biochimie* **1998,** *80* (2), 173-195. DOI: Doi 10.1016/S0300-9084(98)80024-2.

51. Wisse, E.; Braet, F.; Luo, D. Z.; DeZanger, R.; Jans, D.; Crabbe, E.; Vermoesen, A., Structure and function of sinusoidal lining cells in the liver. *Toxicol. Pathol.* **1996,** *24* (1), 100-111. DOI: Doi 10.1177/019262339602400114.

52. Zhang, Y. N.; Poon, W.; Tavares, A. J.; McGilvray, I. D.; Chan, W. C. W., Nanoparticle-liver interactions: Cellular uptake and hepatobiliary elimination. *J. Control. Release* **2016,** *240*, 332-348. DOI: 10.1016/j.jconrel.2016.01.020.

53. Yu, F. B.; Jiang, T. Y.; Zhang, J. H.; Cheng, L. H.; Wang, S. L., Galactosylated liposomes as oligodeoxynucleotides carrier for hepatocyte-selective targeting. *Pharmazie* **2007,** *62* (7), 528-533. DOI: 10.1691/ph.2007.7.6232.

54. Zhang, X. M.; Zhang, Q.; Peng, Q.; Zhou, J.; Liao, L. F.; Sun, X.; Zhang, L.; Gong, T., Hepatitis B virus preS1-derived lipopeptide functionalized liposomes for targeting of hepatic cells. *Biomaterials* **2014,** *35* (23), 6130-6141. DOI: 10.1016/j.biomaterials.2014.04.037.

55. Gao, D. Y.; Lin, T. T.; Sung, Y. C.; Liu, Y. C.; Chiang, W. H.; Chang, C. C.; Liu, J. Y.; Chen, Y. C., CXCR4-targeted lipid-coated PLGA nanoparticles deliver sorafenib and overcome acquired drug resistance in liver cancer. *Biomaterials* **2015,** *67*, 194-203. DOI: 10.1016/j.biomaterials.2015.07.035.

56. Desilets, J.; Lejeune, A.; Mercer, J.; Gicquaud, C., Nanoerythrosomes, a new derivative of erythrocyte ghost: IV. Fate of reinjected nanoerythrosomes. *Anticancer Res.* **2001,** *21* (3B), 1741-7.

57. Patel, G.; Kher, G.; Misra, A., Preparation and evaluation of hepatic stellate cell selective, surface conjugated, peroxisome proliferator-activated receptor-gamma ligand loaded liposomes. *J. Drug Target.* **2012,** *20* (2), 155-165. DOI: 10.3109/1061186x.2011.610800.

58. Tan, J. F.; Thomas, A.; Liu, Y. L., Influence of red blood cells on nanoparticle targeted delivery in microcirculation. *Soft Matter* **2012,** *8* (6), 1934-1946. DOI: 10.1039/c2sm06391c.

59. Gentile, F.; Curcio, A.; Indolfi, C.; Ferrari, M.; Decuzzi, P., The margination propensity of spherical particles for vascular targeting in the microcirculation. *J. Nanobiotechnology* **2008,** *6*, 9. DOI: 10.1186/1477-3155-6-9.

60. Fish, M. B.; Fromen, C. A.; Lopez-Cazares, G.; Golinski, A. W.; Scott, T. F.; Adili, R.; Holinstat, M.; Eniola-Adefeso, O., Exploring deformable particles in vascular-targeted drug delivery: Softer is only sometimes better. *Biomaterials* **2017,** *124*, 169-179. DOI: https://doi.org/10.1016/j.biomaterials.2017.02.002.

61. Watson, C. Y.; Molina, R. M.; Louzada, A.; Murdaugh, K. M.; Donaghey, T. C.; Brain, J. D., Effects of zinc oxide nanoparticles on Kupffer cell phagosomal motility, bacterial clearance, and liver function. *Int. J. Nanomed.* **2015,** *10*, 4173-4184. DOI: 10.2147/Ijn.S82807.

62. Bourrinet, P.; Bengele, H. H.; Bonnemain, B.; Dencausse, A.; Idee, J. M.; Jacobs, P. M.; Lewis, J. M., Preclinical safety and pharmacokinetic profile of ferumoxtran-10, an ultrasmall superparamagnetic iron oxide magnetic resonance contrast agent. *Invest. Radiol.* **2006,** *41* (3), 313-324. DOI: DOI 10.1097/01.rli.0000197669.80475.dd.

63. Suckow, M. A.; Danneman, P.; Brayton, C., *The laboratory mouse*. CRC Press: Boca Raton, Fla., 2001; p 168 p.

64. Serfilippi, L. M.; Pallman, D. R.; Russell, B., Serum clinical chemistry and hematology reference values in outbred stocks of albino mice from three commonly used vendors and two inbred strains of albino mice. *Contemp. Top. Lab Anim. Sci.* **2003,** *42* (3), 46-52.

65. Marshall, M. V.; Draney, D.; Sevick-Muraca, E. M.; Olive, D. M., Single-dose intravenous toxicity study of IRDye 800CW in Sprague-Dawley rats. *Mol. Imaging Biol.* **2010,** *12* (6), 583-94. DOI: 10.1007/s11307-010-0317-x.

66. Shi, J.; Gilbert, G. E.; Kokubo, Y.; Ohashi, T., Role of the liver in regulating numbers of circulating neutrophils. *Blood* **2001,** *98* (4), 1226-30.

67. Hochreiter-Hufford, A.; Ravichandran, K. S., Clearing the dead: apoptotic cell sensing, recognition, engulfment, and digestion. *Cold Spring Harb. Perspect. Biol.* **2013,** *5* (1), a008748. DOI: 10.1101/cshperspect.a008748.

68. Lu, N.; Zhou, Z., Membrane trafficking and phagosome maturation during the clearance of apoptotic cells. *Int. Rev. Cell Mol. Biol.* **2012,** *293*, 269-309. DOI: 10.1016/B978-0-12-394304-0.00013-0.

69. Semple, J. W.; Italiano, J. E., Jr.; Freedman, J., Platelets and the immune continuum. *Nat. Rev. Immunol.* **2011,** *11* (4), 264-74. DOI: 10.1038/nri2956.

70. Lalor, P. F.; Herbert, J.; Bicknell, R.; Adams, D. H., Hepatic sinusoidal endothelium avidly binds platelets in an integrin-dependent manner, leading to platelet and endothelial activation and leukocyte recruitment. *Am. J. Physiol. Gastrointest. Liver Physiol.* **2013,** *304* (5), G469-78. DOI: 10.1152/ajpgi.00407.2012.

71. Radomski, A.; Jurasz, P.; Alonso-Escolano, D.; Drews, M.; Morandi, M.; Malinski, T.; Radomski, M. W., Nanoparticle-induced platelet aggregation and vascular thrombosis. *Br. J. Pharmacol.* **2009,** *146* (6), 882-893. DOI: 10.1038/sj.bjp.0706386.

72. Yun, S.-H.; Sim, E.-H.; Goh, R.-Y.; Park, J.-I.; Han, J.-Y., Platelet Activation: The Mechanisms and Potential Biomarkers. *Biomed Res. Int.* **2016,** *2016*, 9060143. DOI: 10.1155/2016/9060143.

73. O'Connell, K. E.; Mikkola, A. M.; Stepanek, A. M.; Vernet, A.; Hall, C. D.; Sun, C. C.; Yildirim, E.; Staropoli, J. F.; Lee, J. T.; Brown, D. E., Practical murine hematopathology: a comparative review and implications for research. *Comp. Med.* **2015,** *65* (2), 96-113.

Chapter 4: Folate-Functionalized Erythrocyte-Derived Nanoparticles Co-loaded with Indocyanine Green/Doxorubicin Hydrochloride for Near-infrared (NIR) 808 nm Pulsed-laser Combined Chemo-Phototherapy of Ovarian Cancer

4.1 Abstract

Remotely controlled, localized drug delivery is highly desirable for potentially minimizing the systemic toxicity induced by administration of chemotherapy drugs. Nanoparticle-based drug delivery systems provide a highly promising approach for localized drug delivery and are an emerging field of interest in cancer treatment. Here, we demonstrate near-IR light-triggered release of chemotherapeutic drug that have been co-encapsulated with NIR chromophore in erythrocyte-derived nanoparticles. Chemotherapeutic drug, doxorubicin HCl, and NIR chromophore, indocyanine green, were delivered to SKOV3 ovarian cancer cells. Using a pulse-laser, combination of photothermal heating and chemotherapy induced cancerous cell death and increase survivability of SKOV3-tumor bearing mice. This method provides localized treatment and release of chemotherapy drugs deliverable at a specific treatment site over a specific time window, with the potential for greatly minimized side effects. Histological evaluation of subcutaneous tissue revealed minor thermal damage, apoptosis and necrosis in laser/saline group and substantial damage in the laser/F-IDNETs group. The laser/F-IDNETs group showed a significant tumor reduction compared to laser/saline.

4.2 Introduction

Ovarian cancer is the most lethal malignancy affecting the female reproductive system. Nearly 75% of individuals with ovarian cancer are first diagnosed with disseminated intraperitoneal disease (stage III). While some tumors can be removed surgically, others may not be resectable due to their locations. For example, procedures such as diaphragm stripping, splenectomy, distal pancreatectomy, liver resection, or cholecystectomy may be required during surgical removal of ovarian peritoneal tumors. Despite non-specific toxicity and multi-drug resistance problems, chemotherapy and surgery remain as gold standards in treating cancer.[1-2] For example, Doxorubicin HCl (DOX), an anthracycline ring antibiotic, is a highly effective anti-neoplastic agent used in leukemia chemotherapy. However, the severe toxic side-effects such as cardiotoxicity, alopecia, vomiting, leucopenia, and stomatitis have hindered the successful use of DOX.[3-5] One strategy for reducing the side effects and systemic toxicity of chemodrugs and improving therapeutic efficacy is to combine with other treatment modalities.

Nanoparticle-based anticancer drug delivery promises a disruptive technology to accommodate multiple drug molecules or therapeutic modalities to achieve synergistic therapeutic effects.[6-8] To improve drug delivery and bioavailability, nanoparticles responding to external stimulations (e.g., light, magnetic field, ultrasound) or internal stimulations (e.g., reduction/oxidation, pH, and enzymatic activity) have been developed with excellent efficacies.[8] These stimuli can provide excellent spatiotemporal and dosage control for drug release in tumor tissues with reduced systemic toxicity. Recently, phototherapy has attracted considerable attention as a powerful technique for treating

cancers as well as malignant tumors with minimal invasiveness. One such phototherapeutic approach is photothermal therapy (PTT) which require absorption of incoming light by an agent to generate heat for killing cancer cells.[9-10] NIR laser-mediated thermal therapy using wavelengths in the range of ≈ 700-900 nm (spectral window of biological transparency)[11] has been investigated to induce release of drug molecules to target sites. To date, indocyanine green remains as the only FDA-approved NIR-activated agent for clinical applications ranging from ophthalmic angiography, cardiocirculatory measurements, assessment of hepatic function, and blood flow evaluation. ICG has also been investigated for potential applications in mapping sentinel lymph nodes to imaging intracranial aneurysm and cerebral arteriovenous malformations.[12-14] ICG has also been investigated as a photosensitizer for phototherapy due to its ability to generate heat and singlet oxygen upon laser irradiation.[15-16] However, the drawbacks of using ICG include its short half-life within plasma (2 – 4 minutes), with nearly exclusive uptake by hepatocytes and elimination through the hepatobiliary mechanism.

Encapsulation of ICG and DOX into a nanocargo can provide a method to shield the non-specific interactions with blood plasma proteins and ultimately extend the circulation times of both the agents, so that higher amounts of drug payload can be accumulated at specific target sites and also facilitate excellent therapeutic efficacies.[17-18] Furthermore, molecular targeting strategy can also enhance the drug payload accumulation at the specific target sites. For example, a particularly promising target for ovarian cancer is FRα, which is over-expressed in both primary tumor tissue and in

metastatic tumor deposits.[19-23] The tumor specificity and high levels of FRα expression provide the basis to target FRα as a biomarker associated with ovarian cancer.

For example, liposomes co-encapsulating ICG and DOX activated by NIR light have shown enhanced drug accumulation at the tumor site when compared with free drugs, and eradicated tumors by mediating synergistic chemo-photothermal effects.[24] In another recent study, anti-HER2 functionalized ICG-DOX encapsulated in polymeric constructs (PEG-PLGA diblock copolymeric nanoparticles) exhibited cytotoxicity in MDA-MB-453/HER2(+) cells upon 6 W/cm^2 continuous wave (CW) 808 nm light irradiation for 5 minutes, with resulting cell death being higher than when the dosages of encapsulated DOX or ICG alone were twice as much.[25] However, the poor circulation times of liposomes and polymeric nanoparticles as well as the use of CW lasers which will increase the overall treatment time can severely restricts their usage in biomedical clinics.

Erythrocyte-derived drug delivery systems have been investigated as a biomimetic coating for nanomaterials with various functions.[26-30] We reported the first demonstration on the engineering of nanosized red blood cell derived vesicles loaded with ICG for fluorescence imaging and photodestruction of human dermal microvascular endothelial cells.[31] We refer to these constructs as NIR erythrocyte-mimicking transducers (NETs). Upon NIR light activation, NETs are capable to transduce the absorbed photons energy to emit fluorescence, generate heat or mediate production of reactive oxygen species (ROS).[32] The blood circulation kinetics of NETs in healthy mice

show that 11% of initial injection still remain in blood for at least 48 hours post tail-vein injection.[33]

In this study, we have engineered erythrocyte-derived nanosized vesicles which can encapsulate both ICG and DOX (IDNETs). We show for the first time that IDNETs can be successfully functionalized with folate moieties to achieve molecular targeting of FR-α receptors over-expressed on the surface of SKOV3 ovarian cancer cells. IDNETs induced a significant temperature in response to 808 nm pulsed laser irradiation which further triggered the release of chemotherapeutic drug payload, DOX within the specific target site. We demonstrate the therapeutic effectiveness of folate functionalized IDNETs by combining NIR light-triggered photothermolysis along with the delivery of DOX on the destruction of subcutaneous xenograft ovarian tumors in mice with shorter irradiation times (in the order of ms as opposed to minutes for CW laser) and improved survival rates.

4.3 Materials and Methods

4.3.1 Fabrication of F-NETs/F-IDNETs

Erythrocytes were isolated from whole human blood (Biological Specialty Corporation, Colmar, PA) and washed in ≈310 mOsm PBS (referred to as the 1X PBS solution, Fisher Scientific, Hampton, NH, USA) at ≈ (4178 x g) 4200 x g at 4°C for 10 mins. Packed erythrocytes were subject to hypotonic (≈80 mOsm, 0.25X PBS) treatment to deplete the hemoglobin content of the cell, resulting in erythrocyte ghosts (EGs), 46419 x g at 4°C for 20 mins. Micron-sized EGs were subject to sonication for: (1) making nano-sized EGs

and (2) functionalization of folate (folate-DSPE-PEG, Nanosoft Polymers, Winston-Salem, NC, USA) using tip-sonicator (FB705, Fisher Scientific, Hampton, NH, USA). Folate functionalized nano-EGs were concentrated down prior to loading in ultracentrifuge at 76974 x g at 4°C for 1 hour. To make folate-functionalized NETs (F-NETs), 10mL of nEGs were concentrated and resuspended in 1mL 1XPBS, 3mL of 2mg ICG, 3mL Sorenson's buffer. To make F-IDNETs, Doxorubicin HCl (VWR International, Radnor, PA, USA) and Indocyanine green (MP Biomedicals, Santa Ana, CA, USA) were mixed at a 1:1 molar ratio for 5 minutes prior to loading. 10 mL of nEGs were concentrated and resuspended in 1mL 1xPBS, 3 mL of 2 mg ICG, 3 mL of 1 mg DOX, and 3mL Sorenson's buffer. Loading concentration was ≈ 775μM. NETs samples were centrifuged at 76974xg at 4°C for 1 hour and washed twice. NETs fabrication depicted in Figure 4.1A.

4.3.2 Characterization

The hydrodynamic diameters and zeta potentials were measured by dynamic light scattering (DLS) (Zetasizer Nano ZS90, Malvern Instruments Ltd, Westborough, MA, USA). We fitted lognormal functions to the DLS-based estimates of NETs' hydrodynamic diameters. Absorption spectra were obtained using a UV-visible spectrophotometer (Jasco-V670 UV-vis spectrophotometer, JASCO, Easton, MD, USA) with optical path length of 1 cm. Fluorescence emission spectra of ICG-containing samples in response to 720 ± 2.5 nm excitation light, spectrally filtered from a 450 W xenon lamp, were recorded in the range of 735–900 nm using a fluorometer (Fluorolog-3 spectrofluorometer, Horiba Jobin Yvon, Edison, NJ, USA). DOX emission was collected

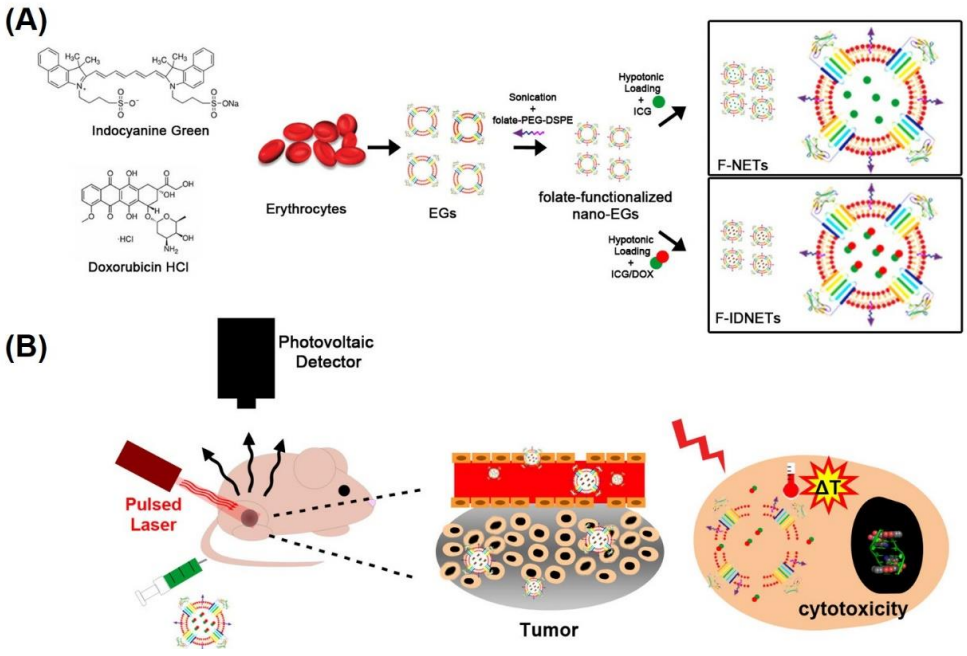

Figure 4.1: (A) Schematic illustration of preparation procedure of F-NETs and F-IDNETs. (B) Schematic illustration of NIR pulsed laser triggered combinational chemo-PTT therapy through intravenous injection.

from 485 – 700 nm with 470 ± 2.5 nm excitation light and folate emission was collected from 365 – 650 nm with 350 ± 2.5 nm excitation light.

4.3.3 Temperature Rise Measurements

Figure 4.2 depicts schematic drawing of photovoltaic detector set-up for temperature rise calculations. Blackbody emission in the range 3-7 μm was measured by photovoltaic detector (PVD): PVI-4TE-6 (Vigo Systems, Poland) with 25 mm f/1 lens (Edmund Optics, 69649, BBAR 3-5μm) placed 25 mm from detector. A 5 mm aperture was used during calibration to match a 5 mm laser spot size for pulsed laser irradiations. An aluminum block was painted black with black india Higgins ink (Chartpak, Leeds, MA, USA) used as blackbody mimic. The Al block was heated on hotplate and transferred to measurement surface, 12.4 cm from detector (Figure 4.S1A). Surface temperature in

cooling phase was measured using a thermocouple (Item#:HYPO-33-1-K-G-60-SMPW-M, Omega Engineering, Stamford, CT), connected to Vernier LabQuest. Temperature and voltage were plotted in Mathworks MatLab and fitted to a exponential decay for temperature calibration. A representative temperature calibration plot is shown in Figure 4.S1B.

4.3.4 Laser Irradiation

For pulsed-laser irradiations, we used Lumics LuOcean Mini 4 808 ±10 nm coupled to a 10-mm aperture collimator VIS-NIR, SMA 88170 (Edmund Optics, NJ, USA). Laser energy was determined using Ophir Energy Meter (3(150)-HE-SH) (Ophir Optronics, Jerusalem, Israel). A laser energy calibration was generated to determine energy densities.

Samples were irradiated with D_o = 50 and 90 J/cm^2, t_p = 500 ms, laser spot size = 5 mm in a glass-bottomed Petri dish (MatTek Corporation, Ashland, MA, USA) and voltages were measured by PVD detector as shown in Figure 4.S1C. Data was analyzed in MathWorks MatLab.

4.3.5 Photostability of ICG in NETs

After irradiation, samples containing ICG were measured by UV-Vis to determine ICG degradation after exposure to laser dosages D_o = 50 and 90 J/cm^2. Percentage of ICG remaining was calculated as:

$$\% \text{ ICG Remaining} = \frac{A_{808\ (light)}}{A_{808\ (dark)}} \times 100 \quad (1)$$

4.3.6 Effects of pH and light on DOX release

To investigate the effects of pH and light-triggered release of DOX, IDNETs and F-IDNETs were diluted in PBS (pH 5.5 or pH 7.6) and irradiated using D_o = 25 J/cm^2. NETs were diluted to A_{808} = 10 in PBS (pH 5.5 or pH 7.6) and irradiated using fluence of 25 J/cm^2 in 20 μL samples. 50 μL of irradiated sample was diluted with 450 μL of PBS (A_{808} = 1) and filtered using Amicon Ultra-4 filter tubes (EMD Millipore, Burlington, MA, USA) at 4k rpm for 10 mins. For dark controls, NETs were diluted to A_{808} = 1 in PBS (at pH 5.5 or pH 7.6) and 500 μL was filtered using Amicon Ultra-4 filter tubes.

After filtration, 200 μL of supernatant was collected into 96-well plate. Additionally, pellet was resuspended to original volume of 500 μL and 200 μL of sample was collected into 96-well plate. DOX fluorescence was observed at excitation 470 nm and emission 590 nm (peak DOX emission) using Molecular Devices SpectraMax M3 plate reader (Molecular Devices, San Jose, CA, USA). Percentage of DOX release was quantified by the following equation:

$$\% \text{ DOX release} = \frac{Fl_{Sup}}{Fl_{Sup} + Fl_{Pellet}} \times 100 \quad (2)$$

4.3.7 Cell Culture

SKOV3 ovarian cancer cells (ATCC, Manassas, VA) were cultured in Rosewell Park Memorial Institute (RPMI) 1640 medium (Mediatech Inc., Manassas, VA) supplemented with 10% fetal bovine serum (FBS) and 1% penicillin/streptomycin (Corning Inc.,

Corning, NY, USA) at 37°C in 5% humidified CO_2. Cells were used for *in vitro* experiments and implanted in Nu/J female nude mice to induce tumors.

4.3.8 Fluorescence Imaging

We incubated NETs, IDNETs, F-NETs and F-IDNETs with SKOV3 ovarian cancer cells. We added 4 x 10^5 cells in 200 μL of RPMI 1640 medium supplemented with 10% FBS, and 1% Penicillin/Streptomycin to each well of a 96-well plate. Cell suspensions were plated in 5% CO_2 overnight. All samples were diluted to have same absorbance at 808 nm. On the following day, the cells were washed and incubated with various agents consisting of 1X PBS, free ICG, free DOX, free ICG-DOX, NETs, ID-NETs, F-NETs or F-IDNETs in separate wells for four hours in the dark at 37 °C. After incubation, cells were subsequently washed twice with 1X PBS and fixed using 4% paraformaldehyde (Electron Microscopy Sciences, Hatfield, PA, USA) permeabilized with 2% Tween-20 (Sigma Aldrich, St. Louis, MO, USA), and finally incubated with 300 nM DAPI for 5 minutes to stain the nuclei for fluorescence imaging.

NIR fluorescence emission (> 770 nm) in response to 740 ± 30 nm excitation by a Nikon halogen lamp was captured by an electron multiplier gained CCD camera (Quant EM-CCD, C9100-14 Hamamatsu, Shizuoka-ken, Japan). The camera exposure time was set at 0.1 s. Fluorescence emission from DOX in the range 524 ± 24 nm was collected in response to 485 ± 35 nm excitation by the Nikon halogen lamp. Fluorescence emission from DAPI-stained nucleiin the range of 435–485 nm was collected in response to 360 ± 20 nm excitation by the Nikon halogen lamp. We present falsely-colored microscopic

fluorescent images as the overlay of the NIR emission due to ICG (red channel), DOX emission (green channel) and visible emission due to DAPI (blue channel).

4.3.9 Cell Viability Assay MTT

SKOV3 cells were plated in 96-well plate for standard curve. SKOV3 cells incubated with 1XPBS, free ICG, free DOX, free ICG-DOX, NETs, ID-NETs, F-NETs, or F-IDNETs were plated in a 24-well plate in triplicate. Dark controls were subject to similar treatment, in absence of pulsed laser irradiation. SKOV3 cells were plated and left overnight. On the following day, SKOV3 cells were washed with 1XPBS and incubated with 250µL RPMI 1640 supplemented with 10% FBS and 1% Penicillin/Streptomycin and 250µL of sample were incubated for 4 hours at 37°C, supplemented with 5% CO_2. Cells were then washed twice with 1XPBS and trypsinized. Cells were concentrated to 50µL samples for irradiation. After irradiation (D_o = 50 or 90 J/cm^2, t_p = 500 ms), cells were returned to plate and incubated overnight at 37°C, in presence of 5% CO_2. On the following day, MTT reagent (Thiazolyl Blue Tetrazolium Bromide, Sigma Aldrich, St. Louis, MO, USA) was added and incubated for 4 hours, at 37°C, in presence of 5% CO_2. After 4 hour incubation, the solution was aspirated and formazan crystals were dissolved in 100% DMSO (Corning Inc., Corning, NY, USA). Absorbance was measured at 572 nm using Molecular Devices SpectraMax M3 plate reader (Molecular Devices, San Jose, CA, USA). Cell viability was determined using calibration curve.

4.3.10 Animal Study

Female Nu/J mice (20-25 g, 6-8 weeks) were purchased from Jackson Laboratory (Bar Harbor, Maine, USA) and utilized in this study under a protocol approved by the University of California, Riverside Institutional Animal Care and Use Committee (A-20170038). We injected ≈ 1 x 10^7 SKOV3 cancer cells subcutaneously into the thighs. Mice were monitored until the tumor sizes reached approximately 15mm^3. The tumor volume was calculated as D x d^2 / 2, where D and d were the larger and smaller diameter of each tumor.

Tumor-bearing mice were randomly divided into six groups with six animals in each group. Group 1 received PBS with laser irradiation, Group 2 received free ICG (2.67 mg/kg) with laser irradiation, Group 3 received free DOX with laser irradiation (0.76 mg/kg), Group 4 received ICG+DOX with laser irradiation (2.67 mg/kg ICG and 0.76 mg/kg DOX), Group 5 received F-NETs (2.67 mg/kg ICG) with laser irradiation and Group 6 received F-IDNETs (2.67 mg/kg ICG and 0.76 mg/kg DOX) with laser irradiation, respectively. We administered 100 μL of the agent (PBS, free ICG, free DOX, free ICG+DOX, F-NETs, or F-IDNETs) intravenously via tail vein injection while the animal was anesthetized. Laser irradiation was performed at 24 h post injection with a beam diameter of 5 mm using D_o = 90 J/cm^2. A representative schematic of animal study is shown in Figure 4.1B. We measured the temperature change in response to the 808 nm laser irradiation with PVD calibrated with temperature probe measuring the surface of a heated black-painted aluminum block as shown in Figure 4.S1A and 4.S1D. Following the experimental procedures, animals were allowed to recover. We assessed the efficacies

of different NETs formulations mediating chemo-photothermal destruction in tumor size by measuring the tumor volumes following each treatment at every alternate day and for up to 14 days after laser irradiation. We estimated the relative tumor volumes (V/V_o) during this time interval by dividing the volume of each tumor (V) on the measurement day by the initial tumor volume (V_o) on the day of the laser irradiation. All the animals were subsequently euthanized on day 14.

4.3.11 Histological and Caspase 3 staining:

A subset of mice from each group was euthanized at day 0 post laser irradiation for histological analysis. Tumor, liver, spleen, kidney, lung and heart were dissected and embedded in OCT-blocks followed by sectioning at a depth of 10 μm per each slice using a cryostat microtome (CM1950 cryostat, Buffalo Grove, Illinois, USA). The sections were subjected to H&E (hematoxylin and eosin) staining to monitor the extent of necrotic tissue damage. Tumor tissue sections were also stained with fluorescein isothiocyanate (FITC)-labeled caspase 3 antibody (BD Biosciences, San Diego, USA) to measure the extent of apoptotic damage. Fluorescent emission (524 ± 24 nm) in response to 485 ± 35 nm excitation by a Nikon Mercury/Xenon arc lamp was captured by an EM-CCD camera with exposure time set at 0.1 s. Mean and SDs of the image intensities (n = 3 images) were quantified using ImageJ. The H&E stained slides were examined under a light microscope (Nikon Eclipse Ti-S).

4.4 Results and Discussion

Zeta potentials of NETs, F-NETs, ID-NETs, and F-IDNETs as -14.52 ± 1.39,-12.68 ± 0.64, -15.12 ± 0.82, -12.26 ± 0.92 mV, respectively (Figure 4.2A). Folate functionalization, results in statistically significant (* $p < 0.05$) increased zeta potential of F-NETs and F-IDNETs compared to its nonfunctionalized counterpart. Hydrodynamic distribution profiles of NETs, F-NETs, ID-NETs, and F-IDNETs fabricated using 775

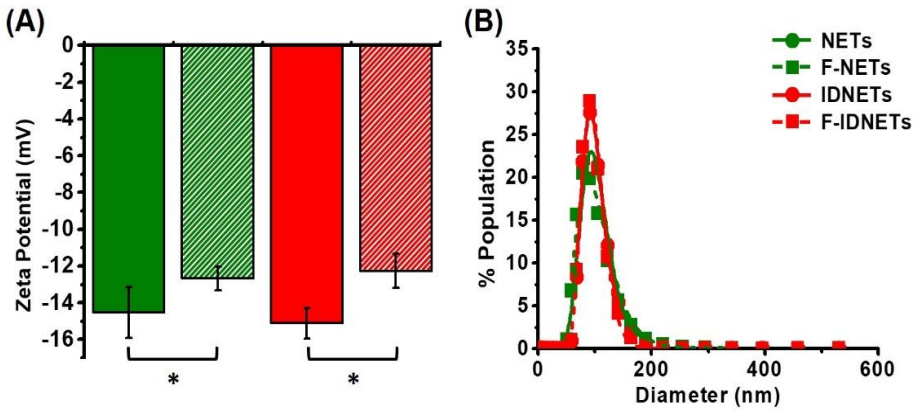

Figure 4.2: Physical Characterization of NETs (A) Zeta Potential, (B) Diameter Distributions.

μM ICG ± DOX were 92.98, 87.38, 91.15, and 93.01 nm, respectively (Figure 4.2B). No significant changes in size distribution observed between samples.

The absorption spectra of free formulations of ICG (17.3 μM), DOX (2.6 μM) and ICG+DOX (17.6 μM and 2.6 μM) dissolved in 1XPBS are shown in Figure 4.3A. The peaks of ICG at 690 and 776 nm correspond to H-like aggregate and monomeric forms of ICG, respectively.[34] DOX absorbs in the visible region with a peak absorbance at 480 nm. Upon mixing the ICG and DOX together, ICG peaks shift to 700 and 782 nm along with the emergence of a spectral shoulder around 850 nm indicating J-like aggregates.[35]

Interaction of DOX and ICG indicated by J-like aggregates as well as decreased both DOX and ICG fluorescence (Figure 3B) when compared to their individual counterparts.

ICG in NETs and IDNETs formulations is predominantly in monomeric form around 800 nm (Figure 4.3C). A bathochromic (red) spectral shift in the monomeric absorption of free ICG from 776 to 800 nm in NETs is consistent with our previous results.[31] This shift can be attributed to the binding of ICG molecules to phospholipids and membrane proteins of the NETs, causing a change in molecular energy levels of ICG, as well as the local solvent environment surrounding ICG within the NETs. IDNETs and

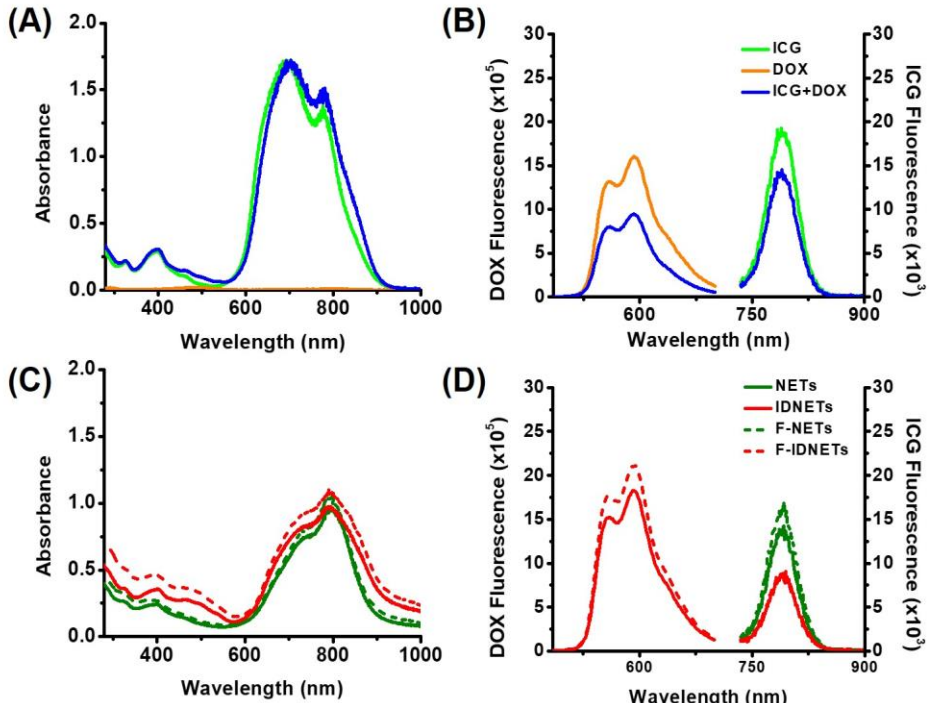

Figure 4.3: Optical Characterization. (A) Absorbance and (B) Fluorescence of ICG, DOX, ICG+DOX (conc), (C) Absorbance and (D) Fluorescence of NETs, IDNETs, f-NETs, f-IDNETs. DOX Fluorescence (Left-Y Axis, λ_{ex} = 470 nm). ICG Fluorescence (Right-Y Axis, λ_{ex} = 720 nm)

F-IDNETs have increased H-like aggregate compared to NETs and F-NETs as well as the appearance of a J-like aggregate shoulder at 860 nm, similar to that of ICG+DOX.

Absorbance values in the NIR range of 600-900 nm indicate ICG absorbance. Presence of peak around 470 nm are from DOX, indicating successful encapsulation of both ICG and DOX within NETs.

DOX (left Y-axis) and ICG (right Y-axis) fluorescence in response to shown in Figure 3D as a double-Y axis. DOX fluorescence in response to 470 nm excitation. ICG fluorescence for ID-NETs is slightly quenched due to interactions with DOX similar to that of ICG+DOX in 1XPBS. Additional confirmation of folate-functionalization measured by weak folate fluorescence, indicating a spectral peak around 440 nm in response to 350 nm photo-excitation (Figure 4.S2).

Figure 4A and 4B show representative temperature rise profiles at D_o = 50 J/cm^2 and 90 J/cm^2 of samples. The average temperature rise of NETs was 13.12 ± 0.86 °C

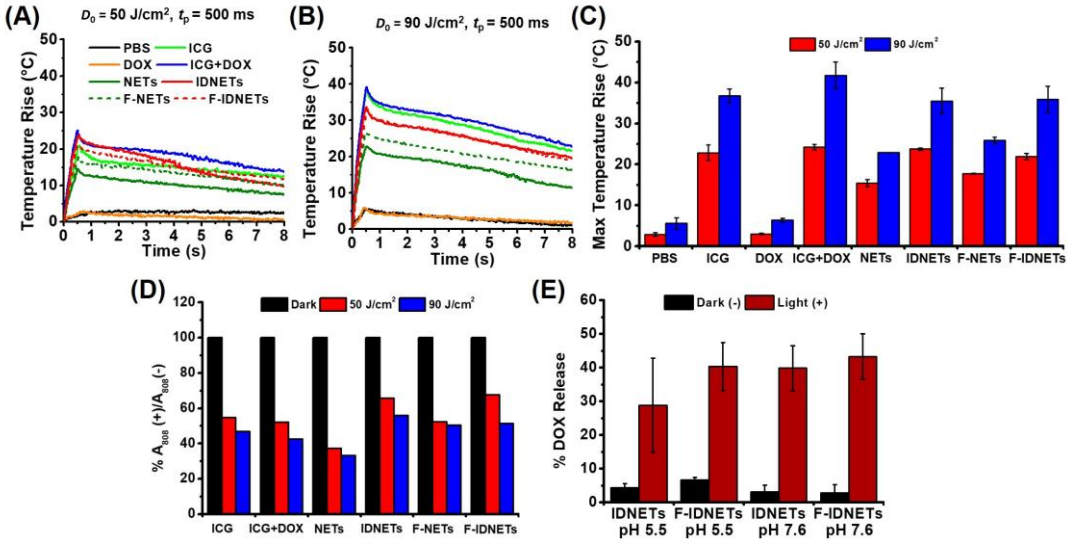

Figure 4.4: Temperature Rise (A) Samples in solution at D_o = 50 J/cm^2 (B) 90 J/cm^2. Absorbance of samples in dark (no light), 50 J/cm^2, and 90 J/cm^2 (C) Average max temperature rise, (D) Percentage of ICG remaining after irradiation, (E) DOX leakage in response to light and pH.

whereas IDNETs had about 20.97 ± 0.16 °C in solution (Figure 4C). Larger temperature rise from samples containing ICG and DOX attributed to spectral shift and J-like aggregate resulting in increased total absorption for pulsed laser (808 ± 10 nm). In general, non-ICG containing samples had minimal temperature rise (2 – 5 °C) in response to pulsed laser irradiation whereas ICG containing samples had 13 – 22 °C (D_o = 50 J/cm^2) and 20 – 40 °C (D_o = 90 J/cm^2) temperature rise. Absorption at 808 nm of ICG-containing samples after laser irradiation indicate 30-60 % ICG degradation as a result of light.

Effects of pH and laser irradiation of DOX release shown in Figure 4.4E. IDNETs and F-IDNETs had leaked 4.3 ± 1.2 and 6.6 ± 0.8% at pH 5.5 (acidic conditions mimicking lysosomes and tumor microenvironment) compared to 3.1 ± 2.0 and 2.8 ± 2.4 % at pH 7.6 (normal conditions). In response to laser irradiation, IDNETs and F-IDNETs leaked 28.8 ± 13.9 and 40.3 ± 7.2 % at pH 5.5 and 39.8 ± 6.7 and 43.3 ± 6.8 % at pH 7.6. Minimal leakage observed in response to changes in pH whereas light triggered ~30 – 45 % DOX release in solution at 25 J/cm^2 in all conditions.

Fluorescent microscope images were obtained after 4 hours of sample incubation with SKOV3 cells are shown in Figure 4.5A. Minimal to no fluorescence observed by controls. Higher NIR fluorescence through folate-functionalized targeting of SKOV3 cells. Higher DOX fluorescence observed in SKOV3 cells incubated with F-IDNETs compared to IDNETs due to specific targeting, combined with slow release of DOX leads to increased cell death in the dark. Cell death and fragmentation can be seen more easily for F-IDNETs in NIR channel. Representative temperature rises for each sample shown

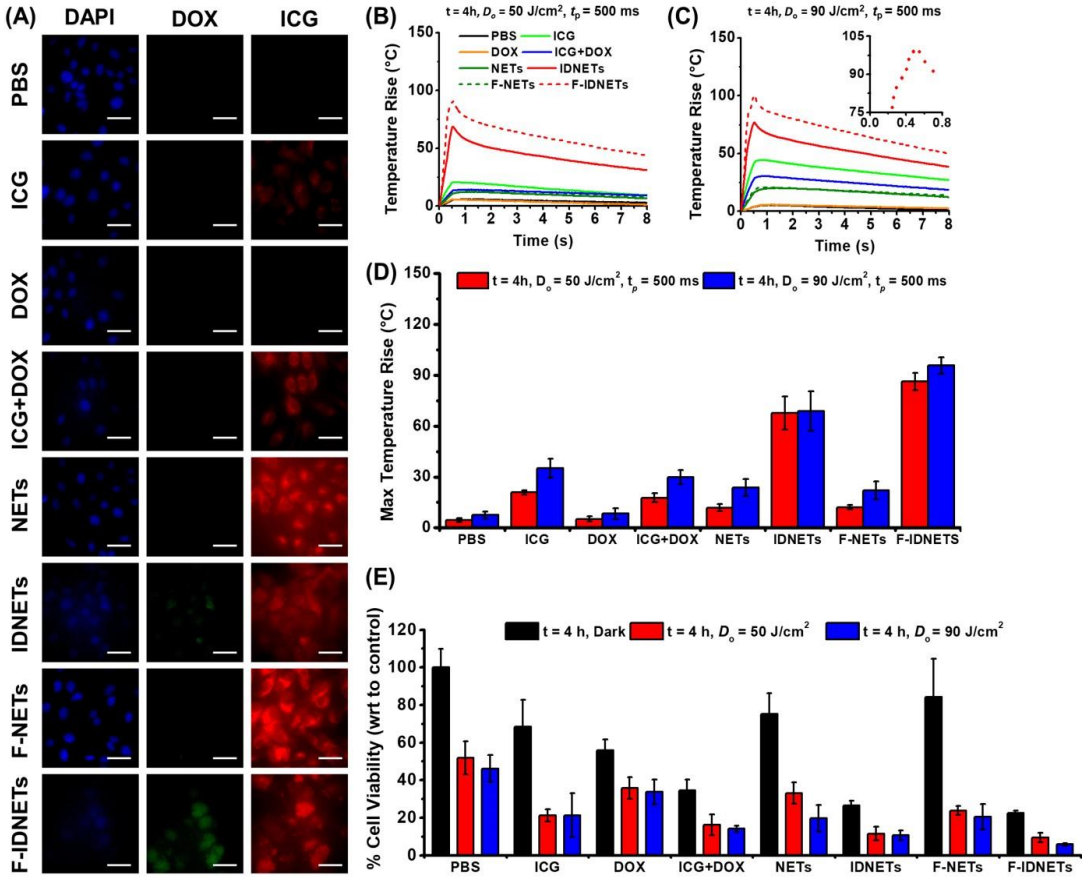

Figure 4.5: (A) Fluorescence Imaging of SKOV3 Cells after 4 hours incubation with various samples.Images processed in ImageJ and channels falsely-colored. Blue: DAPI, Green: DOX, and Red: ICG. Scale corresponds to 50 μm, Temperature Rise (B) Cells in suspension at D_o = 50 J/cm^2 (C) 90 J/cm^2, (D) Average max temperature rise of SKOV3 cells incubated with various samples, (E) Cell viability assessment in response to laser irradiation.

in Figure 4.5B and 4.5C for D_o = 50 J/cm^2 and D_o = 90 J/cm^2. MTT Cell viability assay was performed to determine cell viability after pulsed irradiation. Figure 4.5E shows the percentage cell viability with respect to control (PBS, dark). Pulsed laser induced photothermal cellular death in cells incubated with ICG-containing samples. A larger temperature rises is correlated to greater cell death. Cytotoxic cellular death contribution from DOX can be seen in absence of pulsed laser irradiation, can further contribute to increased cellular death as pulsed laser irradiation results in DOX release. Uptake of

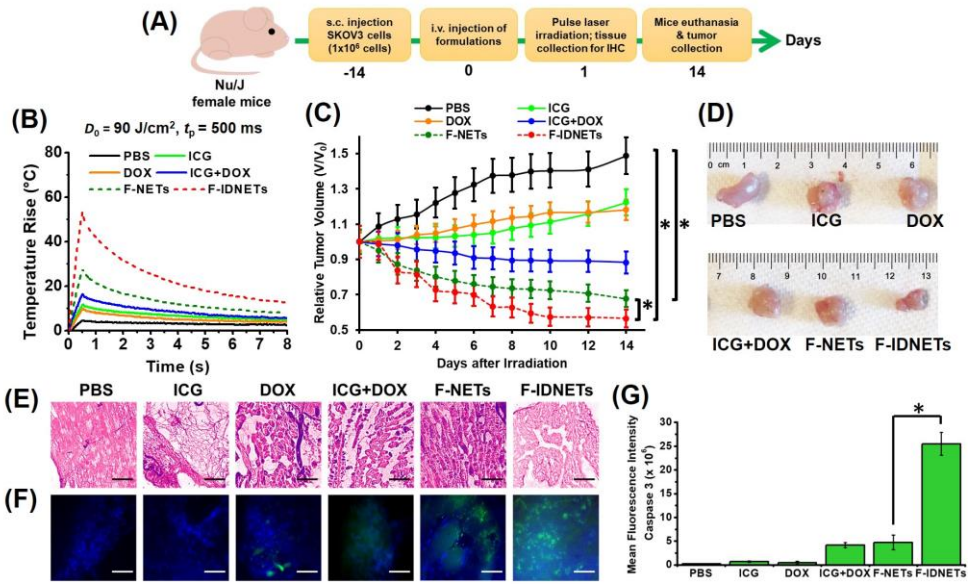

Figure 4.6: (A) Experimental timeline for animal study, (B) Representative temperature rise profiles in mice irradiated with D_o = 90 J/cm^2, t_p 500 ms at 24 hours post-injection, (C) Relative tumor growth taken up to 14 days after irradiation, (D) Photographs of harvested tumors at Day 14, (E) H&E-stained tumor tissues taken immediately after laser treatment, 10× magnification, scale bar = 200 µm, (F) FITC-labeled caspase-3 staining of tumor tissues taken immediately after laser treatment, 40× magnification, scale bar = 50µm. (G) Mean fluorescence intensity quantification of caspase-3 activation. (*p<0.05).

NETs by SKOV3 cells through lysosomal pathways corresponding to acidic conditions may aid with the slow release of DOX killing cells and inducing more uptake of ID-NETs compared to NETs alone.

As a proof-of-concept study, *in vivo* experiments were performed to evaluate the efficacies of the combination of chemo and photothermal effects mediated by F-IDNETs on the destruction of SKOV3 ovarian xenograft tumors-implanted in subcutaneously Nu/J nude mice. Pulsed laser irradiation (808 nm) was done 24 h after intravenous injection of F-IDNETs, F-NETs, free ICG-DOX, free DOX and free ICG formulations via tail vein. The timeline for in vivo experiments were shown in Figure 4.6A. To investigate if there was a photothermal effect during the pulse laser irradiation, we recorded the temperature rise profiles from the tumor bearing mice using a photovoltaic detector (Figure 4.6B).

Laser irradiation at 90 J/cm^2 and at a t_p = 500 ms resulted in a temperature rise of ≈ 54 ºC and 30 º C, for F-IDNETs and F-NETs injected mice, respectively. On the other hand, the free formulations, ICG, DOX and ICG-DOX resulted a temperature rise of ≈ 15 ºC. The tumor growth curves for mice intravenously injected with various formulations and subjected to pulse laser irradiation are presented in Figure 4.6C. In response to laser irradiation, we have observed significant reductions in the relative tumor volumes (V/V_o) of F-IDNETs when compared to that F-NETs. In addition, F-NETs and F-IDNETs exhibited statistically significant reduction in their tumor volumes when compared to the control treatment group (PBS injected mice and treated with laser). The residual tumors of representative mice at day 14 clearly reveal that F-IDNETs injected mice has the smallest tumors when compared to other treatment groups. The combination of chemo-photothermal therapy mediated by F-IDNETs results in significant delayed tumor growth, whereas a single treatment modality, such as chemotherapy alone or photothermal therapy alone resulted only in partial suppression. The mice body weights did not induce any noticeable changes for all the treatment groups during the treatment period (Figure 4.S4). To examine the extent of damages in other organs, we further performed hematoxylin & eosin (H&E) staining for the histological tissue sections of tumor, liver, kidney, lung, heart and spleen (Figure 4.6D and 4.SI 5). There were not any noticeable damages observed in liver, kidney, lung, heart and spleen in any of the treatment groups, whereas necrosis was clearly observed from the tumor tissue dissected from the F-IDNETs and F-NETs treated mice when compared to PBS control group and other free formulation groups. To investigate the presence of cellular apoptosis in response to 808

nm pulse laser irradiation, some of the tumors were extracted immediately after laser irradiation and imaged by fluorescence immunostaining to detect the presence of caspase-3. As evidenced by the FITC green fluorescence emission, there was caspase-3 activation in mice injected with F-NETs and F-IDNETs (Figure 6F). Analysis of these images confirmed that F-IDNETs were effective in inducing the apoptotic pathway of programmed cellular deaths via activation of caspase-3. F-IDNETs induced statistically significant higher values of FITC fluorescence intensity associated with Caspase-3 when compared to that of F-NETs, respectively (Figure 4.6G). Nevertheless, F-IDNETs can potentially be used as an effective theranostic nanoprobe in mediating combined chemo-photothermal therapeutic effects in destructing ovarian tumors.

4.5 Conclusion

In summary, we have demonstrated using NETs for NIR pulsed laser treatment of ovarian tumors in animal model. Encapsulation of ICG and DOX can allow for increased absorption of light from pulsed laser irradiation and subsequently higher temperature rises. Cellular death and slowed tumor growth as contributed by photothermal component (ICG) and chemotherapeutic (DOX) has means to treat ovarian tumors. The use of pulsed laser has clinical relevance such that it can reduce procedural time and trigger thermal release of DOX at localized area.

4.6 Appendix A. Electronic Supplementary Information

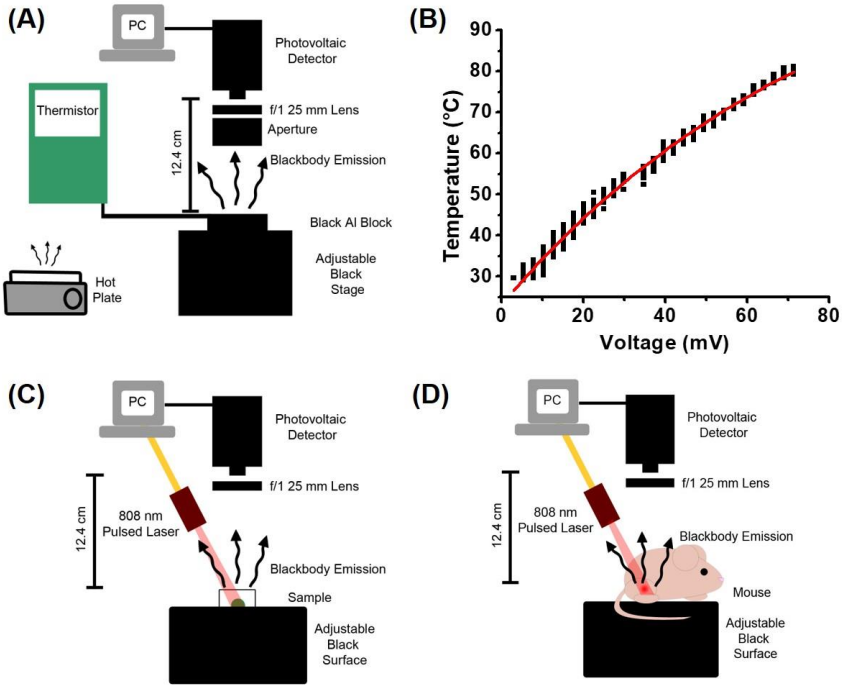

Figure 4.S1: (A) Photovoltaic detector-temperature calibration set-up. (B) Pulse-laser/Photovoltaic Detector set-up for samples and cells and (C) Pulse-laser/Photovoltaic detector set-up for animal studies.

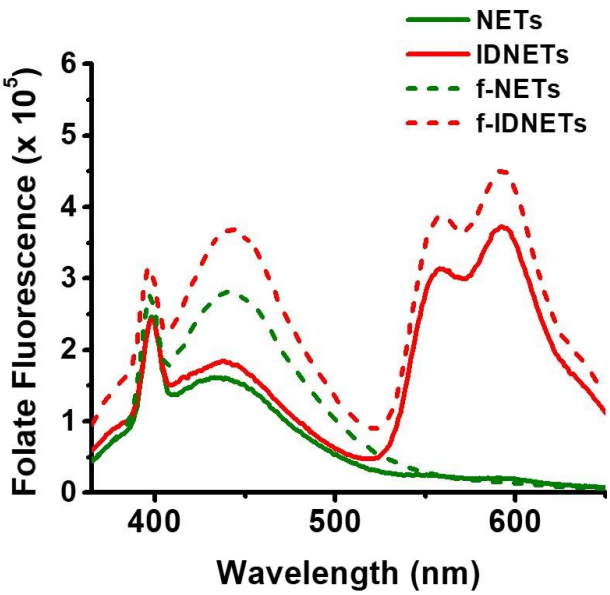

Figure 4.S2: Folate fluorescence in response to 350 nm excitation.

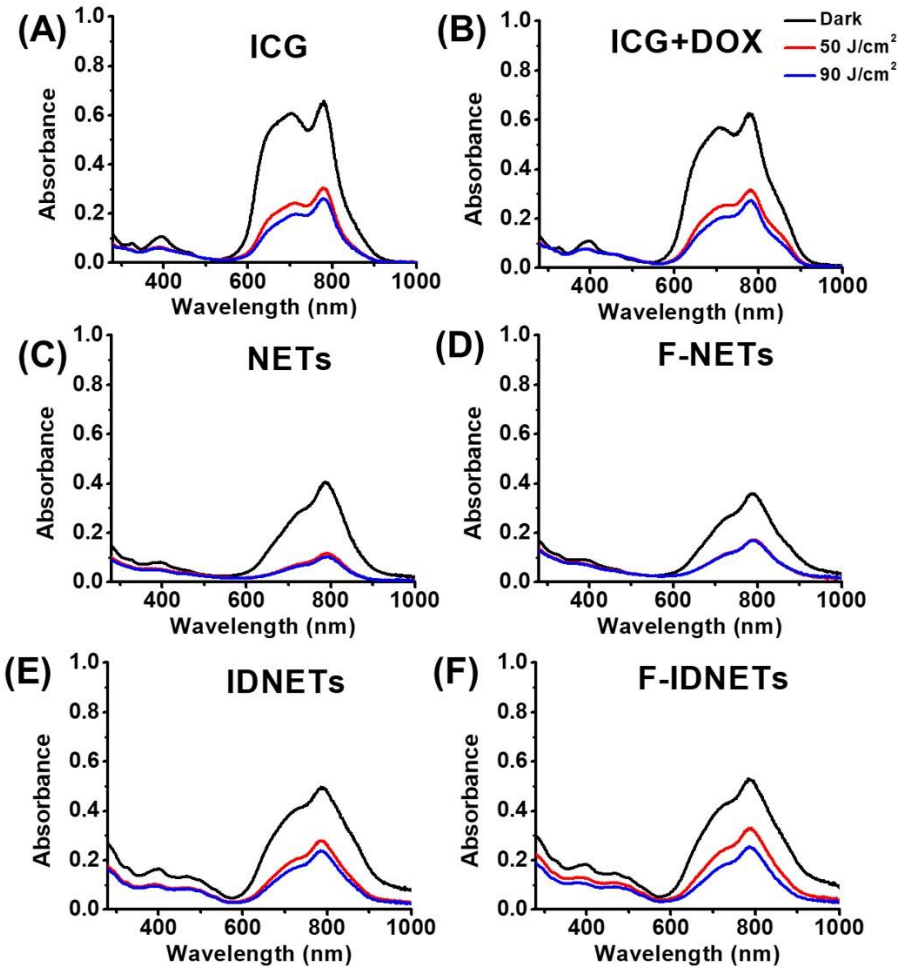

Figure 4.S3: Absorbance spectra of samples in dark (-) or light (+) at 50 and 90 J/cm^2. (A) ICG, (B) ICG+DOX, (C) NETs, (D) F-NETs, (E) IDNETs, and (F) F-IDNETs.

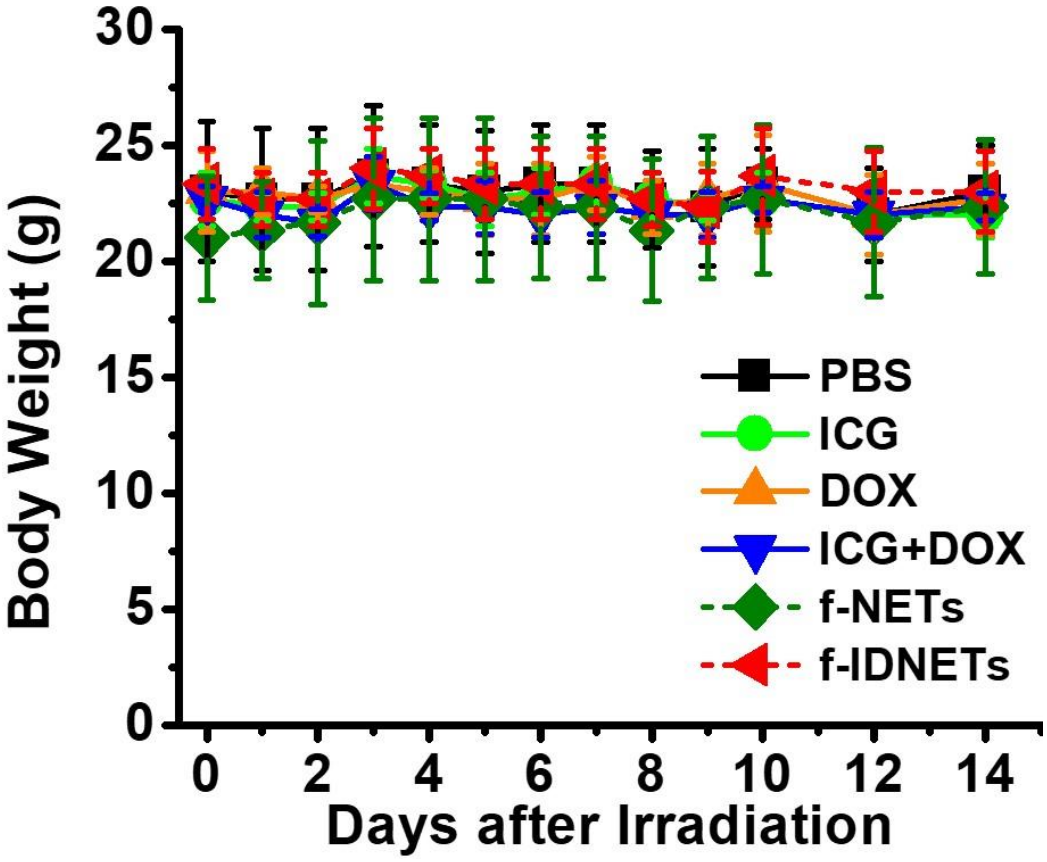

Figure 4.S4: Mice body weight over time. Measurements taken every day for 1 week and every other day for week 2.

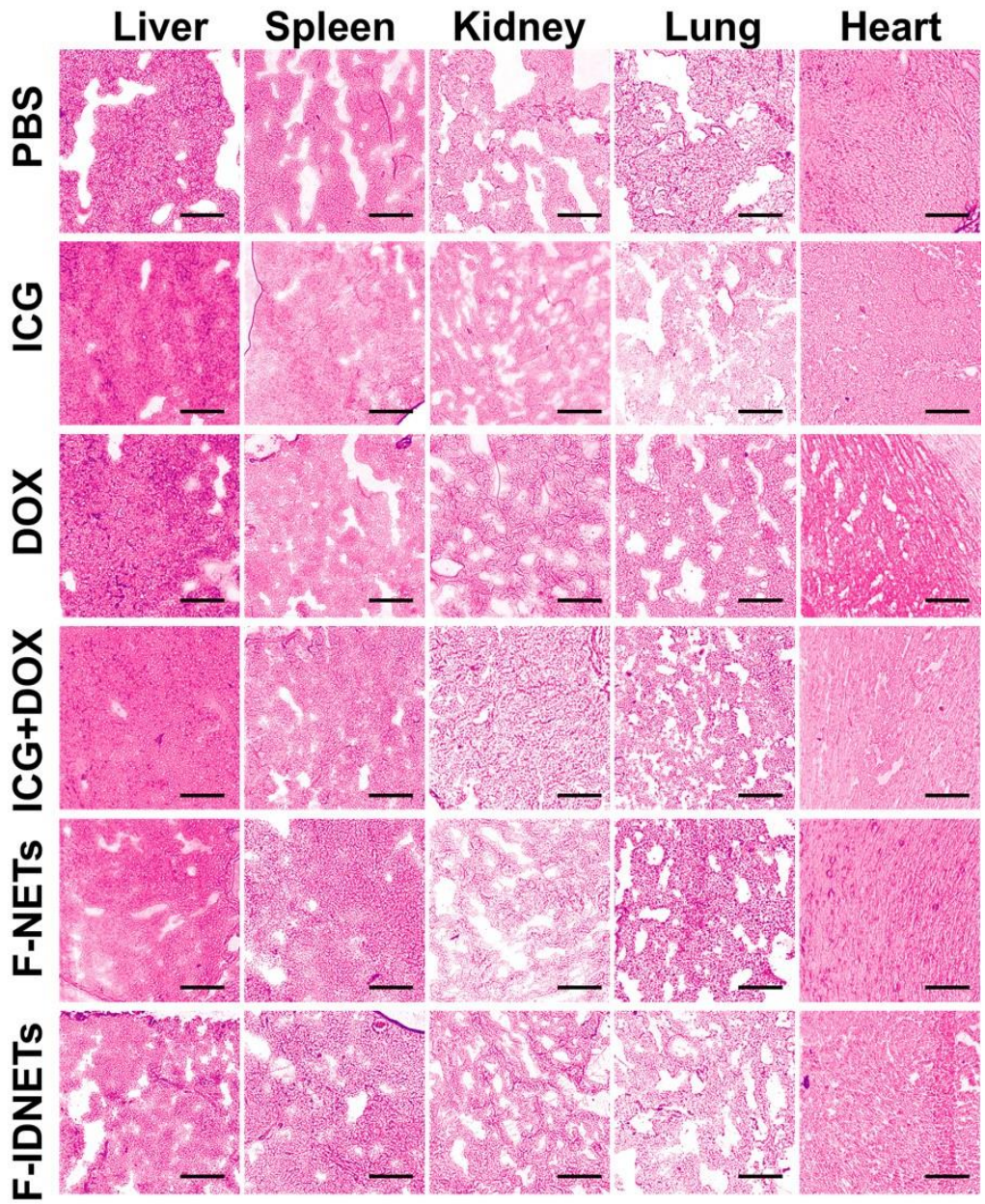

Figure 4.S5: H&E staining histological images of different groups obtained from tissues including liver, spleen, kidney, lung and heart of SKOV3 tumor-bearing mice immediately after laser irradiation. Scale bar = 200 μm. .

4.7 References

1. Chabner, B. A.; Roberts, T. G., Chemotherapy and the war on cancer. *Nat Rev Cancer* **2005,** *5* (1), 65-72.

2. Biemar, F.; Foti, M., Global progress against cancer—challenges and opportunities. *Cancer Biology & Medicine* **2013,** *10* (4), 183-186. DOI: 10.7497/j.issn.2095-3941.2013.04.001.

3. Bulten, B. F.; Sollini, M.; Boni, R.; Massri, K.; de Geus-Oei, L.-F.; van Laarhoven, H. W. M.; Slart, R. H. J. A.; Erba, P. A., Cardiac molecular pathways influenced by doxorubicin treatment in mice. *Sci Rep-Uk* **2019,** *9* (1), 2514. DOI: 10.1038/s41598-019-38986-w.

4. Tangpong, J.; Miriyala, S.; Noel, T.; Sinthupibulyakit, C.; Jungsuwadee, P.; St Clair, D. K., Doxorubicin-induced central nervous system toxicity and protection by xanthone derivative of Garcinia mangostana. *Neuroscience* **2011,** *175*, 292-299. DOI: 10.1016/j.neuroscience.2010.11.007.

5. Xiao, S.; Zhang, J.; Liu, M.; Iwahata, H.; Rogers, H. B.; Woodruff, T. K., Doxorubicin Has Dose-Dependent Toxicity on Mouse Ovarian Follicle Development, Hormone Secretion, and Oocyte Maturation. *Toxicological Sciences* **2017,** *157* (2), 320-329. DOI: 10.1093/toxsci/kfx047.

6. Lim, E.-K.; Kim, T.; Paik, S.; Haam, S.; Huh, Y.-M.; Lee, K., Nanomaterials for Theranostics: Recent Advances and Future Challenges. *Chem. Rev.* **2015,** *115* (1), 327-394. DOI: 10.1021/cr300213b.

7. Liu, M.; Du, H.; Zhang, W.; Zhai, G., Internal stimuli-responsive nanocarriers for drug delivery: Design strategies and applications. *Materials Science and Engineering: C* **2017,** *71*, 1267-1280. DOI: http://dx.doi.org/10.1016/j.msec.2016.11.030.

8. Mura, S.; Nicolas, J.; Couvreur, P., Stimuli-responsive nanocarriers for drug delivery. *Nat Mater* **2013,** *12* (11), 991-1003. DOI: 10.1038/nmat3776.

9. Khot, M. I.; Andrew, H.; Svavarsdottir, H. S.; Armstrong, G.; Quyn, A. J.; Jayne, D. G., A Review on the Scope of Photothermal Therapy–Based Nanomedicines in Preclinical Models of Colorectal Cancer. *Clinical Colorectal Cancer* **2019,** *18* (2), e200-e209. DOI: https://doi.org/10.1016/j.clcc.2019.02.001.

10. Zou, L.; Wang, H.; He, B.; Zeng, L.; Tan, T.; Cao, H.; He, X.; Zhang, Z.; Guo, S.; Li, Y., Current Approaches of Photothermal Therapy in Treating Cancer Metastasis with Nanotherapeutics. *Theranostics* **2016,** *6* (6), 762-772. DOI: 10.7150/thno.14988.

11. Weissleder, R., A clearer vision for in vivo imaging. *Nat Biotechnol* **2001,** *19*, 316. DOI: 10.1038/86684.

12. Crane, L. M. A.; Themelis, G.; Arts, H. J. G.; Buddingh, K. T.; Brouwers, A. H.; Ntziachristos, V.; van Dam, G. M.; van der Zee, A. G. J., Intraoperative near-infrared fluorescence imaging for sentinel lymph node detection in vulvar cancer: First clinical results. *Gynecologic Oncology* **2011,** *120* (2), 291-295. DOI: 10.1016/j.ygyno.2010.10.009.

13. Sevick-Muraca, E. M.; Sharma, R.; Rasmussen, J. C.; Marshall, M. V.; Wendt, J. A.; Pham, H. Q.; Bonefas, E.; Houston, J. P.; Sampath, L.; Adams, K. E.; Blanchard, D. K.; Fisher, R. E.; Chiang, S. B.; Elledge, R.; Mawad, M. E., Imaging of lymph flow in breast cancer patients after microdose administration of a near-infrared fluorophore: feasibility study. *Radiology* **2008,** *246* (3), 734-741. DOI: 10.1148/radiol.2463070962.

14. Verbeek, F. P. R.; Troyan, S. L.; Mieog, J. S. D.; Liefers, G.-J.; Moffitt, L. A.; Rosenberg, M.; Hirshfield-Bartek, J.; Gioux, S.; van de Velde, C. J. H.; Vahrmeijer, A. L.; Frangioni, J. V., Near-infrared fluorescence sentinel lymph node mapping in breast cancer: a multicenter experience. *Breast cancer research and treatment* **2014,** *143* (2), 333-342. DOI: 10.1007/s10549-013-2802-9.

15. Tang, C.-Y.; Wu, F.-Y.; Yang, M.-K.; Guo, Y.-M.; Lu, G.-H.; Yang, Y.-H., A Classic Near-Infrared Probe Indocyanine Green for Detecting Singlet Oxygen. *Int J Mol Sci* **2016,** *17* (2), 219-219. DOI: 10.3390/ijms17020219.

16. Hirano, T.; Kohno, E.; Gohto, Y.; Obana, A., Singlet Oxygen Generation by Irradiation of Indocyanine Green (ICG) and its Effect to Tissues. *Nippon Laser Igakkaishi* **2007,** *28* (2), 122-128. DOI: 10.2530/jslsm.28.122.

17. Zhao, P.; Zheng, M.; Luo, Z.; Gong, P.; Gao, G.; Sheng, Z.; Zheng, C.; Ma, Y.; Cai, L., NIR-driven Smart Theranostic Nanomedicine for On-demand Drug Release and Synergistic Antitumour Therapy. *Sci Rep-Uk* **2015,** *5* (1), 14258. DOI: 10.1038/srep14258.

18. Zheng, M.; Yue, C.; Ma, Y.; Gong, P.; Zhao, P.; Zheng, C.; Sheng, Z.; Zhang, P.; Wang, Z.; Cai, L., Single-Step Assembly of DOX/ICG Loaded Lipid–Polymer Nanoparticles for Highly Effective Chemo-photothermal Combination Therapy. *ACS Nano* **2013,** *7* (3), 2056-2067. DOI: 10.1021/nn400334y.

19. Cheung, A.; Bax, H. J.; Josephs, D. H.; Ilieva, K. M.; Pellizzari, G.; Opzoomer, J.; Bloomfield, J.; Fittall, M.; Grigoriadis, A.; Figini, M.; Canevari, S.; Spicer, J. F.; Tutt, A. N.; Karagiannis, S. N., Targeting folate receptor alpha for cancer treatment. *Oncotarget* **2016,** *7* (32), 52553-52574. DOI: 10.18632/oncotarget.9651.

20. Corbin, I. R.; Ng, K. K.; Ding, L.; Jurisicova, A.; Zheng, G., Near-infrared fluorescent imaging of metastatic ovarian cancer using folate receptor-targeted high-density lipoprotein nanocarriers. *Nanomedicine* **2013,** *8* (6), 875-890. DOI: 10.2217/nnm.12.137.

21. Kalli, K. R.; Oberg, A. L.; Keeney, G. L.; Christianson, T. J. H.; Low, P. S.; Knutson, K. L.; Hartmann, L. C., Folate receptor alpha as a tumor target in epithelial ovarian cancer. *Gynecologic oncology* **2008,** *108* (3), 619-626. DOI: 10.1016/j.ygyno.2007.11.020.

22. Kennedy, M. D.; Jallad, K. N.; Thompson, D. H.; Ben-Amotz, D.; Low, P. S., Optical imaging of metastatic tumors using a folate-targeted fluorescent probe. *J Biomed Opt* **2003,** *8* (4), 636-41. DOI: 10.1117/1.1609453.

23. van Dam, G. M.; Themelis, G.; Crane, L. M. A.; Harlaar, N. J.; Pleijhuis, R. G.; Kelder, W.; Sarantopoulos, A.; de Jong, J. S.; Arts, H. J. G.; van der Zee, A. G. J.; Bart, J.; Low, P. S.; Ntziachristos, V., Intraoperative tumor-specific fluorescence imaging in ovarian cancer by folate receptor-α targeting: first in-human results. *Nature Medicine* **2011,** *17*, 1315. DOI: 10.1038/nm.2472

https://www.nature.com/articles/nm.2472#supplementary-information.

24. Yu, L.; Dong, A.; Guo, R.; Yang, M.; Deng, L.; Zhang, J., DOX/ICG Coencapsulated Liposome-Coated Thermosensitive Nanogels for NIR-Triggered Simultaneous Drug Release and Photothermal Effect. *ACS Biomaterials Science & Engineering* **2018,** *4* (7), 2424-2434. DOI: 10.1021/acsbiomaterials.8b00379.

25. Lee, Y.-H.; Chang, D.-S., Fabrication, characterization, and biological evaluation of anti-HER2 indocyanine green-doxorubicin-encapsulated PEG-b-PLGA copolymeric nanoparticles for targeted photochemotherapy of breast cancer cells. *Sci Rep-Uk* **2017,** *7*, 46688. DOI: 10.1038/srep46688

https://www.nature.com/articles/srep46688#supplementary-information.

26. Hu, C.-M. J.; Fang, R. H.; Zhang, L., Erythrocyte-Inspired Delivery Systems. *Advanced Healthcare Materials* **2012,** *1* (5), 537-547. DOI: doi:10.1002/adhm.201200138.

27. Hu, C.-M. J.; Zhang, L.; Aryal, S.; Cheung, C.; Fang, R. H.; Zhang, L., Erythrocyte membrane-camouflaged polymeric nanoparticles as a biomimetic delivery platform. *Proceedings of the National Academy of Sciences* **2011,** *108* (27), 10980-10985. DOI: 10.1073/pnas.1106634108.

28. Zelepukin, I. V.; Yaremenko, A. V.; Shipunova, V. O.; Babenyshev, A. V.; Balalaeva, I. V.; Nikitin, P. I.; Deyev, S. M.; Nikitin, M. P., Nanoparticle-based drug delivery via RBC-hitchhiking for the inhibition of lung metastases growth. *Nanoscale* **2019,** *11* (4), 1636-1646. DOI: 10.1039/C8NR07730D.

29. Rao, L.; Meng, Q.-F.; Bu, L.-L.; Cai, B.; Huang, Q.; Sun, Z.-J.; Zhang, W.-F.; Li, A.; Guo, S.-S.; Liu, W.; Wang, T.-H.; Zhao, X.-Z., Erythrocyte Membrane-Coated Upconversion Nanoparticles with Minimal Protein Adsorption for Enhanced Tumor Imaging. *ACS Appl. Mater. Inter.* **2017,** *9* (3), 2159-2168. DOI: 10.1021/acsami.6b14450.

30. Zhu, D.-M.; Xie, W.; Xiao, Y.-S.; Suo, M.; Zan, M.-H.; Liao, Q.-Q.; Hu, X.-J.; Chen, L.-B.; Chen, B.; Wu, W.-T.; Ji, L.-W.; Huang, H.-M.; Guo, S.-S.; Zhao, X.-Z.; Liu, Q.-Y.; Liu, W., Erythrocyte membrane-coated gold nanocages for targeted photothermal and chemical cancer therapy. *Nanotechnology* **2018,** *29* (8), 084002. DOI: 10.1088/1361-6528/aa9ca1.

31. Bahmani, B.; Bacon, D.; Anvari, B., Erythrocyte-derived photo-theranostic agents: hybrid nano-vesicles containing indocyanine green for near infrared imaging and therapeutic applications. *Scientific Reports* **2013,** *3*, 2180. DOI: 10.1038/srep02180

https://www.nature.com/articles/srep02180#supplementary-information.

32. Burns, J. M.; Vankayala, R.; Mac, J. T.; Anvari, B., Erythrocyte-Derived Theranostic Nanoplatforms for Near Infrared Fluorescence Imaging and Photodestruction of Tumors. *ACS Appl. Mater. Inter.* **2018,** *10* (33), 27621-27630. DOI: 10.1021/acsami.8b08005.

33. Vankayala, R.; Mac, J. T.; Burns, J. M.; Dunn, E.; Carroll, S.; Bahena, E. M.; Patel, D. K.; Griffey, S.; Anvari, B., Biodistribution and toxicological evaluation of micron- and nano-sized erythrocyte-derived optical particles in healthy Swiss Webster mice. *Biomaterials science* **2019,** *7* (5), 2123-2133. DOI: 10.1039/c8bm01448e.

34. Jung, B. S.; Vullev, V. I.; Anvari, B., Revisiting Indocyanine Green: Effects of Serum and Physiological Temperature on Absorption and Fluorescence Characteristics. *Ieee J Sel Top Quant* **2014,** *20* (2). DOI: Artn 7000409

10.1109/Jstqe.2013.2278674.

35. Holzer, W.; Mauerer, M.; Penzkofer, A.; Szeimies, R. M.; Abels, C.; Landthaler, M.; Baumler, W., Photostability and thermal stability of indocyanine green. *J Photochem Photobiol B* **1998,** *47* (2-3), 155-64. DOI: 10.1016/s1011-1344(98)00216-4.

Conclusion

This research aimed to develop an erythrocyte-derived delivery platform for phototheranostics. Surface modification of NETs with against cell biomarkers allows for active targeting of cancer cells. Due to limitations of ICG's fluorescence quantum yield, a new doping material ICG-bound albumin was investigated for its enhanced fluorescence. This resulted in 2 to 6-fold fluorescence enhancement when compared to its ICG counterpart. Fabrication of NETs using a top-down approach from erythrocytes increased circulation time of ICG in healthy mice. μNETs remain in circulation less than nNETs likely due to size and altered mechanics similar to aged/damaged erythrocyte. Hence, more rapidly cleared compared to its smaller counterpart. 11% of nNETs remain in blood circulation up to 48 h post-injection. At 24h post-injection, no acute toxicity observed in major organs. Lastly, the addition of a chemotherapeutic drug was utilized to test a combination chemotherapeutic photothermal therapy triggered by a pulsed laser. The advantages to pulsed laser include decreased treatment times and driving a photothermal response. This study shows the significant reduction of tumor growth from F-NETs and F-IDNETs when compared to PBS treated with laser with a measurable temperature rise *in vivo* with corresponding H&E and Caspase-3 staining for necrosis and apoptosis, respectively. Additionally, the combination of ICG and DOX in F-IDNETs showed significant delay in tumor growth compared to individual treatment modalities.